UNCOVERING THE NEURONAL FASCICLE AS A REFERENCE STRUCTURE FOR MOTONEURON NEURITE PATTERNING VIA DSCAM1-MEDIATED INTERACTION

by

KATHY BUI

(Under the Direction of Daichi Kamiyama)

ABSTRACT

Necessary for functional neural connections are subcellular structures that send out and receive neurotransmitter signals (e.g., axon terminals and dendrites, respectively). Previously, our group showed that dendrite formation occurs precisely at the interaction site between *Drosophila* anterior corner cell (aCC) motoneuron and its partner, MP1 neuron – mediated by Down syndrome adhesion molecule (Dscam1) on the membrane. However, it is known that dendrites of 36 motoneurons form at unique sites – thus, an ensuing question: does the Dscam1 receptor play a role at other sites where motoneuron dendrites form and if so, how? We address whether neuronal interaction, mediated by Dscam1 receptor, plays a broad role in dendrite formation among motoneurons, using motoneuron 24 (MN24) system due to its distinct location from the aCC-MP1 contact site. The first part of this dissertation identifies the neuronal fascicle as a guiding structure for MN24 neurite development (dendrite formation and axon routing) via Dscam1 signaling; and discusses the implication of Dscam1 function within an individual neuron and among different motoneurons for neural circuitry formation.

The second part of this dissertation reports the use of the PCR product as a cloning-free, alternative donor format for CRISPR/Cas9-mediated knock-in in *Drosophila*. Combining multiple screening approaches, we insert a short disruptive cassette into the *ebony* gene and demonstrate the utility of PCR product donor for generating fly lines with a germline-transmitted knock-in. In the long term, this work should be useful for scalable generation of mutant fly lines for fly researchers. The third part of this dissertation characterizes the generation of the tripartite mRuby4 system as a potential red-colored interaction sensor and outlines a mutagenesis-based approach to further improve the self-complementation efficiency of this split fluorescent protein system.

INDEX WORDS: Dscam1, Dendrite Formation, Motoneuron, CRISPR, Knock-in, Split Fluorescent Protein

UNCOVERING THE NEURONAL FASCICLE AS A REFERENCE STRUCTURE FOR MOTONEURON NEURITE PATTERNING VIA DSCAM1-MEDIATED INTERACTION

by

KATHY BUI

B.S., Emory University, 2017

A Dissertation Submitted to the Graduate Faculty of The University of Georgia in Partial Fulfillment of the Requirements for the Degree

DOCTOR OF PHILOSOPHY

ATHENS, GEORGIA

2024

UNCOVERING THE NEURONAL FASCICLE AS A REFERENCE STRUCTURE FOR MOTONEURON NEURITE PATTERNING VIA DSCAM1-MEDIATED INTERACTION

by

KATHY BUI

Major Professor:	Daichi Kamiyama
Committee:	Jonathan Eggenschwiler
	Edward Kipreos
	James Lauderdale

Electronic Version Approved:

Ron Walcott
Vice Provost for Graduate Education and Dean of the Graduate School
The University of Georgia
August 2024

ACKNOWLEDGEMENTS

I would like to remind the reader that I am just a student. Therefore, there has been *a lot* of guidance throughout my Ph.D. journey. I would like to express my gratitude to Daichi for his invaluable guidance and support throughout my Ph.D. journey. His expertise, encouragement, and unwavering commitment to excellence have been instrumental in shaping my research and professional growth. His dedication to advancing knowledge and nurturing talent serves as a shining example for me to emulate in my future endeavors. I would also like to enthusiastically thank my committee members: Edward, Jim, and Jonathan, for being excited and curious about my work and giving constructive feedback for the nascent idea that turned into this second chapter.

I would like to thank Rie and Miyuki for doing a lot of behind-the-scene work to keep the lab functional like preparing fly materials and ordering reagents. Thanks to their work, I can take a lot of mental load off to work on my research. That, in itself, is such a luxury – thank you!

To my lab mates (of course!): I would like to thank Melissa, Ryo, and Kota for guiding me through the growing pains of being a lost graduate student. You all are so clever, bright, and kind and epitomize my ideals of being a researcher. Even as I grow out of being a graduate student, I would still like your guidance and advice even as an old, frail researcher.

I would like to thank my mom and sister for supporting me! I am grateful for their continuous support for my studies as always. I'd like to thank my partner, Piotrek, for listening and giving me advice. You have been a solid rock and a voice of reason for me.

Lastly, I'd like to thank Tofu, Gacek, and Mister Chaplin. You all are good kitties.

TABLE OF CONTENTS

Page

LIST OF TABLES

Page

LIST OF FIGURES

Page

CHAPTER 1

INTRODUCTION AND LITERATURE REVIEW

1.1 A MODERN SCIENCE PROBLEM: UNDERSTANDING THE NEURAL CIRCUIT

Ramón y Cajal, the father of modern neuroscience, characterized that (1) the organized neural circuitry is a fundamental feature of animal brains and (2) these neural circuits guide an animal's interaction with the external environment [1–3]. A fundamental challenge among the neuroscience community is addressing the question: "How do neurons give rise to complex outputs such as neuromuscular coordination and higher-order thinking?" Individual neurons in isolation are not sufficient for the elaborate movements and mental processes. Yet, they are the foundation of animal behavior and cognition. Neurons are organized and assembled in a neural circuit, relaying information across multiple cells to generate these robust behaviors. But how these neural circuits develop remains a prominent field of study today.

With the recent technological advances in research methodology, we begin to delve into the black box of neural circuitry assembly, allowing researchers to begin to map out the underlying molecular mechanisms that guide the assembly of regional microcircuits. Neural circuitry assembly is crucial and well-conserved in both biological and physiological contexts, from inter-cellular signaling to development and disease. Thus, understanding how neural circuits begin to wire will provide the foundational framework for future work in vertebrate neurodevelopment. Certainly, the monumental challenge of resolving how neural circuits are built relies on the

collective efforts of interdisciplinary researchers, which may chance the paramount breakthrough of our lifetimes.

1.2 NEURAL CIRCUITRY IN DEVELOPMENT AND DISEASE

The adult human central nervous system consists of roughly 86 billion neurons, yet what makes our nervous system so powerful is not just the sheer abundance of neurons [4]. Rather, it is that these neurons communicate with one another in extensive, interactive sets of neural networks. While vertebrate neurons can vary in morphology – a reflection in their specialized cellular functions – neurons are distinguishable from most other cells in the body in that they have two defining subcellular structures responsible for relaying neural information: (1) the axon is the long process of neurons in which messages are relayed from the cell body to the terminal end, and (2) the dendrites are finer, shorter processes where one neuron receives messages from other cells. These structures underlie neural communication and must be organized for *de novo* neural circuit assembly during embryonic development. Consequently, disruptions in dendrite and axon patterning may lead to developmental defects and neurological disorders, such as intellectual disabilities, autism, and epilepsy [5–8].

Currently, our ability to assess neurological disorders is based on the symptomatic, explicit behaviors such as avoidance of eye contact, non-verbal communication, or outward changes in mood [7,9]. For example, autism is typically diagnosed from the ages of 2 based on the standard diagnostic system, which is well beyond the time of establishment of the embryonic neural circuit [7]. Should more sensitive detection strategies allow us to identify defects of the neural circuit before the onset of these behavioral symptoms, we may be able to intervene and treat these abnormalities at even earlier time points. Moreover, the basic principles for building the neural

circuitry are often common for development and repair [10,11]. Thus, understanding how neural circuit formation is orchestrated in the developing CNS may help researchers to not only prevent the severity of these neurological defects but also design pro-regenerative therapies in which developmental programs are recapitulated to regenerate neural circuities in adult injury or diseases.

1.3 *DROSOPHILA* AS A MODEL TO INVESTIGATE EMERGING NEURAL CIRCUITS

The monumental task of studying the vertebrate central nervous system is non-trivial due to a combination of ethical, technical, and practical considerations. Thus, the need for a more accessible and amenable animal system is required for studying neurodevelopment. Enter: *Drosophila* melanogaster, the common fruit fly and established model organism since the early 1900s [12,13]. Although *Drosophila* appears quite unrelated from humans, it serves as a powerful genetic model as roughly 50% of Drosophila genes have homologous counterparts in the human genome [14–16]. Moreover, an estimated 75% of the human-disease-associated genes are conserved in the fly genome [14]. For these reasons, researchers have been using the *Drosophila* system to model many neurological diseases such as Parkinson's, Alzheimer's, Autism, and Down Syndrome, for example [17–22].

Moreover, the *Drosophila* model system is powerful due to its abundance of genetic tools. One such powerful tool is the two-part UAS/GAL4 system, which allows for cell-specific expression of a gene of interest [23,24] (**Figure 1.1**). The UAS/GAL4 system was originally derived from yeast, and transplanted into the *Drosophila* system [23–25]. The transcription of the GAL4 protein is under the control of a cell-type-specific enhancer – consequently restricting GAL4 transcription factor in the cell type/tissue of interest [25–27]. GAL4 expression alone has no biological activity in *Drosophila*. The GAL4 transcription factor binding to the Upstream

Activation Sequence (UAS), allows for the transcription of the downstream transgene of interest [23,27]. For example, *Drosophila* researchers commonly "add" a sequence that encodes for the green fluorescent protein (GFP) downstream of UAS. Consequently, only that specific cell type/tissue contains such green fluorescence. This modular cell-specific expression system relies on the extensive GAL4 driver lines available at stock centers. For this, the combinations of GAL4 drivers with UAS gene constructs are endless.

In addition, there have been recent advancements in genome engineering such as the advent of the CRISPR/Cas9 system [28–30]. Using the CRISPR/Cas9 system, researchers can target a specific site in the genome and make modifications (such as deletion or insertion) to the gene of interest [31,32]. By manipulating these genes, we can decipher what the function and importance of that gene is – especially, in the context of neurodevelopment. To this end, we can begin to map out gene function in the various contexts of development and injury.

1.4 THE *DROSOPHILA* EMBRYONIC CENTRAL NERVOUS SYSTEM (CNS)

Drosophila is a truly versatile model organism that has been studied productively for a diverse range of biological phenomenon [33,34]. *Drosophila*, with its rapid developmental progression (approximately 10 days from embryo to adult), lays down foundational cell patterning during embryonic development, which is crucial for later neurodevelopment. The *Drosophila* embryonic central nervous system can be divided into two parts: the brain lobes and the ventral nerve cord (**Figure 1.2a**). These nervous organ structures are functionally conserved across many animals and corroborate with the vertebrate brain and nerve cord [35]. The *Drosophila* embryonic CNS contains roughly 15,000 neurons and glia and grows tenfold in size in adult stage, emphasizing the

importance of early cell patterning and neuronal wiring [35–38]. Thus, laying down the critical cell patterning and neuronal wiring is critical for later stages of neurodevelopment in *Drosophila*.

During early embryogenesis, the embryo cell composition will be comprised about 65% of myogenic cells and 35% of neural cells [39]. The crucial period of embryonic development must ensure that these neurons are wired correctly to each other and to other cells (such as skeletal muscles). Like most animals, the *Drosophila* embryo is bilaterally symmetrical and can be divided into 14 total segments along the anterior-posterior (A-P) axis: where the most anterior 3 segments will make the head, the following 3 segments will make the thorax, and the final 7 segments will make the abdomen [40]. The CNS contained in each segment is referred to as a "neuromere". Because the embryo can be divided bilaterally, the neuromere could similarly be bilaterally divided into two half-neuromeres. The half-neuromere contains ~30 neuroblasts, which can give rise to a combination of motoneurons and interneurons upon differentiation, forming the embryonic neural circuit [41].

Accessible through fillet dissection, the embryonic CNS allows for detailed neuronal tracing studies to investigate the fine neuronal structures such as axons and dendrites at the single cell resolution [42] (**Figure 1.2b**). There are a series of tour-de-force studies that characterize individual embryonic neurons, with notable studies characterizing roughly 270 interneurons and 36 motoneurons in the embryonic CNS [43–45]. While the cell bodies are organized into the small space of the CNS, the more telling features of neuronal function are where their neuronal projections (axons and dendrites) are organized. Neuronal projections within the CNS can be organized by either a combination of fasciculations running along the mediolateral axis or AP axis [43,46,47]. Projections running along the mediolateral axis follow the anterior or posterior commissures – or the "horizontal steps of the ladder" – whereas projections running along the AP

axis follow the longitudinal commissure (**Figure 1.2a**). Motoneuron projections are not only restricted to the small space of these commissures but also project their axons out into the peripheral field, where they will innervate and control 30 distinct body wall muscles to form neuromuscular junctions [46,47] (**Figure 1.2a**).

Compared to the axons that extend into the peripheral field, dendritic projections of motoneurons are integrated into neuromeres, where they will receive upstream input from other cells in the CNS [48,49]. Because motoneurons receive differential inputs from different cells, the placement and elaboration of their dendritic projections will vary from motoneuron to motoneuron. Motoneuron dendrites have been documented to emerge around 13:00 after egg laying (AEL) and continue growing well into late larval stages [47,50–52]. Kim et al. suggested in a subsequent study that larval motoneuron dendrites laterally have more elaborations in the regions where embryonic motoneuron dendrites form, indicating that the sites where the primary dendrites begin to form lay a foundation where later high-order dendrites and synapses can build upon [47].

Landgraf et al. studied the locations of individual motoneuron dendrites to gain some insight into the functionalities of the motoneurons [44]. Interestingly, they found that their motoneuron dendrites are organized based on the muscle groups they innervate, indicating functional specificity [46]. Characteristically, these dendrites and axons invariably project to their proper targets across individuals, even before any motor activity, suggesting that a genetic program guides their patterning. But how exactly do these neuronal projections locate their specific targets? Understanding the mechanisms behind the precise targeting of these neural connections is crucial for unraveling neural circuit development.

1.5 EXTRINSIC MOLECULAR MECHANISMS OF NEURAL WIRING IN CNS

In nature, we find two major extrinsic mechanisms for controlling dendrite and axon patterning, which are the basis of neural wiring. On one hand, neuronal processes can be guided by gradients of diffusible molecules [53–56]. Particularly, some early works have identified some diffusible molecules for guiding where the axon growth cone is directed [55,57–63]. These diffusible molecules are secreted from specialized midline glia, and therefore, axon guidance will be under the direction and in relation to the midline, an important organizing center [62–65]. These guidance molecules can be attractive or repulsive, depending on which receptors are expressed on the growth cone. Of the ligand-receptor complexes that play a role in axon guidance, the most well-studied are Slit-Robo1 and Netrin-Frazzled/DCC complexes [59,60,62,63].

The evolutionary conservation of the Slit-Robo pathway across bilaterian animals underscores its fundamental role in governing the intricate process of midline axon crossing [54,58,62,63]. This Slit-Robo complex is notably well-documented in *Drosophila* axon guidance[63]. Slit, a ligand, is secreted by the midline glia, where it binds to Robo receptors found throughout the VNC [62,63]. In *slit* mutants, embryos suffer from aberrant neurodevelopment, specifically CNS axons are all joined at the midline due to the absence of midline repulsion [63]. Perhaps unsurprisingly, these mutants do not survive past the embryonic stage. This severe neuro-defect is phenocopied in mutant embryos where there is an absence of Robo receptors that can bind to the Slit ligand (*robo1* and *robo2* mutants) [66].

Contrary to the Slit-Robo pathway, Netrin-Frazzled/DCC pathway mediates the midline attraction and crossing [59,60,64]. In *Drosophila*, Netrin ligands are encoded by NetA and NetB genes, and these two Netrin ligands can interact with their receptor Frazzled (Fra), a member of

the DCC (Deleted in Colorectal Cancer) family [60,67]. Similar to Slit, Netrins are secreted from midline glia and diffuse across the VNC to attract axons for midline crossing [64].

Not exclusive to the two aforementioned signaling pathways, there are additional molecules (identified and unknown) that play redundant or parallel roles in midline crossing, alongside of the existing Netrin-Fra/DCC and Slit/Robo pathways. One study pointedly noted that even in the absence of Net-Fra/DCC signaling, some CNS axons could still successfully cross the midline, implying other molecules aside from Netrins or Fra/DCC playing a role in midline crossing [68]. To identify these guidance molecules, researchers performed a genetic screening where they introduced mutations in the NetAB or fra mutant background to determine which mutant genes that augment a more severe phenotype, suggesting that these genes played a parallel role from Netrin-Fra/DCC pathway for midline crossing [68]. Some of these mutation were found in genes including Dscam (Down Syndrome Cell Adhesion Molecule) and flamingo, encoding an atypical protocadherin [68,69]. Interestingly, Dscam could bind with Netrin ligands to mediate midline attraction [68,70]. Moreover, they show the double loss of Dscam and fra genes produce a more severe midline crossing defect than the individual loss of either Netrin or fra genes, suggesting that Dscam can function in a pathway parallel to the Netrin-Fra/DCC pathway [68]. Dscam is an unusual, multi-faceted molecule in itself, playing various roles in the CNS development, which we describe in the following passage.

1.6 DSCAM AS A CONSERVED CUE FOR NEURONAL MORPHOGENESIS IN CNS

Down syndrome cell adhesion molecule (Dscam), belonging to the immunoglobulin superfamily of cell adhesion molecules, exhibits a notable degree of structural conservation across humans to flies (vertebrate Dscam and Dscam-like1 (Dscaml1), and four *Drosophila* homologs, Dscams 1–

4) [71–73]. Within vertebrates, Dscam displays widespread expression throughout the nervous system and plays a role in governing proper axonal guidance and synaptogenesis [71,74–76]. As its name suggests, a well-studied cellular function of Dscam is its property for cell-adhesion – namely for the specific, homophilic binding in cell aggregation assays [77]. However, while some proposed functions in neurodevelopment align with Dscam's function for adhesion, various studies have uncovered other nuanced Dscam functions for neurodevelopment, such as chemotaxis in neurite patterning [78].

Down syndrome (DS), also referred to as Trisomy 21, is one of the most frequent genetic disorders, in which an individual has an extra copy of chromosome 21 [79,80]. This extra copy of chromosome 21 affects how a child's brain develops, which typically manifests as an intellectual disability. Individuals with DS are more likely to have a reduced brain weight, decreased number of neurons, and abnormal neuronal morphology [81,82].

Human DSCAM gene, associated with the titular DS, was identified in human chromosome 21q22, associated with the mental retardation phenotype [83–85]. It has been suggested that overexpression of DSCAM may contribute to some DS phenotypes due to DSCAM's unique properties for cell adhesion and chemotaxis in neurodevelopment [86]. Studies of embryonic development are difficult in humans – thus, the investigation of Dscam function has been pioneered within the *Drosophila* fruit fly system. In the few studies of Dscam function in vertebrates, Dscam proteins have been shown to mediate either attraction or repulsion in retina formation, suggesting that the balance between chemo-attraction and -repulsion mediated by Dscam proteins is dependent on context (e.g., cell type, presence of co-receptors, availability of downstream effectors) [87,88]. This contextual modulation of Dscam protein functionality

underscores the differential outputs of cell morphology during development despite widespread Dscam expression [72,86].

As in vertebrates, Dscam has comparable cellular functions for insect axon guidance [89]. One key difference between vertebrate and insect Dscam is that the insect gene has extensive alternative splicing, in which it can encode up to 19008 extracellular domains, which can then bind homophilically in an isoform-specific manner [90]. Nevertheless, the core function of insect Dscam seems to be largely conserved in vertebrate DSCAM and DSCAML1 [73,74].

The *Drosophila* model system has been indispensable for our current knowledge of Dscam function. To reiterate, Dscam has been known for its function in axon guidance, as noted previously, but also plays additional roles outside of guidance – including fasciculation and dendrite morphogenesis during neurodevelopment [68,90]. Dscam function for dendrite morphogenesis has been well-characterized in peripheral sensory neurons, which are located outside of the CNS [91]. Peripheral sensory neurons are characterized by the dendritic "tiling" feature, where dendrites avoid overlap and are spaced out so that they cover a large surface area on the body wall [92–94]. Individual sensory neurons express a stochastic handful of *Dscam1* isoforms on their cell surfaces and in this way can be uniquely identified, able to recognize "self"—other processes of the same cell—but remaining blind to the processes of neighboring cells [95]. This self-recognition gives rise to self-avoidance, and two sister processes of the neuron repel from each other, promoting this dendritic tiling feature [96–101]. Thus, Dscam1-mediated self-avoidance prevents self-crossings within sister dendritic branches, but allows overlap with neighboring neurons through its molecular diversity and the isoform specificity of the interactions [95,101]. This model is strongly supported by studies investigating dendrite spacing in the peripheral nervous system during development. However, the Dscam function is less clear for

central neuron dendrites, the major structure for synaptic input in the embryonic CNS, as CNS dendrites overlap within the limited space of the VNC [42].

So far from what we know, in CNS neurons, Dscam has differential functions compared to their functions in sensory neurons [102]. In adult *Drosophila* motoneurons, loss of Dscam1 impairs the formation of new dendritic branches already during early stages of dendritic growth [103]. These observations indicate a primary growth defect instead of a dendritic self-repulsion defect [103]. Similarly, in embryonic stage, we see embryonic aCC (anterior Corner Cell) motoneuron show a loss of primary dendrite growth in late embryos of *dscam1* null mutants [42,50]. Corroborating with this observation, aCC-specific *dscam1* knockdown shows loss of aCC dendrites [50]. Interestingly, dscam1 knockdown in another neuron, MP1 (midline precursor 1) also shows loss of dendrites in aCC motoneuron [50]. The MP1 neuron is known to intersect with aCC motoneuron in a stereotyped position [50,104]. We discovered that at the point of intersection, aCC dendritogenesis—the formation of primary dendritic branches—is promoted by a cell-cell adhesion process. Importantly, this adhesion process, identified as an inter-neuronal Dscam1 interaction, involves Dscam1 on one neuron binding to its counterpart Dscam1 on an adjacent neuron, recruiting Pak1 kinase through the Dreadlocks (Dock) adaptor protein on the aCC membrane [50]. This recruitment initiates local cytoskeletal changes, leading to dendritic branch outgrowth. However, the extent to which this mechanism represents a conserved principle among motoneurons, where inter-neuronal Dscam1 interactions dictate dendritic outgrowth sites (and simultaneously, axon guidance), will be explored in Chapter 2.

1.7 GENOME EDITING AS A TOOL TO PROBE GENE FUNCTION

With the development of large-scale genome sequencing and annotation projects, the Genomic Revolution has inundated researchers with an overwhelming wealth of information. Now present: a novel, forefront challenge of mining through the data abyss and transforming it into functionally and physiologically significant knowledge. Central to this problem is the need for efficient and reliable methods that allow us to determine how genes function in a cellular and physiological context.

To this end, researchers have generated genetic mutants in order to probe and identify the functions of these genes. To create genetic mutants, the genome must be altered. Genomes (and their constituent genes) are comprised of double-stranded DNA. Genetic alterations can be introduced when there are double-stranded breaks (DSB) in the DNA [105]. Utilizing techniques to introduce DSB (e.g, radiation, alkylating agents, nucleases), researchers can manipulate the DNA by deletion, addition, or change in base-pairs at the broken ends of the DNA, which can disrupt the gene function [106–109]. The process of making specific changes to the DNA of an organism by adding, removing, or altering DNA is referred to as genome editing. Genome editing technologies can be used on somatic cells (non-heritable), or germline cells (for reproduction) [110]. The current utility of genome editing lies in probing gene function in model organisms, like the *Drosophila* fruit fly.

The ability to specifically engineer biological systems and organisms holds enormous potential for applications across basic science, medicine and biotechnology. However, the ability to modify the genome is not a novel concept. In fact, we have known about a few research techniques to modify eukaryotic genomes for well over a century.

Genome editing is an established type of engineering for about a century but its humble beginnings used non-specific, low-efficiency approaches. For example, some of the earliest studies in 1928 demonstrated using X-rays or gamma rays could introduce genetic mutations – a process known as irradiation-induced mutagenesis [106,111,112]. Similarly, chemical-induced mutagenesis used chemical agents to induce mutations in genetical materials in a comparably random approach [107,108]. These two approaches were useful for inducing a large number of genomic mutations and generating large-scale libraries of mutant lines [113,114]. Another wave of large-scale mutant line generation was from the discovery and advantageous use of transposable elements. Transposable elements, or transposons, are mobile segments of DNA that are able to "hop" or move positions within the genome [115]. The most well-studied transposon movement is which a transposase enzyme excises a DNA element from its original location and reintegrates it into another genomic locus [116]. Utilizing these endogenous DNA transfer vehicles, researchers have been able to build extensive experimental tools and animal lines by introducing a wide variety of gene cassettes, a few including reporters and mutagenic gene trap cassettes [117–119]. While these aforementioned methods were indispensable for the experimental tools and lines researchers use today, these mechanisms for introducing genomic mutations were non-specific and difficult to replicate.

Despite the swath of methodologies for non-specific genomic editing, there has since been a call for mechanisms that could be more specific, reliable, and targeted. More targeted genomic editing mechanisms, such as those mediated by zinc finger nuclease (ZFN) and transcription activator-like effector nuclease (TALEN) became popular in the 2010s [120,121]. These methods utilized engineered chimeric nucleases which contain two main components: (1) a DNA cleavage domain that introduces a double-strand break in the genomic DNA and (2)

modular DNA-binding domains that recognize the nucleotide sequence within the genome [122]. ZFNs and TALENs differ in the latter component, where their DNA-binding domains will recognize nucleotide in some varying specificity. For instance, one ZF DNA-binding domain recognizes a unique triplet nucleotide code, and there is a library of ZF domains that accounts for almost all 64 possible triplet nucleotide codes [123–125]. On the other hand, one TALE DNA-binding domain can recognize a single nucleotide [126–128]. Like zinc-fingers, TALE repeats are modular and can be linked together to recognize a specific DNA sequence – typically, ~5 ZF domains or ~20 TALE domains to confer specificity [128]. However in contrast to zinc-fingers, constructing TALE repeats do not require re-designing the linkage between repeats, making TALENS more modular for specific targeting than ZFNs [122]. One limitation with using ZFNs or TALENs is the design and cloning assembly for specific targeting – ZF domain may not account for a triplet nucleotide sequence that is in the targeted genomic locus, and TALE binding site must start with a Thymine base [122]. Moreover, these methods require some extensive molecular cloning (e.g., "Golden Gate" molecular cloning or high-throughput solid-phase assembly [129–131].

One promising genome editing system, distinct from ZFNs and TALENs, is the CRISPR (Clustered Regulatory Interspaced Short Palindromic Repeats)/CRISPR-associated (Cas) system, which utilizes a modular, facile RNA-guided DNA cleavage. In the following passage below, we explore how the CRISPR/Cas9 system changed the landscape of genome editing for many model organisms and its potential for basic science research.

1.8 CRISPR/CAS9-MEDIATED KNOCK-IN FOR GENERATING SPECIFIC MUTANTS

CRISPR/Cas9-mediated genome editing system has emerged in recent years, allowing investigators to specifically manipulate genes (and any subsequent protein products) in a diverse

range of organisms and cell types. The CRISPR-associated protein is a non-specific endonuclease that cleaves and generates a DSB [105,132,133]. There are several versions of Cas endonucleases isolated from different bacteria but the most commonly used one is the Cas9 nuclease [134]. The guide RNA is a specific RNA sequence that recognizes the target DNA region of interest and directs the Cas nuclease there for editing [135]. The gRNA is made up of two parts: crispr RNA (crRNA), a ~20 nucleotide sequence which recognizes the specific DNA sequence in the genome, and a tracr RNA (trRNA), which serves as a binding scaffold for the Cas nuclease [135,136]. The novelty of this model is that the user can design and clone the gRNA with relative ease compared to the predecessor ZFN- and TALEN-mediated systems.

The CRISPR/Cas9 system was shown to be capable of manipulating in a variety of genomes. Some of the earliest adaptations of the CRISPR/Cas9 system were in model organisms such as zebrafish, mice, and cultured mammalian cells [31,137,138]. In addition, the system was also applied to bacteria, yeast, and insects including the *Drosophila* fruit fly, a key genetic model [29,139,140].

More importantly, the *Drosophila* fruit fly was the first model to showcase germline transmission of Cas9-induced changes, in which the targeted genome modifications in the *Drosophila* germline are transmitted to progeny [29,30]. The approach to making germline-transmitted genetic mutants is important due to the fact that the generation of mutant fly lines are foundational for fly researchers to readily and reproducibly conduct their experiments.

Generating sequence-specific gRNAs makes the CRISPR/Cas9 system an appealing method for genome editing in many models, including fruit flies. From the initial cloning steps to screening for the transgenic flies, stable lines with CRISPR/Cas9-mediated modifications can be generated rapidly (within a month) [141]. By using the CRISPR/Cas9 system, researchers can

generate precise, heritable genomic modifications in *Drosophila*. With CRISPR/Cas9-mediated genome editing, rapid engineering of the genome and generation of mutant lines allows researchers to interrogate gene function.

A goal of the nationwide research endeavor, *Drosophila* Gene Disruption Project (GDP), is to generate genetic mutant fly lines that can be used to study the function of each gene – some analyses for these mutant lines might include assessing the loss-of-function phenotypes, the cell types that express the gene, the subcellular protein localizations [117–119]. The Bloomington *Drosophila* Stock Center houses roughly 77,000 fly lines (updated since 2020), and 20, 247 of those lines are genetic mutants generated from GDP [118,119]. Yet, of these genetic mutant fly lines, there are roughly 2,000 genes that do not have an associated mutant fly line, making genetic studies for these genes difficult in fruit flies. In Chapter 3, we discuss a CRISPR/Cas9-mediated approach that may be useful for generating mutant fly lines in a rapid, scalable manner.

1.9 SPLIT FLUORESCENT PROTEINS FOR DETECTING PROTEIN INTERACTIONS

Fluorescent proteins (FPs) are indispensable tools that underlie how we visualize proteins within a live cellular context [142,143]. What is more fascinating are some of the derivatives from the original FPs. Previous works have shown that FPs can be split into two, smaller non-fluorescent components, and moreover, these split components, when expressed together, can reconstitute into a functional FP [144–149] This bipartite fluorescence complementation has been a powerful approach in studying native protein localization and protein aggregations – where a protein of interest can be fused with a short FP tag rather than the bulky, full-length FP [32,144,145,150–152]. One limitation to note: the split bipartite FP system, originally conceptualized for visualizing protein-protein interaction, has the limitation of spontaneous self-assembly between the two

fragments [146,147,153] – thus, it can be difficult distinguishing a true interaction event from a false positive signal.

Enter the split tripartite GFP system. As the name suggests, the GFP can be further split into three components – in which the two smallest fragments are fused respectively to the protein interaction partners. The split tripartite GFP system utilizes two small, non-fluorescent fragments (~20 amino acids) in proximity–10^{th} β-strand fragment and 11^{th} β-strand fragment – in a target cell expressing the 1-9^{th} β-strand barrel; all three components complement each other and reconstitute into its fluorescent complex [154]. Currently, the tripartite GFP system is spectrally limited to only green channel (excitation 488nm / emission 518nm) to study one protein-protein interaction at a single time. However, many preexisting technologies utilize the green emission spectrum, and thus, it can be difficult to distinguish between the different fluorescent signals – especially when studying multiple proteins simultaneously. In Chapter 4, we propose the tripartite mRuby4 system as a potential, red-colored sensor for studying protein interaction within a live cell.

1.10 FIGURES

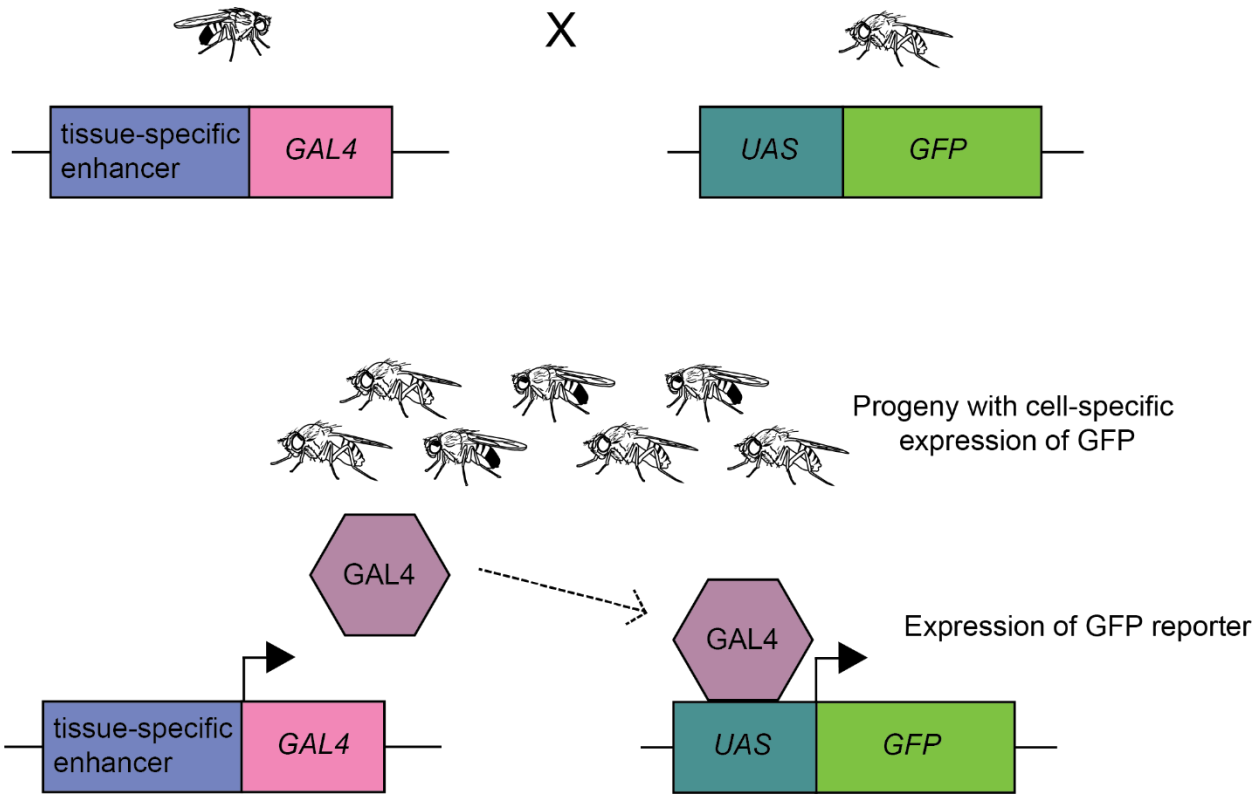

Figure 1.1 | UAS/GAL4 system for cell-specific labeling in *Drosophila* Schematic of the yeast-derived bipartite UAS/GAL4 system for cell-specific labeling or targeting. One parent fly (top left) contains a transgene for GAL4 transcription factor (pink rectangle) under the endogenous tissue-specific enhancer (indigo rectangle). The other parent fly (top right) contains a Green Fluorescent Protein (GFP) reporter cassette (green rectangle) downstream of the Upstream Activation Sequence (UAS) (teal rectangle) – this parent fly does not express GFP due to the absence of GAL4 binding to UAS. When the two parent flies cross, progenies will have cells that express GAL4 and UAS reporter. Tissue-specific GAL4 proteins (purple hexagon) can bind to UAS, inducing expression of the reporter transgene (in this example, GFP).

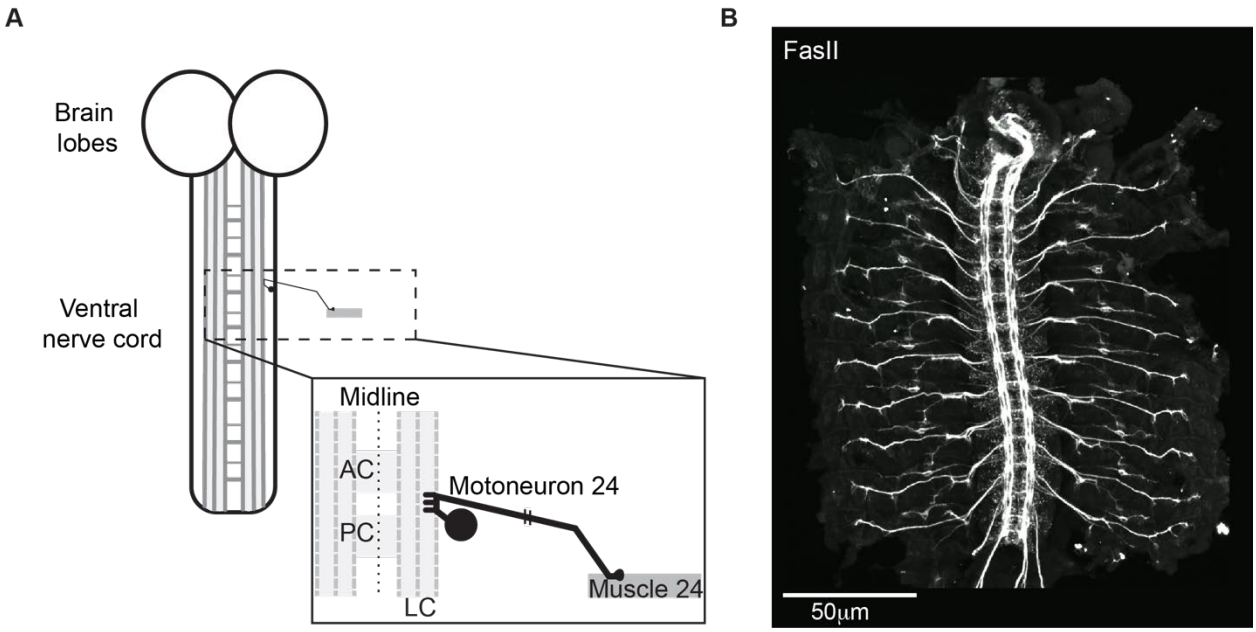

Figure 1.2 | Stereotyped CNS organization in the fly embryo to study motoneuron development (a) Cartoon schematic of embryonic CNS consisting of the brain lobes and ventral nerve cord (VNC). The segmented VNC contains multiple neuromeres – in this schematic, we show 8 neuromeres for simplificity. The cartoon inset shows a zoom-in of the dashed rectangle. Many axon tracts bundle together to give rise to commissure structures – which make up the ladder-shaped pattern within the VNC. The long parts of the ladder is the longitudinal commissure (LC), where three major axonal fascicles reside (gray dashed lines). The short parts of the ladder are the anterior commissure (AC) and posterior commissure (PC). Motoneurons project their axons and dendrites (collectively referred to as neurites) within these commissures before projecting out to the peripheral field and innervating their specific muscle targets. In this cartoon, we show motoneuron 24 as an example. The long process (axon) projects from the cell body towards the longitudinal commissure, specifically the outmost axonal fascicle, before innervating muscle 24 (gray rectangle). The shorter processes (dendrites) project from the axon along the outmost axonal fascicle. In Chapter 2, we investigate further this stereotyped placement of motoneuron 24's axon and dendrite projections. **(b)** Embryo fillet dissection showing the accessible CNS. The embryo is

immunostained with anti-FasII antibody (gray) to study the CNS neuron projections (which include axons and dendrites). Note that this fillet dissection also includes the intact body wall muscles – in which these cells are targets of innervation by motoneurons. Because we can visualize the axon terminals, we can employ approaches such as retrograde lipophilic dye-labeling in order to study motoneurons at a single-cell resolution. Scale bar, 50 μm.

1.11 REFERENCES

[1] Ramón y Cajal S., Leyes de la morfología y dinamismo de las célulasnerviosas, Rev. Trimest. Micrográfica. (1897).

[2] S.R. y Cajal, Histologie du système nerveux de l'homme & des vertébrés: Cervelet, cerveau moyen, rétine, couche optique, corps strié, écorce cérébrale générale & régionale, grand sympathique., A. Maloine. 2 (1911).

[3] S. Ramón y Cajal, La fine structure des centres nerveux, Proceedins R. Soc. London. 55 (1894).

[4] S. Herculano-Houzel, The human brain in numbers: A linearly scaled-up primate brain, Front. Hum. Neurosci. 3 (2009). https://doi.org/10.3389/neuro.09.031.2009.

[5] B.J. He, G.L. Shulman, A.Z. Snyder, M. Corbetta, The role of impaired neuronal communication in neurological disorders, Curr. Opin. Neurol. 20 (2007). https://doi.org/10.1097/WCO.0b013e3282f1c720.

[6] M. Wong, D. Guo, Dendritic spine pathology in epilepsy: Cause or consequence?, Neuroscience. 251 (2013). https://doi.org/10.1016/j.neuroscience.2012.03.048.

[7] N.E. Rosen, C. Lord, F.R. Volkmar, The Diagnosis of Autism: From Kanner to DSM-III to DSM-5 and Beyond, J. Autism Dev. Disord. 51 (2021). https://doi.org/10.1007/s10803-021-04904-1.

[8] A.A. Nugent, A.L. Kolpak, E.C. Engle, Human disorders of axon guidance, Curr. Opin. Neurobiol. 22 (2012). https://doi.org/10.1016/j.conb.2012.02.006.

[9] R. Cooper, Diagnostic and statistical manual of mental disorders (DSM), Knowl. Organ. 44 (2017). https://doi.org/10.5771/0943-7444-2017-8-668.

[10] K. Furusawa, K. Emoto, Scrap and Build for Functional Neural Circuits: Spatiotemporal

Regulation of Dendrite Degeneration and Regeneration in Neural Development and Disease, Front. Cell. Neurosci. 14 (2021). https://doi.org/10.3389/fncel.2020.613320.

[11] L. Moons, L. De Groef, Molecular mechanisms of neural circuit development and regeneration, Int. J. Mol. Sci. 22 (2021). https://doi.org/10.3390/ijms22094593.

[12] T.H. Morgan, Sex limited inheritance in drosophila, Science (80-.). 32 (1910). https://doi.org/10.1126/science.32.812.120.

[13] T.H. Morgan, What are "Factors" in Mendelian explanations?, J. Hered. os-5 (1909). https://doi.org/10.1093/jhered/os-5.1.365.

[14] S. Yamamoto, M. Jaiswal, W.L. Charng, T. Gambin, E. Karaca, G. Mirzaa, W. Wiszniewski, H. Sandoval, N.A. Haelterman, B. Xiong, K. Zhang, V. Bayat, G. David, T. Li, K. Chen, U. Gala, T. Harel, D. Pehlivan, S. Penney, L.E.L.M. Vissers, J. De Ligt, S.N. Jhangiani, Y. Xie, S.H. Tsang, Y. Parman, M. Sivaci, E. Battaloglu, D. Muzny, Y.W. Wan, Z. Liu, A.T. Lin-Moore, R.D. Clark, C.J. Curry, N. Link, K.L. Schulze, E. Boerwinkle, W.B. Dobyns, R. Allikmets, R.A. Gibbs, R. Chen, J.R. Lupski, M.F. Wangler, H.J. Bellen, A drosophila genetic resource of mutants to study mechanisms underlying human genetic diseases, Cell. 159 (2014). https://doi.org/10.1016/j.cell.2014.09.002.

[15] B. Ugur, K. Chen, H.J. Bellen, Drosophila tools and assays for the study of human diseases, DMM Dis. Model. Mech. 9 (2016). https://doi.org/10.1242/dmm.023762.

[16] S. Chien, L.T. Reiter, E. Bier, M. Gribskov, Homophila: Human disease gene cognates in Drosophila, Nucleic Acids Res. 30 (2002). https://doi.org/10.1093/nar/30.1.149.

[17] I. Ueoka, H.T.N. Pham, K. Matsumoto, M. Yamaguchi, Autism spectrum disorder-related syndromes: Modeling with drosophila and rodents, Int. J. Mol. Sci. 20 (2019).

https://doi.org/10.3390/ijms20174071.

[18] Y. Xiong, J. Yu, Modeling Parkinson's disease in Drosophila: What have we learned for dominant traits?, Front. Neurol. 9 (2018). https://doi.org/10.3389/fneur.2018.00228.

[19] M.B. Feany, W.W. Bender, A Drosophila model of Parkinson's disease, Nature. 404 (2000). https://doi.org/10.1038/35006074.

[20] K. Prüßing, A. Voigt, J.B. Schulz, Drosophila melanogaster as a model organism for Alzheimer's disease, Mol. Neurodegener. 8 (2013). https://doi.org/10.1186/1750-1326-8-35.

[21] A. Ullrich, M.A. Böhme, J. Schöneberg, H. Depner, S.J. Sigrist, F. Noé, Dynamical Organization of Syntaxin-1A at the Presynaptic Active Zone, PLoS Comput. Biol. 11 (2015). https://doi.org/10.1371/journal.pcbi.1004407.

[22] K.T. Chang, Y.J. Shi, K.T. Min, The Drosophila homolog of Down's syndrome critical region 1 gene regulates learning: Implications for mental retardation, Proc. Natl. Acad. Sci. U. S. A. 100 (2003). https://doi.org/10.1073/pnas.2536696100.

[23] A.H. Brand, N. Perrimon, Targeted gene expression as a means of altering cell fates and generating dominant phenotypes, Development. 118 (1993). https://doi.org/10.1242/dev.118.2.401.

[24] J.B. Duffy, GAL4 system in Drosophila: A fly geneticist's Swiss army knife, Genes. (United States). 34 (2002). https://doi.org/10.1002/gene.10150.

[25] J.A. Fischer, E. Giniger, T. Maniatis, M. Ptashne, GAL4 activates transcription in Drosophila, Nature. 332 (1988). https://doi.org/10.1038/332853a0.

[26] M. Johnston, J. Dover, Mutational analysis of the GAL4-encoded transcriptional activator protein of Saccharomyces cerevisiae, Genetics. 120 (1988).

https://doi.org/10.1093/genetics/120.1.63.

[27] J. Ma, M. Ptashne, Deletion analysis of GAL4 defines two transcriptional activating segments, Cell. 48 (1987). https://doi.org/10.1016/0092-8674(87)90081-X.

[28] S.J. Gratz, C.D. Rubinstein, M.M. Harrison, J. Wildonger, K.M. O'Connor-Giles, CRISPR-Cas9 genome editing in Drosophila, Curr. Protoc. Mol. Biol. (2015). https://doi.org/10.1002/0471142727.mb3102s111.

[29] S.J. Gratz, A.M. Cummings, J.N. Nguyen, D.C. Hamm, L.K. Donohue, M.M. Harrison, J. Wildonger, K.M. O'connor-Giles, Genome engineering of Drosophila with the CRISPR RNA-guided Cas9 nuclease, Genetics. (2013). https://doi.org/10.1534/genetics.113.152710.

[30] S.J. Gratz, F.P. Ukken, C.D. Rubinstein, G. Thiede, L.K. Donohue, A.M. Cummings, K.M. Oconnor-Giles, Highly specific and efficient CRISPR/Cas9-catalyzed homology-directed repair in Drosophila, Genetics. (2014). https://doi.org/10.1534/genetics.113.160713.

[31] S. Lin, B.T. Staahl, R.K. Alla, J.A. Doudna, Enhanced homology-directed human genome engineering by controlled timing of CRISPR/Cas9 delivery, Elife. (2014). https://doi.org/10.7554/eLife.04766.

[32] D. Kamiyama, S. Sekine, B. Barsi-rhyne, J. Hu, B. Chen, L.A. Gilbert, H. Ishikawa, M.D. Leonetti, W.F. Marshall, J.S. Weissman, B. Huang, Versatile protein tagging in cells with split fluorescent protein, Nat. Commun. 7 (2016) 1–9. https://doi.org/10.1038/ncomms11046.

[33] B.H. Jennings, Drosophila-a versatile model in biology & medicine, Mater. Today. 14 (2011). https://doi.org/10.1016/S1369-7021(11)70113-4.

[34] N.S. Tolwinski, Introduction: Drosophila-A model system for developmental biology, J. Dev. Biol. 5 (2017). https://doi.org/10.3390/jdb5030009.

[35] S.T. Crews, Drosophila embryonic CNS development: Neurogenesis, gliogenesis, cell fate, and differentiation, Genetics. 213 (2019). https://doi.org/10.1534/genetics.119.300974.

[36] E.S. Heckscher, F. Long, M.J. Layden, C.H. Chuang, L. Manning, J. Richart, J.C. Pearson, S.T. Crews, H. Peng, E. Myers, C.Q. Doe, Atlas-builder software and the eNeuro atlas: Resources for developmental biology and neuroscience, Dev. 141 (2014). https://doi.org/10.1242/dev.108720.

[37] K. Ito, J. Urban, G.M. Technau, Distribution, classification, and development of Drosophila glial cells in the late embryonic and early larval ventral nerve cord, Roux's Arch. Dev. Biol. 204 (1995). https://doi.org/10.1007/BF02179499.

[38] L.K. Scheffer, C.S. Xu, M. Januszewski, Z. Lu, S.Y. Takemura, K.J. Hayworth, G.B. Huang, K. Shinomiya, J. Maitin-Shepard, S. Berg, J. Clements, P.M. Hubbard, W.T. Katz, L. Umayam, T. Zhao, D. Ackerman, T. Blakely, J. Bogovic, T. Dolafi, D. Kainmueller, T. Kawase, K.A. Khairy, L. Leavitt, P.H. Li, L. Lindsey, N. Neubarth, D.J. Olbris, H. Otsuna, E.T. Trautman, M. Ito, A.S. Bates, J. Goldammer, T. Wolff, R. Svirskas, P. Schlegel, E.R. Neace, C.J. Knecht, C.X. Alvarado, D.A. Bailey, S. Ballinger, J.A. Borycz, B.S. Canino, N. Cheatham, M. Cook, M. Dreher, O. Duclos, B. Eubanks, K. Fairbanks, S. Finley, N. Forknall, A. Francis, G.P. Hopkins, E.M. Joyce, S. Kim, N.A. Kirk, J. Kovalyak, S.A. Lauchie, A. Lohff, C. Maldonado, E.A. Manley, S. McLin, C. Mooney, M. Ndama, O. Ogundeyi, N. Okeoma, C. Ordish, N. Padilla, C. Patrick, T. Paterson, E.E. Phillips, E.M. Phillips, N. Rampally, C. Ribeiro, M.K. Robertson, J.T. Rymer, S.M. Ryan,

M. Sammons, A.K. Scott, A.L. Scott, A. Shinomiya, C. Smith, K. Smith, N.L. Smith, M.A. Sobeski, A. Suleiman, J. Swift, S. Takemura, I. Talebi, D. Tarnogorska, E. Tenshaw, T. Tokhi, J.J. Walsh, T. Yang, J.A. Horne, F. Li, R. Parekh, P.K. Rivlin, V. Jayaraman, M. Costa, G.S.X.E. Jefferis, K. Ito, S. Saalfeld, R. George, I.A. Meinertzhagen, G.M. Rubin, H.F. Hess, V. Jain, S.M. Plaza, A connectome and analysis of the adult drosophila central brain, Elife. 9 (2020). https://doi.org/10.7554/ELIFE.57443.

[39] I. Hayashi, M. Perez-Magallanes, Establishment of pure neuronal and muscle precursor cell cultures from Drosophila early gastrula stage embryos, Vitr. Cell. Dev. Biol. - Anim. J. Soc. Vitr. Biol. 30 (1994). https://doi.org/10.1007/BF02632041.

[40] A. Martinez-Arias, P.A. Lawrence, Parasegments and compartments in the Drosophila embryo, Nature. 313 (1985). https://doi.org/10.1038/313639a0.

[41] J.B. Skeath, Y. Zhang, R. Holmgren, S.B. Carroll, C.Q. Doe, Specification of neuroblast identity in the drosophila embryonic central nervous system by gooseberry-distal, Nature. 376 (1995). https://doi.org/10.1038/376427a0.

[42] M.A. Inal, K. Banzai, D. Kamiyama, Retrograde tracing of Drosophila embryonic motor neurons using lipophilic fluorescent dyes, J. Vis. Exp. 2020 (2019). https://doi.org/10.3791/60716.

[43] M. Landgraf, N. Sánchez-Soriano, G.M. Technau, J. Urban, A. Prokop, Charting the Drosophila neuropile: A strategy for the standardised characterisation of genetically amenable neurites, Dev. Biol. 260 (2003). https://doi.org/10.1016/S0012-1606(03)00215-X.

[44] M. Landgraf, T. Bossing, G.M. Technau, M. Bate, The origin, location, and projections of the embryonic abdominal motorneurons of Drosophila, J. Neurosci. 17 (1997).

https://doi.org/10.1523/jneurosci.17-24-09642.1997.

[45] C. Rickert, T. Kunz, K.L. Harris, P.M. Whitington, G.M. Technau, Morphological characterization of the entire interneuron population reveals principles of neuromere organization in the Ventral nerve cord of Drosophila, J. Neurosci. 31 (2011). https://doi.org/10.1523/JNEUROSCI.4009-11.2011.

[46] M. Landgraf, V. Jeffrey, M. Fujioka, J.B. Jaynes, M. Bate, Embryonic origins of a motor system: Motor dendrites form a myotopic map in Drosophila, PLoS Biol. 1 (2003). https://doi.org/10.1371/journal.pbio.0000041.

[47] M.D. Kim, Y. Wen, Y.N. Jan, Patterning and organization of motor neuron dendrites in the Drosophila larva, Dev. Biol. 336 (2009) 213–221. https://doi.org/10.1016/J.YDBIO.2009.09.041.

[48] S. Saalfeld, A. Cardona, V. Hartenstein, P. Tomančák, CATMAID: Collaborative annotation toolkit for massive amounts of image data, Bioinformatics. 25 (2009). https://doi.org/10.1093/bioinformatics/btp266.

[49] C. Albert, Web-based collaborative neuronal reconstruction with CATMAID, Front. Neuroinform. 5 (2011). https://doi.org/10.3389/conf.fninf.2011.08.00093.

[50] D. Kamiyama, R. McGorty, R. Kamiyama, M.D. Kim, A. Chiba, B. Huang, Specification of Dendritogenesis Site in Drosophila aCC Motoneuron by Membrane Enrichment of Pak1 through Dscam1, Dev. Cell. 35 (2015). https://doi.org/10.1016/j.devcel.2015.09.007.

[51] C.N.G. Giachello, I. Hunter, T. Pettini, B. Coulson, A. Knüfer, S. Cachero, M. Winding, A.A. Zarin, H. Kohsaka, Y.N. Fan, A. Nose, M. Landgraf, R.A. Baines, Electrophysiological Validation of Monosynaptic Connectivity between Premotor Interneurons and the aCC Motoneuron in the Drosophila Larval CNS, J. Neurosci. 42

(2022). https://doi.org/10.1523/JNEUROSCI.2463-21.2022.

[52] S.D. Ackerman, N.A. Perez-Catalan, M.R. Freeman, C.Q. Doe, Astrocytes close a motor circuit critical period, Nature. 592 (2021). https://doi.org/10.1038/s41586-021-03441-2.

[53] L.F.J. Howard, H.E. Brown, B.C. Wadsworth, T.A. Evans, Midline axon guidance in the Drosophila embryonic central nervous system, Semin. Cell Dev. Biol. 85 (2019). https://doi.org/10.1016/j.semcdb.2017.11.029.

[54] T.A. Evans, G.J. Bashaw, Axon guidance at the midline: of mice and flies, Curr. Opin. Neurobiol. 20 (2010). https://doi.org/10.1016/j.conb.2009.12.006.

[55] M. Tessier-Lavigne, C.S. Goodman, The molecular biology of axon guidance, Science (80-.). 274 (1996). https://doi.org/10.1126/science.274.5290.1123.

[56] M.P. Furrer, I. Vasenkova, D. Kamiyama, Y. Rosado, A. Chiba, Slit and Robo control the development of dendrites in Drosophila CNS, Development. 134 (2007). https://doi.org/10.1242/dev.02882.

[57] D.M. Lin, V.J. Auld, C.S. Goodman, Targeted neuronal cell ablation in the drosophila embryo: Pathfinding by follower growth cones in the absence of pioneers, Neuron. 14 (1995). https://doi.org/10.1016/0896-6273(95)90215-5.

[58] H. Long, C. Sabatier, L. Ma, A. Plump, W. Yuan, D.M. Ornitz, A. Tamada, F. Murakami, C.S. Goodman, M. Tessier-Lavigne, Conserved roles for Slit and Robo proteins in midline commissural axon guidance, Neuron. 42 (2004). https://doi.org/10.1016/S0896-6273(04)00179-5.

[59] K.J. Mitchell, J.L. Doyle L., T. Serafini, T.E. Kennedy, M. Tessier-Lavigne, C.S. Goodman, B.J. Dickson, Genetic analysis of Netrin genes in Drosophila: Netrins guide CNS commissural axons and peripheral motor axons, Neuron. 17 (1996).

https://doi.org/10.1016/S0896-6273(00)80153-1.

[60] M. Hiramoto, Y. Hiromi, E. Giniger, Y. Hotta, The Drosophila netrin receptor Frazzled guides axons by controlling Netrin distribution, Nature. 406 (2000). https://doi.org/10.1038/35022571.

[61] N.J. Ramirez-Suarez, H.M. Belalcazar, C.J. Salazar, B. Beyaz, B. Raja, K.C.Q. Nguyen, K. Celestrin, J. Fredens, N.J. Færgeman, D.H. Hall, H.E. Bülow, Axon-Dependent Patterning and Maintenance of Somatosensory Dendritic Arbors, Dev. Cell. 48 (2019). https://doi.org/10.1016/j.devcel.2018.12.015.

[62] T. Kidd, K. Brose, K.J. Mitchell, R.D. Fetter, M. Tessier-Lavigne, C.S. Goodman, G. Tear, Roundabout controls axon crossing of the CNS midline and defines a novel subfamily of evolutionarily conserved guidance receptors, Cell. 92 (1998). https://doi.org/10.1016/S0092-8674(00)80915-0.

[63] T. Kidd, K.S. Bland, C.S. Goodman, Slit is the midline repellent for the Robo receptor in Drosophila, Cell. 96 (1999). https://doi.org/10.1016/S0092-8674(00)80589-9.

[64] R. Harris, L.M. Sabatelli, M.A. Seeger, Guidance cues at the Drosophila CNS midline: Identification and characterization of two Drosophila Netrin/UNC-6 homologs, Neuron. 17 (1996). https://doi.org/10.1016/S0896-6273(00)80154-3.

[65] M.P. Furrer, S. Kim, B. Wolf, A. Chiba, Robo and Frazzled/DCC mediate dendritic guidance at the CNS midline, Nat. Neurosci. 6 (2003). https://doi.org/10.1038/nn1017.

[66] J.H. Simpson, T. Kidd, K.S. Bland, C.S. Goodman, Short-range and long-range guidance by Slit and its robo receptors: Robo and Robo2 play distinct roles in midline guidance, Neuron. 28 (2000). https://doi.org/10.1016/S0896-6273(00)00151-3.

[67] M. Brankatschk, B.J. Dickson, Netrins guide Drosophila commissural axons at short

range, Nat. Neurosci. 9 (2006). https://doi.org/10.1038/nn1625.

[68] G.L. Andrews, S. Tanglao, W.T. Farmer, S. Morin, S. Brotman, M.A. Berberoglu, H. Price, G.C. Fernandez, G.S. Mastick, F. Charron, T. Kidd, Dscam guides embryonic axons by Netrin-dependent and -independent functions, Development. 135 (2008). https://doi.org/10.1242/dev.023739.

[69] C. Organisti, I. Hein, I.C. Grunwald Kadow, T. Suzuki, Flamingo, a seven-pass transmembrane cadherin, cooperates with Netrin/Frazzled in Drosophila midline guidance, Genes to Cells. 20 (2015). https://doi.org/10.1111/gtc.12202.

[70] A. Ly, A. Nikolaev, G. Suresh, Y. Zheng, M. Tessier-Lavigne, E. Stein, DSCAM Is a Netrin Receptor that Collaborates with DCC in Mediating Turning Responses to Netrin-1, Cell. 133 (2008). https://doi.org/10.1016/j.cell.2008.05.030.

[71] J. Huang, Y. Wang, S. Raghavan, S. Feng, K. Kiesewetter, J. Wang, Human down syndrome cell adhesion molecules (dscams) are functionally conserved with drosophila dscam[tm1] isoforms in controlling neurodevelopment, Insect Biochem. Mol. Biol. 41 (2011). https://doi.org/10.1016/j.ibmb.2011.05.008.

[72] K.L. Agarwala, S. Ganesh, K. Amano, T. Suzuki, K. Yamakawa, DSCAM, a highly conserved gene in mammals, expressed in differentiating mouse brain, Biochem. Biophys. Res. Commun. 281 (2001). https://doi.org/10.1006/bbrc.2001.4420.

[73] D. Schmucker, B. Chen, Dscam and DSCAM: Complex genes in simple animals, complex animals yet simple genes, Genes Dev. 23 (2009). https://doi.org/10.1101/gad.1752909.

[74] M.L. Montesinos, Roles for DSCAM and DSCAML1 in central nervous system development and disease., Adv. Neurobiol. 8 (2014). https://doi.org/10.1007/978-1-4614-8090-7_11.

[75] M.L. Montesinos, Local translation of the Down syndrome cell adhesion molecule (DSCAM) mRNA in the vertebrate central nervous system, J. Neurogenet. 31 (2017). https://doi.org/10.1080/01677063.2017.1391250.

[76] A.M. Garrett, A.L.D. Tadenev, R.W. Burgess, DSCAMs: Restoring balance to developmental forces, Front. Mol. Neurosci. (2012). https://doi.org/10.3389/fnmol.2012.00086.

[77] K.L. Agarwala, S. Nakamura, Y. Tsutsumi, K. Yamakawa, Down syndrome cell adhesion molecule DSCAM mediates homophilic intercellular adhesion, Mol. Brain Res. 79 (2000). https://doi.org/10.1016/S0169-328X(00)00108-X.

[78] D. Hattori, S.S. Millard, W.M. Wojtowicz, S.L. Zipursky, Dscam-mediated cell recognition regulates neural circuit formation, Annu. Rev. Cell Dev. Biol. 24 (2008). https://doi.org/10.1146/annurev.cellbio.24.110707.175250.

[79] S.E. Antonarakis, R. Lyle, E.T. Dermitzakis, A. Reymond, S. Deutsch, Chromosome 21 and Down syndrome: From genomics to pathophysiology, Nat. Rev. Genet. 5 (2004). https://doi.org/10.1038/nrg1448.

[80] S.E. Antonarakis, Down syndrome and the complexity of genome dosage imbalance, Nat. Rev. Genet. 18 (2017). https://doi.org/10.1038/nrg.2016.154.

[81] J.T. Coyle, M.L. Oster-Granite, J.D. Gearhart, The neurobiologie consequences of down syndrome, Brain Res. Bull. 16 (1986). https://doi.org/10.1016/0361-9230(86)90074-2.

[82] N. Whittle, S.B. Sartori, M. Dierssen, G. Lubec, N. Singewald, Fetal Down syndrome brains exhibit aberrant levels of neurotransmitters critical for normal brain development, Pediatrics. 120 (2007). https://doi.org/10.1542/peds.2006-3448.

[83] J.R. Korenberg, C. Bradley, C.M. Disteche, Down syndrome: Molecular mapping of the

congenital heart disease and duodenal stenosis, Am. J. Hum. Genet. 50 (1992).

[84] J.R. Korenberg, X.N. Chen, R. Schipper, Z. Sun, R. Gonsky, S. Gerwehr, N. Carpenter, C. Daumer, P. Dignan, C. Disteche, J.M. Graham, L. Hugdins, B. Mcgillivray, K. Miyazaki, N. Ogasawara, J.P. Park, R. Pagon, S. Pueschel, G. Sack, B. Say, S. Schuffenhauer, S. Soukup, T. Yamanaka, Down syndrome phenotypes: The consequences of chromosomal imbalance, Proc. Natl. Acad. Sci. U. S. A. 91 (1994). https://doi.org/10.1073/pnas.91.11.4997.

[85] J.M. Delabar, D. Theophile, Z. Rahmani, Z. Chettouh, J.L. Blouin, M. Prieur, B. Noel, P.M. Sinet, Molecular mapping of twenty-four features of Down syndrome on chromosome 21., Eur. J. Hum. Genet. 1 (1993). https://doi.org/10.1159/000472398.

[86] K. Yamakawa, Y.K. Huo, M.A. Haendel, R. Hubert, X.N. Chen, G.E. Lyons, J.R. Korenberg, DSCAM: A novel member of the immunoglobulin superfamily maps in a Down syndrome region and is involved in the development of the nervous system, Hum. Mol. Genet. 7 (1998). https://doi.org/10.1093/hmg/7.2.227.

[87] M. Yamagata, J.R. Sanes, Dscam and Sidekick proteins direct lamina-specific synaptic connections in vertebrate retina, Nature. 451 (2008). https://doi.org/10.1038/nature06469.

[88] P.G. Fuerst, A. Koizumi, R.H. Masland, R.W. Burgess, Neurite arborization and mosaic spacing in the mouse retina require DSCAM, Nature. 451 (2008). https://doi.org/10.1038/nature06514.

[89] D. Schmucker, J.C. Clemens, H. Shu, C.A. Worby, J. Xiao, M. Muda, J.E. Dixon, S.L. Zipursky, Drosophila Dscam is an axon guidance receptor exhibiting extraordinary molecular diversity, Cell. 101 (2000). https://doi.org/10.1016/S0092-8674(00)80878-8.

[90] W.M. Wojtowicz, J.J. Flanagan, S.S. Millard, S.L. Zipursky, J.C. Clemens, Alternative

splicing of Drosophila Dscam generates axon guidance receptors that exhibit isoform-specific homophilic binding, Cell. 118 (2004). https://doi.org/10.1016/j.cell.2004.08.021.

[91] Y.N. Jan, L.Y. Jan, Branching out: Mechanisms of dendritic arborization, Nat. Rev. Neurosci. 11 (2010). https://doi.org/10.1038/nrn2836.

[92] W.B. Grueber, L.Y. Jan, Y.N. Jan, Tiling of the Drosophila epidermis by multidendritic sensory neurons, Development. 129 (2002). https://doi.org/10.1242/dev.129.12.2867.

[93] W.B. Grueber, B. Ye, A.W. Moore, L.Y. Jan, Y.N. Jan, Dendrites of distinct classes of Drosophila sensory neurons show different capacities for homotypic repulsion, Curr. Biol. 13 (2003). https://doi.org/10.1016/S0960-9822(03)00207-0.

[94] R. Bodmer, Y.N. Jan, Morphological differentiation of the embryonic peripheral neurons in Drosophila, Roux's Arch. Dev. Biol. 196 (1987). https://doi.org/10.1007/BF00402027.

[95] G. Neves, J. Zucker, M. Daly, A. Chess, Stochastic yet biased expression of multiple Dscam splice variants by individual cells, Nat. Genet. 36 (2004). https://doi.org/10.1038/ng1299.

[96] J. Wang, C.T. Zugates, I.H. Liang, C.H.J. Lee, T. Lee, Drosophila Dscam is required for divergent segregation of sister branches and suppresses ectopic bifurcation of axons, Neuron. 33 (2002). https://doi.org/10.1016/S0896-6273(02)00570-6.

[97] X.L. Zhan, J.C. Clemens, G. Neves, D. Hattori, J.J. Flanagan, T. Hummel, M.L. Vasconcelos, A. Chess, S.L. Zipursky, Analysis of Dscam diversity in regulating axon guidance in Drosophila mushroom bodies, Neuron. 43 (2004). https://doi.org/10.1016/j.neuron.2004.07.020.

[98] M.E. Hughes, R. Bortnick, A. Tsubouchi, P. Bäumer, M. Kondo, T. Uemura, D. Schmucker, Homophilic Dscam Interactions Control Complex Dendrite Morphogenesis,

Neuron. 54 (2007). https://doi.org/10.1016/j.neuron.2007.04.013.

[99] B.J. Matthews, M.E. Kim, J.J. Flanagan, D. Hattori, J.C. Clemens, S.L. Zipursky, W.B. Grueber, Dendrite Self-Avoidance Is Controlled by Dscam, Cell. 129 (2007). https://doi.org/10.1016/j.cell.2007.04.013.

[100] P. Soba, S. Zhu, K. Emoto, S. Younger, S.J. Yang, H.H. Yu, T. Lee, L.Y. Jan, Y.N. Jan, Drosophila Sensory Neurons Require Dscam for Dendritic Self-Avoidance and Proper Dendritic Field Organization, Neuron. 54 (2007). https://doi.org/10.1016/j.neuron.2007.03.029.

[101] D. Hattori, Y. Chen, B.J. Matthews, L. Salwinski, C. Sabatti, W.B. Grueber, S.L. Zipursky, Robust discrimination between self and non-self neurites requires thousands of Dscam1 isoforms, Nature. 461 (2009). https://doi.org/10.1038/nature08431.

[102] N. Wilhelm, S. Kumari, N. Krick, C. Rickert, C. Duch, Dscam1 Has Diverse Neuron Type-Specific Functions in the Developing Drosophila CNS, ENeuro. 9 (2022). https://doi.org/10.1523/ENEURO.0255-22.2022.

[103] K.M. Hutchinson, F. Vonhoff, C. Duch, Dscam1 is required for normal dendrite growth and branching but not for dendritic spacing in Drosophila motoneurons, J. Neurosci. 34 (2014). https://doi.org/10.1523/JNEUROSCI.3448-13.2014.

[104] M.J. Bastiani, C.S. Goodman, Neuronal growth cones: Specific interactions mediated by filopodial insertion and induction of coated vesicles, Proc. Natl. Acad. Sci. U. S. A. 81 (1984). https://doi.org/10.1073/pnas.81.6.1849.

[105] J.A. Doudna, E. Charpentier, The new frontier of genome engineering with CRISPR-Cas9, Science (80-.). 346 (2014). https://doi.org/10.1126/science.1258096.

[106] L.J. Stadler, Mutations in barley induced by X-rays and radium, Science (80-.). 68

(1928). https://doi.org/10.1126/science.68.1756.186.

[107] M. Westergaard, Chemical mutagenesis in relation to the concept of the gene, Experientia. 13 (1957). https://doi.org/10.1007/BF02157427.

[108] B. REINER, S. ZAMENHOF, Studies on the chemically reactive groups of deoxyribonucleic acids., J. Biol. Chem. 228 (1957). https://doi.org/10.1016/s0021-9258(18)70727-8.

[109] H.O. Smith, K.W. Welcox, A Restriction enzyme from Hemophilus influenzae, J. Mol. Biol. 51 (1970). https://doi.org/10.1016/0022-2836(70)90149-x.

[110] Human genome editing: Science, ethics, and governance, 2017. https://doi.org/10.17226/24623.

[111] L.J. Stadler, Genetic Effects of X-Rays in Maize, Proc. Natl. Acad. Sci. 14 (1928). https://doi.org/10.1073/pnas.14.1.69.

[112] H.J. Muller, THE MEASUREMENT OF GENE MUTATION RATE IN DROSOPHILA, ITS HIGH VARIABILITY, AND ITS DEPENDENCE UPON TEMPERATURE, Genetics. 13 (1928). https://doi.org/10.1093/genetics/13.4.279.

[113] C.B. Bridges, DEFICIENCY, Genetics. 2 (1917). https://doi.org/10.1093/genetics/2.5.445.

[114] R.K. Cook, S.J. Christensen, J.A. Deal, R.A. Coburn, M.E. Deal, J.M. Gresens, T.C. Kaufman, K.R. Cook, The generation of chromosomal deletions to provide extensive coverage and subdivision of the Drosophila melanogaster genome, Genome Biol. 13 (2012). https://doi.org/10.1186/gb-2012-13-3-r21.

[115] B. McCLINTOCK, The origin and behavior of mutable loci in maize., Proc. Natl. Acad. Sci. U. S. A. 36 (1950). https://doi.org/10.1073/pnas.36.6.344.

[116] M. Munoz-Lopez, J. Garcia-Perez, DNA Transposons: Nature and Applications in

Genomics, Curr. Genomics. 11 (2010). https://doi.org/10.2174/138920210790886871.

[117] H.J. Bellen, R.W. Levis, Y. He, J.W. Carlson, M. Evans-Holm, E. Bae, J. Kim, A. Metaxakis, C. Savakis, K.L. Schulze, R.A. Hoskins, A.C. Spradling, The Drosophila gene disruption project: Progress using transposons with distinctive site specificities, Genetics. 188 (2011). https://doi.org/10.1534/genetics.111.126995.

[118] H.J. Bellen, R.W. Levis, G. Liao, Y. He, J.W. Carlson, G. Tsang, M. Evans-Holm, P.R. Hiesinger, K.L. Schulze, G.M. Rubin, R.A. Hoskins, A.C. Spradling, The BDGP gene disruption project: Single transposon insertions associated with 40% of Drosophila genes, Genetics. 167 (2004). https://doi.org/10.1534/genetics.104.026427.

[119] A.C. Spradling, D. Stern, A. Beaton, E.J. Rhem, T. Laverty, N. Mozden, S. Misra, G.M. Rubin, The Berkeley Drosophila Genome Project gene disruption project: Single P-element insertions mutating 25% of vital Drosophila genes, Genetics. 153 (1999). https://doi.org/10.1093/genetics/153.1.135.

[120] F.D. Urnov, E.J. Rebar, M.C. Holmes, H.S. Zhang, P.D. Gregory, Genome editing with engineered zinc finger nucleases, Nat. Rev. Genet. 11 (2010). https://doi.org/10.1038/nrg2842.

[121] J.C. Miller, S. Tan, G. Qiao, K.A. Barlow, J. Wang, D.F. Xia, X. Meng, D.E. Paschon, E. Leung, S.J. Hinkley, G.P. Dulay, K.L. Hua, I. Ankoudinova, G.J. Cost, F.D. Urnov, H.S. Zhang, M.C. Holmes, L. Zhang, P.D. Gregory, E.J. Rebar, A TALE nuclease architecture for efficient genome editing, Nat. Biotechnol. 29 (2011). https://doi.org/10.1038/nbt.1755.

[122] T. Gaj, C.A. Gersbach, C.F. Barbas, ZFN, TALEN, and CRISPR/Cas-based methods for genome engineering, Trends Biotechnol. 31 (2013). https://doi.org/10.1016/j.tibtech.2013.04.004.

[123] N.P. Pavletich, C.O. Pabo, Zinc finger-DNA recognition: Crystal structure of a Zif268-DNA complex at 2.1 Å, Science (80-.). 252 (1991). https://doi.org/10.1126/science.2028256.

[124] X. Meng, S. Thibodeau-Beganny, T. Jiang, J.K. Joung, S.A. Wolfe, Profiling the DNA-binding specificities of engineered Cys2His2 zinc finger domains using a rapid cell-based method, Nucleic Acids Res. 35 (2007). https://doi.org/10.1093/nar/gkm385.

[125] M.L. Maeder, S. Thibodeau-Beganny, A. Osiak, D.A. Wright, R.M. Anthony, M. Eichtinger, T. Jiang, J.E. Foley, R.J. Winfrey, J.A. Townsend, E. Unger-Wallace, J.D. Sander, F. Müller-Lerch, F. Fu, J. Pearlberg, C. Göbel, J.P.P. Dassie, S.M. Pruett-Miller, M.H. Porteus, D.C. Sgroi, A.J. Iafrate, D. Dobbs, P.B. McCray, T. Cathomen, D.F. Voytas, J.K. Joung, Rapid "Open-Source" Engineering of Customized Zinc-Finger Nucleases for Highly Efficient Gene Modification, Mol. Cell. 31 (2008). https://doi.org/10.1016/j.molcel.2008.06.016.

[126] J. Boch, H. Scholze, S. Schornack, A. Landgraf, S. Hahn, S. Kay, T. Lahaye, A. Nickstadt, U. Bonas, Breaking the code of DNA binding specificity of TAL-type III effectors, Science (80-.). 326 (2009). https://doi.org/10.1126/science.1178811.

[127] M.J. Moscou, A.J. Bogdanove, A simple cipher governs DNA recognition by TAL effectors, Science (80-.). 326 (2009). https://doi.org/10.1126/science.1178817.

[128] A.C. Mercer, T. Gaj, R.P. Fuller, C.F. Barbas, Chimeric TALE recombinases with programmable DNA sequence specificity, Nucleic Acids Res. 40 (2012). https://doi.org/10.1093/nar/gks875.

[129] T. Cermak, E.L. Doyle, M. Christian, L. Wang, Y. Zhang, C. Schmidt, J.A. Baller, N. V. Somia, A.J. Bogdanove, D.F. Voytas, Efficient design and assembly of custom TALEN

and other TAL effector-based constructs for DNA targeting, Nucleic Acids Res. 39 (2011). https://doi.org/10.1093/nar/gkr218.

[130] A.W. Briggs, X. Rios, R. Chari, L. Yang, F. Zhang, P. Mali, G.M. Church, Iterative capped assembly: Rapid and scalable synthesis of repeat-module DNA such as TAL effectors from individual monomers, Nucleic Acids Res. 40 (2012). https://doi.org/10.1093/nar/gks624.

[131] D. Reyon, S.Q. Tsai, C. Khgayter, J.A. Foden, J.D. Sander, J.K. Joung, FLASH assembly of TALENs for high-throughput genome editing, Nat. Biotechnol. 30 (2012). https://doi.org/10.1038/nbt.2170.

[132] L.S. Qi, M.H. Larson, L.A. Gilbert, J.A. Doudna, J.S. Weissman, A.P. Arkin, W.A. Lim, Repurposing CRISPR as an RNA-Guided Platform for Sequence-Specific Control of Gene Expression, Cell. 152 (2013) 1173–1183. https://doi.org/10.1016/J.CELL.2013.02.022.

[133] B. Wiedenheft, S.H. Sternberg, J.A. Doudna, RNA-guided genetic silencing systems in bacteria and archaea, Nature. 482 (2012). https://doi.org/10.1038/nature10886.

[134] K.S. Makarova, E. V. Koonin, Annotation and classification of CRISPR-Cas systems, Methods Mol. Biol. 1311 (2015). https://doi.org/10.1007/978-1-4939-2687-9_4.

[135] M. Jinek, K. Chylinski, I. Fonfara, M. Hauer, J.A. Doudna, E. Charpentier, A programmable dual-RNA-guided DNA endonuclease in adaptive bacterial immunity, Science (80-.). 337 (2012). https://doi.org/10.1126/science.1225829.

[136] G. Gasiunas, R. Barrangou, P. Horvath, V. Siksnys, Cas9-crRNA ribonucleoprotein complex mediates specific DNA cleavage for adaptive immunity in bacteria, Proc. Natl. Acad. Sci. U. S. A. 109 (2012). https://doi.org/10.1073/pnas.1208507109.

[137] N. Chang, C. Sun, L. Gao, D. Zhu, X. Xu, X. Zhu, J.W. Xiong, J.J. Xi, Genome editing

with RNA-guided Cas9 nuclease in Zebrafish embryos, Cell Res. 23 (2013). https://doi.org/10.1038/cr.2013.45.

[138] B. Shen, J. Zhang, H. Wu, J. Wang, K. Ma, Z. Li, X. Zhang, P. Zhang, X. Huang, Generation of gene-modified mice via Cas9/RNA-mediated gene targeting, Cell Res. 23 (2013). https://doi.org/10.1038/cr.2013.46.

[139] J.E. Garneau, M.È. Dupuis, M. Villion, D.A. Romero, R. Barrangou, P. Boyaval, C. Fremaux, P. Horvath, A.H. Magadán, S. Moineau, The CRISPR/cas bacterial immune system cleaves bacteriophage and plasmid DNA, Nature. 468 (2010). https://doi.org/10.1038/nature09523.

[140] J.E. Dicarlo, J.E. Norville, P. Mali, X. Rios, J. Aach, G.M. Church, Genome engineering in Saccharomyces cerevisiae using CRISPR-Cas systems, Nucleic Acids Res. 41 (2013). https://doi.org/10.1093/nar/gkt135.

[141] S.J. Gratz, M.M. Harrison, J. Wildonger, K.M. O'connor-Giles, Precise genome editing of drosophila with CRISPR RNA- guided cas9, Methods Mol. Biol. 1311 (2015). https://doi.org/10.1007/978-1-4939-2687-9_22.

[142] R.Y. Tsien, THE GREEN FLUORESCENT PROTEIN, Annu. Rev. Biochem. 67 (1998) 509–544. https://doi.org/https://doi.org/10.1146/annurev.biochem.67.1.509.

[143] F.G. Prendergast, K.G. Mann, Chemical and Physical Properties of Aequorin and the Green Fluorescent Protein Isolated from Aequorea forskålea†, Biochemistry. 17 (1978). https://doi.org/10.1021/bi00610a004.

[144] S. Cabantous, T.C. Terwilliger, G.S. Waldo, Protein tagging and detection with engineered self-assembling fragments of green fluorescent protein, Nat. Biotechnol. 23 (2005). https://doi.org/10.1038/nbt1044.

[145] S. Cabantous, G.S. Waldo, In vivo and in vitro protein solubility assays using split GFP, Nat. Methods. 3 (2006). https://doi.org/10.1038/nmeth932.

[146] C.-D. Hu, Y. Chinenov, T.K. Kerppola, Visualization of Interactions among bZIP and Rel Family Proteins in Living Cells Using Bimolecular Fluorescence Complementation, Mol. Cell. 9 (2002) 789–798. https://doi.org/10.1016/S1097-2765(02)00496-3.

[147] C.D. Hu, T.K. Kerppola, Simultaneous visualization of multiple protein interactions in living cells using multicolor fluorescence complementation analysis, Nat. Biotechnol. (2003). https://doi.org/10.1038/nbt816.

[148] T.K. Kerppola, Design and implementation of bimolecular fluorescence complementation (BiFC) assays for the visualization of protein interactions in living cells, Nat. Protoc. (2006). https://doi.org/10.1038/nprot.2006.201.

[149] Z. Wang, G. Palmer, L.C. Griffith, Regulation of Drosophila Ca2+/calmodulin-dependent protein kinase II by autophosphorylation analyzed by site-directed mutagenesis, J. Neurochem. 71 (1998). https://doi.org/10.1046/j.1471-4159.1998.71010378.x.

[150] R. Tamura, F. Jiang, J. Xie, D. Kamiyama, Multiplexed labeling of cellular proteins with split fluorescent protein tags, Commun. Biol. 4 (2021). https://doi.org/10.1038/s42003-021-01780-4.

[151] S. Feng, A. Varshney, D.C. Villa, C. Modavi, J. Kohler, F. Farah, Bright split red fluorescent proteins with enhanced complementation efficiency for the tagging of endogenous proteins and visualization of synapses, Nat. Commun. 8 (2018).

[152] S. Feng, S. Sekine, V. Pessino, H. Li, M.D. Leonetti, B. Huang, Improved split fluorescent proteins for endogenous protein labeling, Nat. Commun. 8 (2017) 370. https://doi.org/10.1038/s41467-017-00494-8.

[153] A. Horstman, I.A.N. Tonaco, K. Boutilier, R.G.H. Immink, A Cautionary note on the use of split-YFP/BiFC in plant protein-protein interaction studies, Int. J. Mol. Sci. (2014). https://doi.org/10.3390/ijms15069628.

[154] S. Cabantous, H.B. Nguyen, J.-D. Pedelacq, F. Koraïchi, A. Chaudhary, K. Ganguly, M.A. Lockard, G. Favre, T.C. Terwilliger, G.S. Waldo, A New Protein-Protein Interaction Sensor Based on Tripartite Split-GFP Association, Sci. Rep. 3 (2013) 2854. https://doi.org/10.1038/srep02854.

CHAPTER 2

ADJACENT NEURONAL FASCICLE GUIDES MOTONEURON 24 DENDRITIC BRANCHING AND AXONAL ROUTING DECISIONS THROUGH DSCAM1 SIGNALING[1]

[1] Bui, K. C. and Kamiyama, D. Submitted to *Journal of Neuroscience.*

2.1 ABSTRACT

The formation and precise positioning of axons and dendrites are crucial for the development of neural circuits. Although juxtracrine signaling via cell-cell contact is known to influence these processes, the specific structures and mechanisms regulating neuronal process positioning within the central nervous system (CNS) remain to be fully identified. Our study investigates motoneuron 24 (MN24) in the *Drosophila* embryonic CNS, which is characterized by a complex yet stereotyped axon projection pattern, known as 'axonal routing.' In this motoneuron, the primary dendritic branches project laterally toward the midline, specifically emerging at the sites where axons turn. We observed that *Scp2*-positive neurons contribute to the lateral fascicle structure in the ventral nerve cord (VNC) near MN24 dendrites. Notably, the knockout of the Down syndrome cell adhesion molecule (*dscam1*) results in the loss of dendrites and disruption of proper axonal routing in MN24, while not affecting the formation of the fascicle structure. Through cell-type specific knockdown and rescue experiments of *dscam1*, we have determined that the interaction between MN24 and *Scp2*-positive fascicle, mediated by Dscam1, promotes the development of both dendrites and axonal routing. Our findings demonstrate that the holistic configuration of neuronal structures, such as axons and dendrites, within single motoneurons can be governed by local contact with the adjacent neuron fascicle, a novel reference structure for neural circuitry wiring. Given the occurrence of analogous axon fascicle formations within the vertebrate spinal cord, such structures may play a conserved role in the morphogenesis of motoneurons via Dscam1 across phyla.

2.2 INTRODUCTION

The precise positioning of axons and dendrites is crucial for neuronal function [1-4]. Notably, during early embryonic stages, the construction of the circuit occurs independently of neuronal activities, relying solely on the developmental program [5-8]. In this embryonic context, extracellular cues play a critical role in neural circuitry development, providing vital spatial information that guides the growth, directional shifts, and arborization of these neural structures [9-11]. A notable example of spatial regulation in neuronal processes is evident in the decision-making of repulsion and attraction at the midline within the embryonic central nervous system (CNS) of *Drosophila* melanogaster [12-14]. In the CNS, numerous neurons project their axons across the midline to the contralateral side, while others remain on the ipsilateral side [15]. This crucial decision is dependent on the midline repulsive ligand Slit and its receptor Roundabout (Robo) [16-18]. Slit, secreted by midline glia, ensures that axons with upregulated Robo levels are repelled from the midline, whereas those with downregulated Robo levels can cross the midline. In addition, several families of other secreted proteins, such as Netrin, are also extensively studied for their roles in axon guidance [19, 20]. Similar signaling mechanisms, like Slit-Robo and Netrin-Fra, also guide the later higher-order branches of dendrites in the CNS [21-23]. This raised an intriguing question: Are these secreted-molecule-based mechanisms the only means by which neuronal processes are directed to their proper destinations within the embryonic CNS of *Drosophila*?

Currently, only a limited number of adhesion molecules critical for juxtracrine signaling have been identified in this context [12]. For instance, the atypical cadherin Flamingo is notably involved in the midline crossing of axons [24], while the Down syndrome cell adhesion molecule (Dscam1) is recognized for its role in promoting axon growth across segment boundaries [25].

Despite these significant advances, the detailed mechanisms through which such adhesion molecules, including Flamingo and Dscam1, regulate dendrite formation in the CNS have been largely unexplored. Our prior study addresses this knowledge gap by elucidating a key function of Dscam1 signaling in facilitating dendritic outgrowth [26]. In our research, we concentrated on anterior corner cell (aCC) motoneurons, examining their lateral axonal extensions and intersections with MP1 partner neurons. We discovered that at the point of intersection, dendritogenesis—the formation of primary dendritic branches—is promoted by a cell-cell adhesion process. Importantly, this adhesion process, identified as an inter-neuronal Dscam1 interaction, involves Dscam1 on one neuron binding to its counterpart Dscam1 on an adjacent neuron, recruiting Pak1 kinase through the Dreadlocks (Dock) adaptor protein on the aCC membrane. This recruitment initiates local cytoskeletal changes, leading to dendritic branch outgrowth. However, the extent to which this mechanism represents a conserved principle among motoneurons, where inter-neuronal Dscam1 interactions dictate dendritic outgrowth sites, remains to be explored. Furthermore, the broader impact of this interaction on other aspects of neuronal morphology in *Drosophila* is not yet fully understood. Intriguingly, evidence suggests that such Dscam1 interactions are potentially involved in various processes, including cell body migration, axon guidance, axonal outgrowth, axonal targeting, and dendrite patterning [27-34].

In the *Drosophila* embryonic CNS, each hemisegment contains 36 motoneurons [35-37]. Pioneering work by Sink et al. [36] and Landgraf et al. [38], using a lipophilic dye-labeling approach, revealed how individual motoneurons project their axons and dendrites in the ventral nerve cord (VNC). These motoneurons can be categorized into two groups: the first category with cell bodies situated between the midline and the neuropiles along the mediolateral plane, and the second half with cell bodies located from outside the neuropiles to the edge of the VNC. The aCC

motoneurons, which we have previously studied, belong to the first category. In our current investigation, we turn our focus to the latter category to further investigate Dscam1-mediated neural morphogenesis. Motoneurons in the second category have an axon turning pattern and elaborate their dendrites specifically at these axonal turning points. One motoneuron within this category, motoneuron 24 (MN24), demonstrates a distinctive pattern of dendritic elaboration. Unlike the aCC motoneuron, whose dendritic arbors are in the middle region of the neuropile, the dendritic projections of MN24 are predominantly observed at the most lateral edge of the neuropile without overlapping aCC processes. This unique positioning makes MN24 an ideal subject for investigating the molecular and cellular mechanisms that underpin axon turning and dendritic arborization in single, identifiable motoneurons within the embryonic CNS. In addition, MN24 offers a valuable opportunity for independent validation of our previous findings on aCC dendrite outgrowth, contributing to a broader understanding of whether we can generalize the Dscam1-mediated dendrite formation across different motoneuron categories.

Here, we have conducted an anatomical characterization of the MN24 subcellular structures and identified its potential partner structure, a *Scp2*-positive neuronal fascicle. These *Scp2*-positive interneurons project axons along the anterior-posterior axis to form the lateral fascicle, which is detectable through anti-FasII antibody staining. Our findings reveal that the knockout of *dscam1* leads to the disappearance of dendrites and disrupts the axonal routing in MN24. Further, our cell-type specific knockdown and subsequent rescue experiments of *dscam1* indicate that the contact between MN24 and *Scp2*-positive neurons, mediated by Dscam1, is essential for both dendrite outgrowth and axonal routing in MN24. Notably, soma migration appears to be a critical factor for axonal routing. These results unveil a novel mechanism in which

the overall morphology of a neuron is modulated in response to adjacent neuronal fascicles, facilitated by the adhesion of the Down syndrome cell adhesion molecule (Dscam1).

2.3 RESULTS

Spatial Regulation of MN24 Dendritogenesis in Late Embryonic CNS

Previous studies have demonstrated that the dendritic processes of the MN24 are distinctly positioned away from those in the aCC motoneuron, exhibiting a notable lateral shift [38, 41]. While these studies have characterized the dendritic morphologies of MN24 qualitatively, there are no current reports that carefully examine the exact positioning and detailed arrangements of its dendritic branches. In our prior study [26], we identified a MN24-specific GAL4 driver, *hedgehog (hh)-GAL4*, during a screening of GAL4 drivers. Notably, this *hh-GAL4* driver initiates GAL4 expression at 11:00 AEL in MN24, as well as in several neighboring motoneurons (MN21, MN22, and MN23). Initially, using this GAL4 driver, we attempted to label neuronal processes by expressing a membrane marker (*UAS-mCD4::tdGFP*). However, due to the low expression level of this GAL4 driver, we were unable to achieve adequate membrane labeling to distinguish fine neuronal structures. Consequently, we decided to employ a retrograde lipophilic-dye labeling technique. This method allowed us to label membranes with a high density of lipophilic dye, enabling the detailed visualization of individual dendritic branches. We then quantified the number and position of dendritic tips, the latter defined as the distance from the midline to the ventral nerve cord edge (**Figure 2.1a-b**). These measurements reveal that on average, wild-type MN24 at 15:00 AEL has 7.6 ± 0.3 (mean ± SEM) primary dendritic branches, which are located 15.8 ± 0.3 mm from the midline (**Figure 2.1a** and **c**). In addition to dendritic characteristics, we measured other anatomical features of MN24. The cell body of MN24 is located outside of the neuropile at 25.6 ±

0.8 mm from the midline (**Figure 2.1a**). The axonal process of MN24 extends 7.9 ± 0.8 mm towards the midline before diverging away from it (**Figure 2.1a**), forming a 'routing' pattern. Following this divergence, the axon exits the CNS and then innervates the target muscle 24 (**Figure 2.1a**). Additionally, we quantified the area encompassed by the axonal routing, finding it to be 36.2 ± 3.6 mm^2 (**Figure 2.2** for details of area measurement). Together, the arrangement of MN24 neuronal processes—precisely, its dendrite formation—is stereotypically positioned, suggesting MN24 dendrites are regulated in a spatial manner.

Potential Guiding Role of the Most Lateral Fascicle Structure to MN24 Dendritogenesis

The emergence of primary dendritic branches of MN24 at specific lateral positions within the CNS prompts the following question: What spatial cue guides MN24 to generate its branches at the precise location? To understand the positioning of MN24 dendrites relative to established positional landmarks, we performed immunostaining on wild-type embryos using an anti-FasII antibody. This antibody reveals a set of axon tracts, each forming distinct longitudinal fascicles within the neuropile [42]. These tracts run along the anterior-posterior axis and parallel to each other in the mediolateral direction (**Figure 2.1b**). Notably, the most lateral fascicle is located 16.2 ± 0.1 mm from the midline, closely mirroring the positioning of MN24 dendrites at 15.8 ± 0.3 mm (**Figure 2.1c**). Due to the incompatibility between immunohistochemistry and lipophilic dye labeling techniques, as detergent washes away the dye, we were unable to simultaneously image their structures. However, our quantitative analysis indicates their proximity, suggesting that the lateral fascicle might play a crucial positional role in MN24 dendritogenesis.

Loss of Dscam1 Disrupts MN24 Dendritic Processes

As previously demonstrated [26], the *dscam1* gene plays a prominent role in the outgrowth of primary dendritic branches in the aCC motoneuron, evidenced by the near elimination of these

branches in the *dscam1* null mutants (*dscam1*$^{-/-}$). Building upon this, we investigated whether *dscam1* similarly regulates dendritogenesis in MN24. We characterized the dendritic outgrowth of MN24 in embryos homozygous for the *dscam1* mutation. In *dscam1*$^{-/-}$, we observed a significant decrease in the number of primary dendritic branches. On average, there were 1.3 ± 0.4 branches in *dscam1*$^{-/-}$ compared to the wild-type, which had 7.6 ± 0.3 (**Figure 2.3a-b**). Interestingly, in the mutant background, we observed a notable 'collapse' in the axonal routing of MN24 (**Figure 2.3a**). On average, the area of the axonal routing in the mutants was significantly reduced, measuring only 4.1 ± 4.4 mm^2, in contrast to the wild-type area, which was 36.2 ± 3.6 mm^2 (**Figure 2.3c**). Further cellular characterization in the *dscam1*$^{-/-}$ mutant revealed that while MN24 extends its axon around the target muscle region in most cases, there were occasional instances where it failed to reach the target muscle 24 (**Figure 2.3d-e**). Despite these minor defects, the overall pattern of axon guidance in MN24 remains intact. These results suggest that the loss of *dscam1* specifically impacts the development of primary dendritic branches and the routing of the axon shaft in MN24 before exiting the VNC.

Since we hypothesize that the most lateral FasII-positive fascicle might be involved in MN24 dendritogenesis, it is crucial to assess its phenotype in the mutant. Following staining of the *dscam1*$^{-/-}$ mutant with the anti-FasII antibody, we observed thinning in the lateral fascicle and, on some occasions, a 'wavy' pattern. However, for the most part, the mutant lateral fascicle appeared relatively normal, where 87.1% of mutant fascicles from the 66 observed hemisegments contained no breakage similar to 89.0% of those from wild-type containing no breakage (**Figure 2.4a-b**). Based on these observations, we anticipate that the close proximity between this fascicle and MN24 is largely maintained.

In conclusion, our findings indicate that Dscam1 may act as a crucial positional cue for dendritic outgrowth and axonal routing in MN24. This aligns with our previous observations showing a high concentration of Dscam1 proteins at the neuropile, the site of MN24 dendritogenesis and axonal routing [26]. However, the exact mechanism—whether these defects in MN24 are a direct result of *dscam1* loss specifically in MN24 or a secondary effect arising from a global loss of *dscam1*—remains to be elucidated.

Dual Roles of *dscam1* in Dendritic Outgrowth and Axonal Routing in MN24

To further elucidate the mechanism, we conducted cell-type specific manipulation of *dscam1* using a short hairpin RNA (shRNA) targeting *dscam1* under *UAS* control for gene knockdown (*UAS-dscam1 RNAi*). The efficacy of this *UAS-dscam1 RNAi* line, previously validated [26], was apparent when expressed under the control of the pan-neuronal GAL4 driver, *elav-GAL4*, leading to the elimination of Dscam1 proteins from the embryonic CNS. Crossing this RNAi line with *hh-GAL4*, we selectively knocked down *dscam1* in MN24. This targeted approach resulted in a significant reduction in dendritic branches—on average, MN24-specific RNAi knockdown exhibited only 1.7 ± 0.4 primary dendritic branches, compared to control embryos, which had 6.8 ± 0.5 (**Figure 2.5a-b**). Notably, reintroducing a single isoform of *dscam1* (*UAS-dscam1*$^{exon\ 17.2}$) into MN24 in the *dscam1* mutant background did not restore the normal dendritic count (2.3 ± 0.5 for rescue and 1.1 ± 0.7 for mutant control) (**Figure 2.5c-d**).

Regarding axonal routing, the MN24-specific RNAi knockdown of *dscam1* partially replicated the knockout phenotype. Knocking down *dscam1* led to alterations in the axonal routing of MN24, with the average routing area measuring 14.0 ± 4.8 mm^2, compared to the control's 42.0 ± 5.5 mm^2 (**Figure 2.5a** and **e**). However, this phenotype was less severe than in the knockout control, which had an average loop area of 7.7 ± 5.7 mm^2 (see also **Figure 2.5f**, the second bar).

Reintroducing the *dscam1* gene into MN24 in the *dscam1*$^{-/-}$ background did not significantly rescue the axonal routing structure observed (8.5 ± 4.2 mm^2 for rescue) (**Figure 2.5b** and **f**).

From these findings, we draw two conclusions: (1) the RNAi knockdown results suggest that *dscam1* serves a cell-autonomous function in the dendritogenesis and axonal routing of MN24, and (2) the rescue results indicate that *dscam1* alone is not sufficient for the formation of both cellular structures in MN24. Furthermore, these results imply the possibility that *dscam1*, when expressed in other cells, contributes to MN24 morphogenesis, indicating a non-cell-autonomous function of dscam1 in these processes.

***Scp2*-GAL4: Enabling Selective Expression of Transgenes in Lateral Fascicles**

To elucidate the non-cell-autonomous functions of *dscam1*, we considered that the most lateral FasII-positive fascicle might provide positional cues to MN24, potentially mediated by Dscam1. To test this hypothesis, we must manipulate the *dscam1* gene in the lateral fascicle. However, due to the absence of a reported GAL4 line specifically labeling the most lateral fascicle, we embarked on a screening to identify a new GAL4 driver. By crossing approximately 20 GAL4 lines with *UAS-mCD4-tdGFP*, we identified a promising candidate, *Scp2-GAL4*. This GAL4 line labels a subset of interneurons that contribute to the formation of the most lateral fascicle. The expression pattern observed in *Scp2-GAL4* highlights neuronal processes from interneurons, segregated into either the medial or lateral fractions of the FasII-positive fascicles (**Figure 2.6**). Additionally, this GAL4 line targeted aCC and RP2 motoneurons in 40.6% and 34.3% of the observed hemisegments (n=32), respectively. MN3 and MN19 were also labeled, though less frequently, at 6.3% for each of the hemisegments observed. Importantly, *Scp2-GAL4* does not label MN24 or any related motoneurons within the same SNa nerve tract. In conclusion, we identified *Scp2-GAL4* as a GAL4

line that facilitates the expression of *UAS* transgenes in two of the FasII-positive fascicles, notably including the most lateral fascicle.

Dscam1 in the Lateral Fascicle is Necessary for MN24 Dendritogenesis and Axonal Routing

Using the *Scp2-GAL4* driver, we simultaneously implemented *UAS-dscam1 RNAi* for specific gene knockdown and *UAS-mCD4-tdGFP* for targeted cell labeling. This approach led to a significant reduction in dendritic branches—on average, MN24 exhibited 2.0 ± 0.4 primary dendritic branches, compared to the control, which had 8.3 ± 0.6 (**Figure 2.7a-b**). These results strongly support the concept of a non-cell-autonomous function for *dscam1*. Interestingly, subsequent attempts to rescue the dendritic phenotype by reintroducing *dscam1* into *Scp2*-positive neurons were unsuccessful in reversing the mutant phenotype in MN24 (1.4 ± 0.5 for rescue and 2.1 ± 0.5 for mutant control) (**Figure 2.7c-d**). This suggests that the expression of the *dscam1* gene only in *Scp2*-positive neurons is not sufficient for MN24 dendritogenesis.

Similarly, RNAi knockdown of *dscam1* using *Scp2-GAL4* led to a 'collapse' in the axonal routing of MN24. The average axon routing area was measured at 12.6 ± 4.6 mm^2, significantly reduced compared to the control, which was measured at 35.6 ± 5.8 mm^2 (**Figure 2.7a and e**). Additionally, when we resupplied the *dscam1* gene only to *Scp2*-positive neurons in *dscam1*$^{-/-}$, there was no observed rescue of the axonal routing structure (9.4 ± 4.1 mm^2 for rescue and 2.4 ± 4.0 mm^2 for mutant control) (**Figure 2.7b and f**). Importantly, upon imaging in the rescue experiments, we found that the cell bodies of MN24 were variably positioned relative to the most lateral fascicles; mutant MN24 had a cell body position that seemed more medially shifted compared to control MN24 (for example, see **Figure 2.7a and Figure 2.8a**). Inspired by this observation, we measured the positions of both the cell bodies and the fascicle relative to the midline. We discovered that while the position of the most lateral fascicle remained unchanged

(15.3 ± 0.4 mm for mutant and 14.3 ± 0.5 mm for control), the cell bodies of MN24 were differently positioned, often closer to the lateral fascicle (19.8 ± 0.9 mm for mutant and 26.7 ± 1.0 mm for control) (**Figure 2.8b-c**). This led us to speculate that the reduced area of the axon loop might be a secondary defect—due to the proximity of MN24 cell bodies to the most lateral fascicle, there may be insufficient space for the axonal routing to form properly in these genetic backgrounds (see the Discussion).

Dscam1 Mediates Interaction Between MN24 and the Lateral Fascicle for Proper Dendritogenesis and Axonal Routing of MN24

Our experiments indicate that both cell-autonomous and non-cell-autonomous functions of *dscam1* are essential for dendritogenesis and axonal routing in MN24 and suggest that Dscam1 on either side of the neuronal membranes function to guide MN24 neurite processes. If Dscam1 serves as a positional cue, then we reasoned that providing Dscam1 to both MN24 and *Scp2*-positive neurons would restore the MN24 mutant phenotype. To directly test this hypothesis, we reintroduced *UAS-dscam1* into *dscam1*$^{-/-}$ mutants using two GAL4 drivers, *Scp2*- and *hh-GAL4*, targeting both MN24 and *Scp2*-positive fascicle. In alignment with our hypothesis, this dual reintroduction of *dscam1* led to a complete recovery of the MN24 dendrite count (7.4 ± 0.5 for rescue and 8.4 ± 0.6 for control) and restoration of the axonal routing structure (41.1 ± 6.2 mm^2 for rescue and 38.6 ± 6.7 mm^2 for control) (**Figure 2.9a-c**). Notably, the axonal structure recovered, with the cell bodies repositioning to locations similar to those in the controls (27.1 ± 0.9 mm for rescue and 28.6 ± 1.0 mm for control) (**Figure 2.10**). These findings suggest that Dscam1's function in both MN24 and *Scp2*-positive neurons is crucial for dendritogenesis and axonal routing in MN24 and are consistent within the model that Dscam1 acts as a positional cue to guide MN24 development (**Figure 2.11a**).

2.4 DISCUSSION

Dscam1 as a Positional Cue Defines the MN24 Dendritogenesis Site

Expanding on our previous findings about dendritogenesis in the aCC motoneuron [26], our current study explores the function of *dscam1* during MN24 dendritogenesis. Our research presents several lines of evidence suggesting that the interaction between MN24 and *Scp2*-positive neurons is critical for the outgrowth of primary dendritic branches in MN24. Firstly, we demonstrate that MN24 and the *Scp2*-positive fascicle are in proximity. Secondly, upon knocking down *dscam1* in either MN24 or *Scp2*-positive fascicle, we observed a reduction in the number of primary dendritic branches, mirroring the phenotype seen in *dscam1*$^{-/-}$ mutants. This suggests that *dscam1* in both MN24 and *Scp2*-positive fascicle is necessary for MN24 dendritogenesis. Thirdly, our rescue experiments in *dscam1*$^{-/-}$ mutants, involving the reintroduction of *dscam1* into either MN24 or *Scp2*-positive fascicle, were unsuccessful. This indicates that *dscam1* function in either neuron type alone is insufficient. However, when *dscam1* was reintroduced into both MN24 and *Scp2*-positive fascicle in *dscam1*$^{-/-}$ mutants, we could fully rescue the dendritic phenotype. Finally, the observation that MN24 axons still contact the *Scp2*-positive fascicle in *dscam1*$^{-/-}$ mutants rules out the possibility that the reduced number of dendrites is due to a mislocation of these neural processes. Consequently, we propose that Dscam1 provides a positional cue for MN24 through cell-cell contact, defining the site of dendritic outgrowth (**Figure 2.11a**). This mechanism echoes how vertebrate DSCAM guides retinal ganglion cell (RGC) dendrites and bipolar cell axons for synapse formation in the chick retina [43], suggesting a potentially conserved principle in dendritic outgrowth mediated by inter-neuronal Dscam1 interactions.

Our study specifically targets the early developmental stage of the MN24, around 15:00 after egg laying (AEL), a pivotal time when primary dendritic branches start to emerge. The critical role of these initial branches in forming the foundation for higher-order branches and synaptic formations has yet to be fully established, but emerging data offer promising insights. Recent advancements in comprehensive connectome efforts have facilitated the reconstruction of the entire CNS in the first instar larva, and this valuable data is accessible in a publicly available database [44, 45]. Using this resource, we have examined an electron microscopy (EM) reconstructed model of MN24 [44, 45]. This model reveals that the higher-order branches are situated in the regions of the axonal turning points, corresponding to the area where MN24's primary dendrites initiate (**Figure 2.11b**). Notably, these branches exhibit numerous synapses throughout their structure. This observation suggests a developmental progression from primary dendritic branches to the establishment of functional synapses in MN24.

The Roles of Dscam1 in Axonal Routing and Soma Migration of MN24

In addition to the observed loss-of-dendrite phenotype, our study has revealed axonal routing defects in MN24 in *dscam1*$^{-/-}$ mutants. Normally, MN24 axons project ventrally, reaching the most lateral FasII-positive fascicle, and then undergo a crucial lateral turn as part of their axonal routing process. However, in *dscam1*$^{-/-}$ mutants, this axonal routing is notably compromised. One potential explanation for this diminished axonal routing in *dscam1*$^{-/-}$ mutants could be related to a migration defect of the soma in MN24. In *dscam1*$^{-/-}$ mutants, the soma position is observed to be closer to the lateral fascicle (**Figure 2.7c** and **Figure 2.8a** and **c**). Interestingly, reintroducing *dscam1* into both MN24 and *Scp2*-positive neurons corrects the soma's position, subsequently leading to the restoration of the normal axonal loop structure (**Figure 2.9c and 2.10**).

The role of *dscam1* in soma migration during brain development in *Drosophila* is an emerging research interest. A critical study by Liu et al. focusing on larval medulla neurons has provided significant insights into this process [33]. They revealed that within the fly visual system, the cell bodies of sister neurons from the same lineage exhibit mutual repulsion. This event contributes to the formation of columnar structures. This repulsive interaction is mediated by inter-neuronal interaction between Dscam1. Inspired by these findings, we propose a similar mechanism in the MN24 system. We propose a model where Dscam1 orchestrates a repulsive interaction between the soma of MN24 and the *Scp2*-positive fascicle (**Figure 2.11a**). Given the lateral expansion of the ventral nerve cord (VNC) during development, the soma of the MN24 is initially positioned close to the lateral fascicle and is likely to migrate laterally as development progresses. This migration would be started off by inter-neuronal Dscam1 interactions.

Single Isoform of Dscam1 for Rescue in Morphological Defects in MN24

An impressive diversity of 19,008 isoforms, each with different extracellular domains, can arise from the *dscam1* gene through alternative splicing of three variable exon clusters [27, 46]. These extracellular domains can bind in a homophilic and isoform-specific manner [30, 47]. Intriguingly, each neuron in the fly is found to express a distinct and limited set of Dscam1 isoforms [48, 49]. Consequently, the isoform-specific binding characteristics of Dscam1 facilitate homophilic repulsion exclusively among identical (or 'self') cells, raising questions about Dscam1 interactions between different neuron types like MN24 and *Scp2*-positive neurons.

In our experiments, we introduced a single isoform of *dscam1* simultaneously into different neuron types, which successfully rescued the phenotypes associated with dendritogenesis and axonal routing in MN24 (**Figure 2.9a-c**). These findings suggest that just one isoform of *dscam1* is sufficient for these developmental processes. This leads us to question

the nature of Dscam1 trans- and homophilic interactions between different neuronal types. Several hypotheses arise: one possibility is that MN24 and *Scp2*-positive neurons express the same set of isoforms, potentially due to originating from the same neuronal progenitor cells, thus sharing isoform profiles. Alternatively, the trans-interaction of Dscam1 might be mediated by other molecules, forming a protein complex. For instance, in *C. elegans*, the dendritic branching of PVD neurons involves the interaction of SAX7/NMR-1 transmembrane proteins with DMA-1, mediated by the secreted LECT-2 adapter [50, 51]. A similar mechanism might be at play in *Drosophila*, with secreted molecules (such as Slit [25, 52], Netrin [53, 54], or other ligands yet to be determined) bridging opposing Dscam1 membranes through their non-variable regions.

Cross-Species Insights into DSCAM-Mediated Motor Circuit Formation

Unraveling the specific mechanisms of Dscam1 interactions among diverse neuronal types will significantly broaden our understanding of how our model generalizes to motoneurons in *Drosophila*. Additionally, the structural and functional similarities between the *Drosophila* embryonic CNS and the mammalian spinal cord highlight the potential for cross-species studies on DSCAM. The spinal cord, within the neural tube, serves as a model for axon guidance research, showcasing shared molecular mechanisms between mammals and *Drosophila* [12, 14, 54]. For instance, the interaction between Netrin1 and DCC, which directs commissural axons towards the midline in mice, reflects analogous processes in the *Drosophila* embryonic CNS [20, 55-57]. Recent findings from Klar's group have significantly emphasized the role of homophilic DSCAM interactions in the fasciculation of chick commissural axons [58]. Their *in-situ* hybridization data reveal that *DSCAM* is expressed in subsets of motoneurons. Considering the close proximity of motoneuron cell bodies and dendrites to these commissural axons [59, 60], it

is plausible that axonal fascicles could influence motoneuron morphogenesis through DSCAM-mediated interactions. Future research along these lines is essential.

2.5 FIGURES

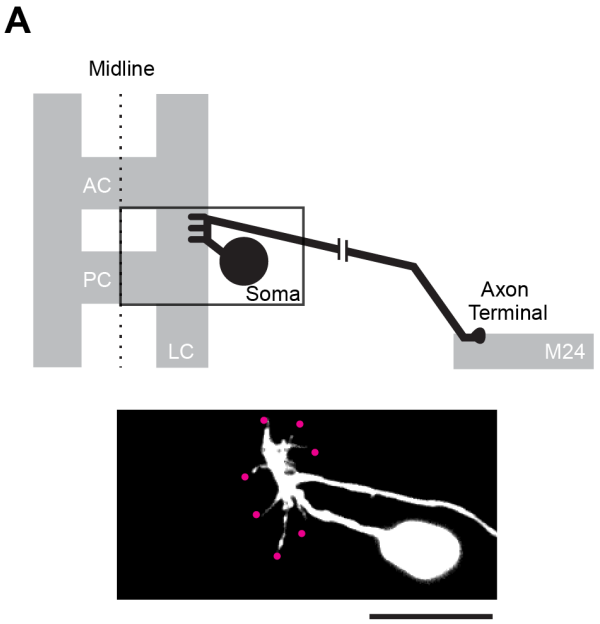
A
Midline
AC
PC
LC
Soma
Axon
Terminal
M24
B
Lateral
Fascicle
0 6 12 18 24 30
Distance from midline (μm)
C
The most lateral fascicle
Count
40
30
20
10
0
0 6 12 18 24 30
MN24 dendrites
Count
15
12
9
6
3
0
0 6 12 18 24 30
Distance from midline (μm)

Figure 2.1 | Neuronal Fascicle Spatially Aligns with the Position of MN24 Dendrite Formation (**a**) Top panel shows a schematic of MN24 (black) within the ventral nerve cord of an embryo. The axon stereotypically projects out of the soma, anteriorly along the edge of the longitudinal connective (LC), and away from the midline to target muscle 24 (M24). The bottom panel shows a representative fluorescence image of a lipophilic-dye-labeled MN24. At 15:00h AEL, MN24 form their dendritic processes (magenta dots) at stereotyped positions on the axon routing. For all subsequent images, anterior is to the top, and medial is to the left. AC: Anterior commissure. PC: Posterior commissure. Scale bar, 10 mm. (**b**) Representative fluorescence images of FasII-positive longitudinal fascicles within the ventral nerve cord. The stereotyped most lateral FasII-positive fascicle structure (arrowhead) provides a frame of reference to characterize the mediolateral position of MN24 dendrites. Gray dashed line depicts the midline. (**c**) Distribution plots of the mediolateral positions of MN24 dendritic branches (white) (n = 22 neurons) and FasII-positive lateral fascicle (dark gray) (n = 77 hemisegments), where 0 mm indicates the distance from the CNS midline.

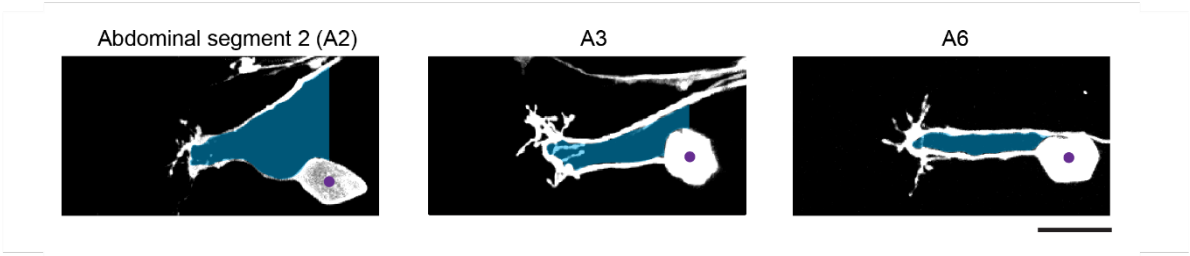

Figure 2.2 | Segment-specific MN24 Morphologies in the Wild-Type Background

Representative images depicting the morphology of wild-type MN24 in different abdominal segments are shown. These images show the characteristic dendrites and axon routing, observed in Figure 1A. Notably, the angle of the axon segment projecting towards the muscle varies in a segment-specific manner. Axon routing area (shaded blue) is measured as the area within the loop. For "open" axon routing areas, (left and middle panels), we define the center of the cell body (purple dot) and use the perpendicular line to the soma center as the border for measurement of the axon routing area. Scale bar, 10 μm.

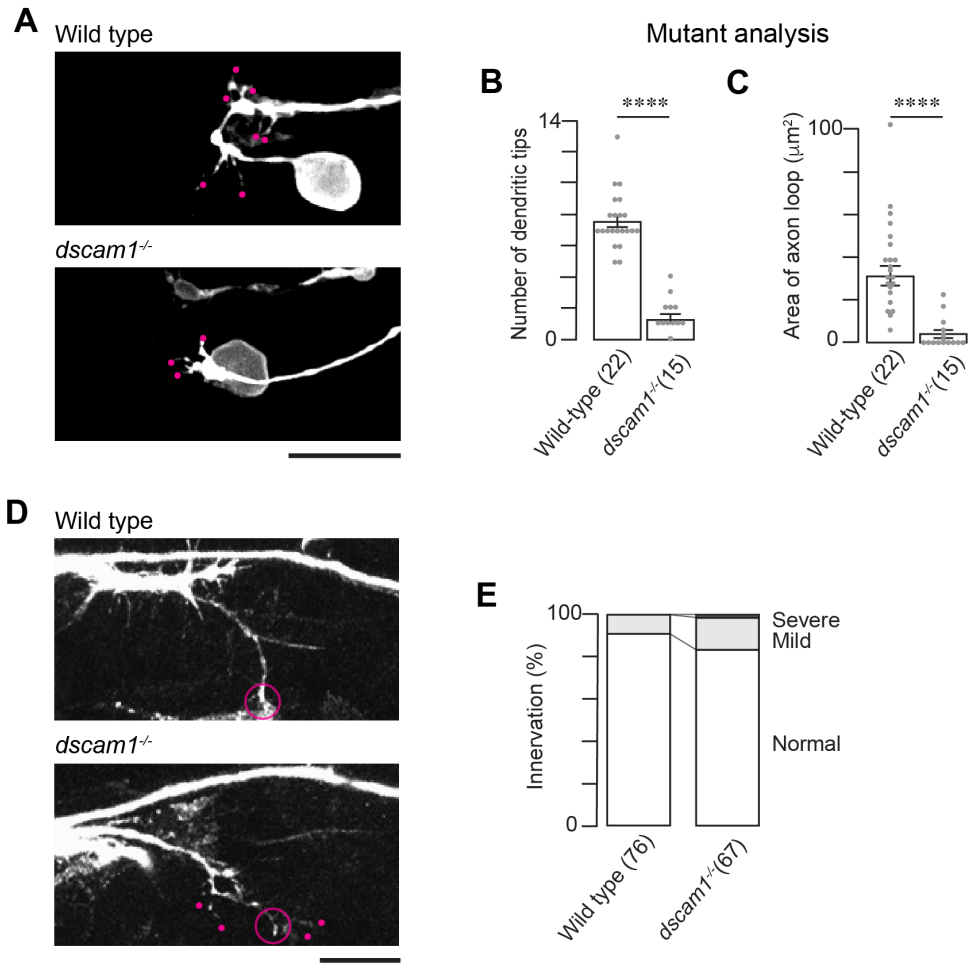

Figure 2.3 | *dscam1* is Required for MN24 Neurite Development (**a**) Representative fluorescence images of MN24 within wild-type (top panel) and *dscam1*$^{-/-}$ mutant (bottom panel) backgrounds. (**b** and **c**) Comparison of mean primary dendritic branch numbers (**b**) and axon routing areas (**c**) within wild-type and *dscam1*$^{-/-}$ mutant backgrounds; using Mann–Whitney U test. For all graphs, the sample size of neurons is denoted by the number in the parentheses of each genotype unless otherwise specified. For all subsequent statistical analyses, symbols indicate the following: ****, $p < 0.0001$; ***, $p < 0.001$; **, $p < 0.01$; *, $p < 0.05$; ns – not significant. (**d**) Immunofluorescence staining of FasII at 15:00h AEL shows the visual comparison between axon terminals in wild-type (top panel) and *dscam1*$^{-/-}$ mutant (bottom panel)

backgrounds. Representative image displaying FasII staining in the wild-type and mutant backgrounds exhibits innervation by the SNa nerve branch (open circle). However, in the *dscam1*$^{-/-}$ mutant background, the SNa sub-branches have some mild targeting defects (white dots). (**e**) Quantification of SNa innervation defects within wild-type (n = 76 hemisegments) and *dscam1*$^{-/-}$ mutant (n = 67 hemisegments) backgrounds. Data is represented as a percentage – number of hemisegments with innervation defects over the total number of hemisegments observed. SNa innervation defects were characterized as mild (light gray) or severe (dark gray) when the SNa sub-branch had targeting defects or the SNa branch did not exit the nerve cord, respectively. Scale bars, 10 μm in (**a** and **d**).

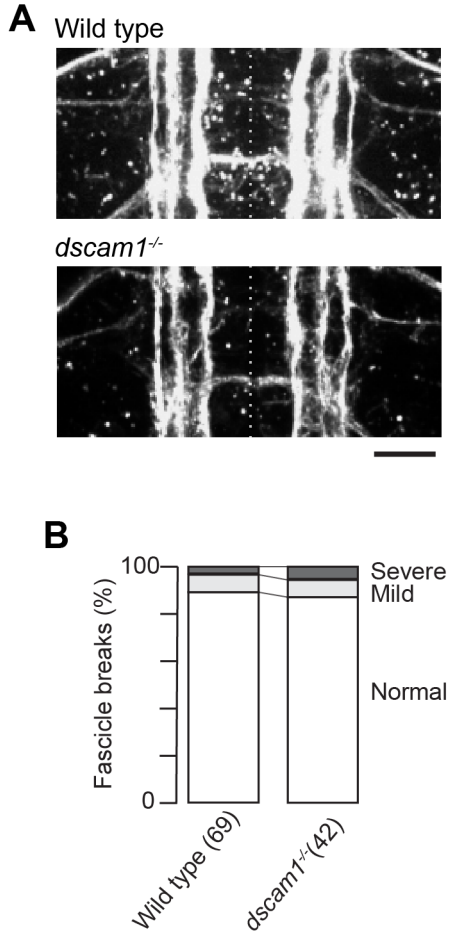

Figure 2.4 | Longitudinal Fascicles in Wild-Type and *dscam1*$^{-/-}$ Mutant Backgrounds (**a**) Representative fluorescence images of FasII-positive axon tracts within wild-type (top panel) and *dscam1*$^{-/-}$ mutant (bottom panel) backgrounds. Scale bar, 10 μm. (**b**) Quantification of lateral fascicle defects within wild-type (n = 77 hemisegments) and *dscam1*$^{-/-}$ mutant (n = 66 hemisegments) backgrounds. Data is represented as a percentage – length of lateral fascicle defects over total lateral fascicle length. Lateral fascicle defects were characterized as mild or severe when the lateral fascicle was thinning or contained a break, respectively.

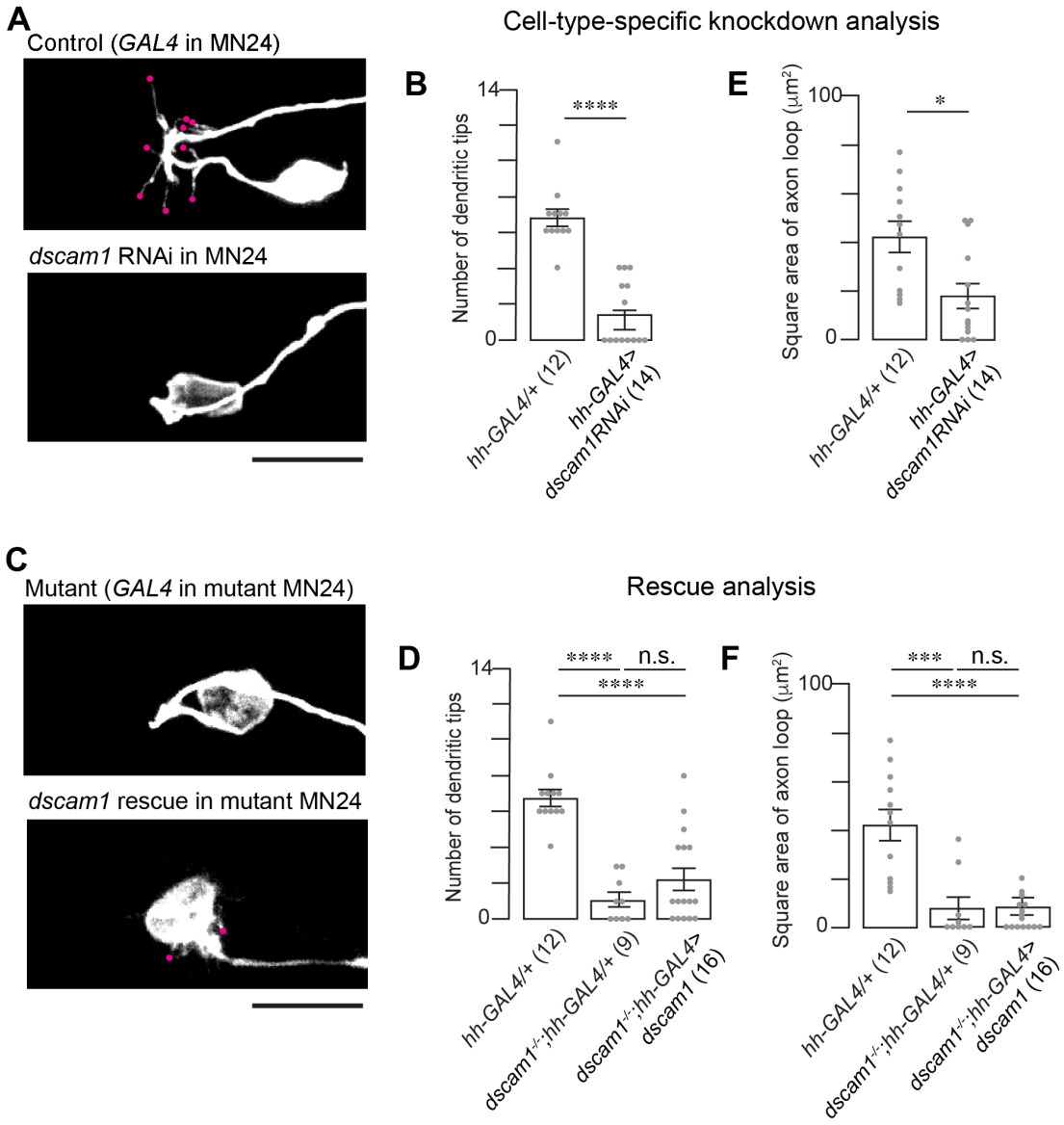

Figure 2.5 | Dscam1 Plays a Cell-Autonomous Role for MN24 Neurite Development (**a**) Representative fluorescence images of MN24 in wild-type background expressing *hh*-GAL4 driver (top panel) and *dscam1* RNAi expressed under the control of the *hh*-GAL4 driver (bottom panel). (**b** and **e**) Comparison of mean primary dendritic branch numbers (**b**) and axon routing areas (**e**) of MN24 in wild-type background expressing *hh*-GAL4 driver and *dscam1* RNAi expressed under the control of the *hh*-GAL4 driver; using Mann–Whitney U test. (**c**) Representative fluorescence images of MN24 in *dscam1*$^{-/-}$ mutant background expressing *hh*-

GAL4 driver (top panel), and *dscam1*$^{-/-}$ mutant background resupplied *dscam1* expressed under the control of the *hh*-GAL4 driver (bottom panel). (**d** and **f**) Comparison of mean primary dendritic branch numbers (**d**) and axon routing areas (**f**) of MN24 in wild-type background expressing *hh*-GAL4 driver, *dscam1*$^{-/-}$ mutant background expressing *hh*-GAL4 driver, and *dscam1*$^{-/-}$ mutant background resupplied *dscam1* expressed under the control of the *hh*-GAL4 driver; using Kruskal–Wallis test followed by Dunn's multiple comparisons test. Scale bars, 10 μm in (**a** and **c**).

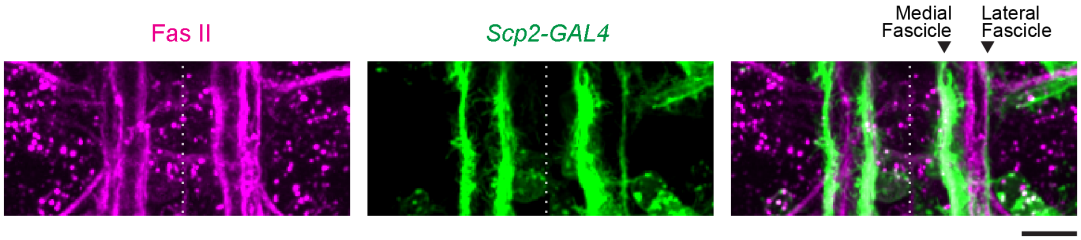

Figure 2.6 | *Scp2*-GAL4 Driver Allows Labeling of Lateral Fascicle Representative images of neuronal fascicles labeled by membrane-bound GFP under the control of *Scp2*-GAL4 driver (green) or immunostained with anti-FasII antibody (magenta). *Scp2*-positive fascicles include the medial and lateral fascicles (arrowheads) and exclude the intermediate fascicle. Scale bar, 10 μm.

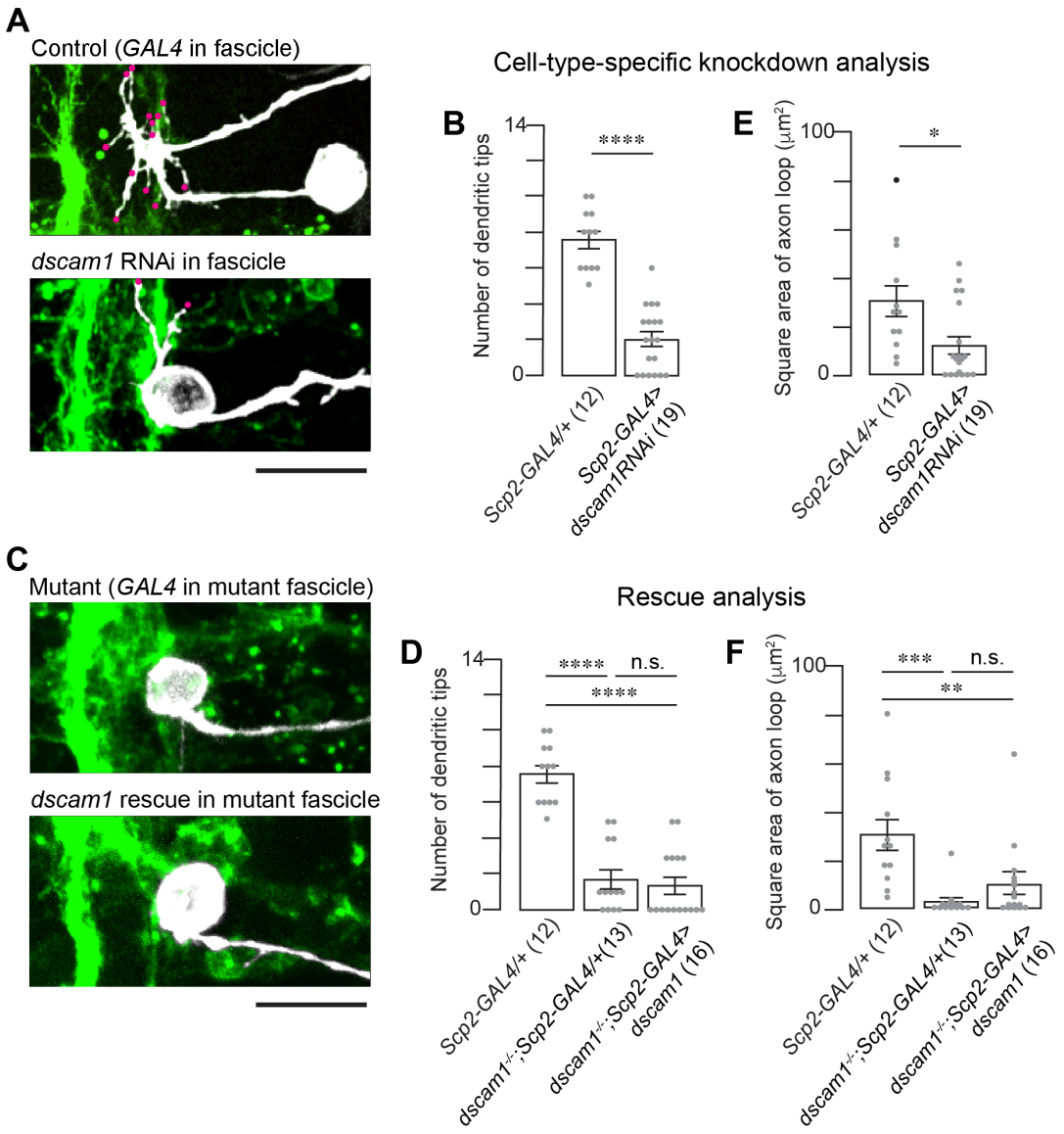

Figure 2.7 | *Scp2*-Positive Lateral Fascicle Provides Non-Cell-Autonomous Dscam1 for MN24 Neurite Development (**a**) Representative fluorescence images of MN24 in wild-type background expressing *Scp2*-GAL4 driver (top panel) and *dscam1* RNAi expressed under the control of the *Scp2*-GAL4 driver (bottom panel). (**b** and **e**) Comparison of mean primary dendritic branch numbers (**b**) and axon routing areas (**e**) of MN24 in wild-type background expressing *Scp2*-GAL4 driver and *dscam1* RNAi expressed under the control of the *Scp2*-GAL4 driver; using Mann–Whitney U test. (**c**) Representative fluorescence images of MN24 in

dscam1$^{-/-}$ mutant background expressing *Scp2*-GAL4 driver (top panel), and *dscam1*$^{-/-}$ mutant background resupplied *dscam1* expressed under the control of the *Scp2*-GAL4 driver (bottom panel). (**d** and **f**) Comparison of mean primary dendritic branch numbers (**d**) and axon routing areas (**f**) of MN24 in wild-type background expressing *Scp2*-GAL4 driver, *dscam1*$^{-/-}$ mutant background expressing *Scp2*-GAL4 driver, and *dscam1*$^{-/-}$ mutant background resupplied *dscam1* expressed under the control of the *Scp2*-GAL4 driver; using Kruskal–Wallis test followed by Dunn's multiple comparisons test. Scale bars, 10 μm in (**a** and **c**).

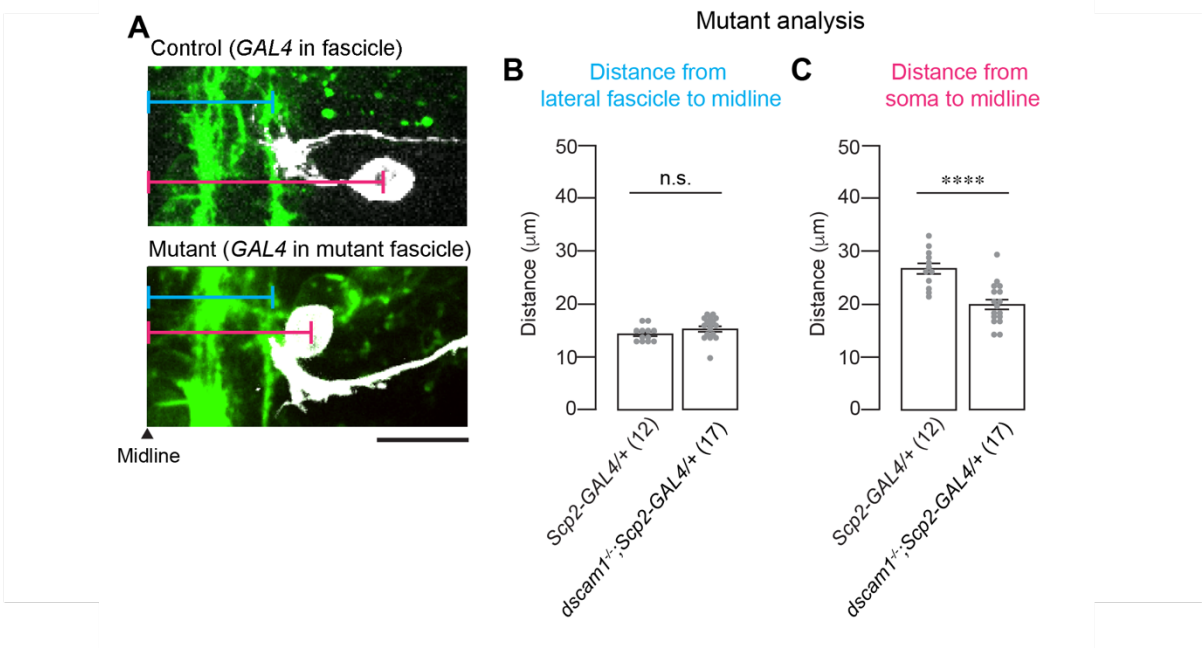

Figure 2.8 | MN24 Soma Position is Medially Shifted in the *dscam1*$^{-/-}$ Mutant Background

(**a**) Representative images of MN24 at 15:00h AEL in wild-type background expressing *Scp2*-GAL4 driver (green) (top panel) and *dscam1*$^{-/-}$ mutant background expressing *Scp2*-GAL4 driver (bottom panel). Blue and pink bars indicate the distance (mm) from the lateral fascicle and soma, respectively, to the midline. Scale bar, 10 μm. (**b**) Quantification of lateral fascicle position in wild-type background expressing *Scp2*-GAL4 driver and *dscam1*$^{-/-}$ mutant background expressing *Scp2*-GAL4 driver; using Welch's *t* test. The *Scp2*-positive lateral fascicle does not have a mediolateral shift in the *dscam1*$^{-/-}$ mutant background. (**c**) Quantification of MN24 soma position in wild-type background expressing *Scp2*-GAL4 driver and *dscam1*$^{-/-}$ mutant background expressing *Scp2*-GAL4 driver; using Welch's *t* test. MN24 soma in the *dscam1*$^{-/-}$ mutant background expressing *Scp2*-GAL4 driver has a more medial shift compared to that of the wild-type background.

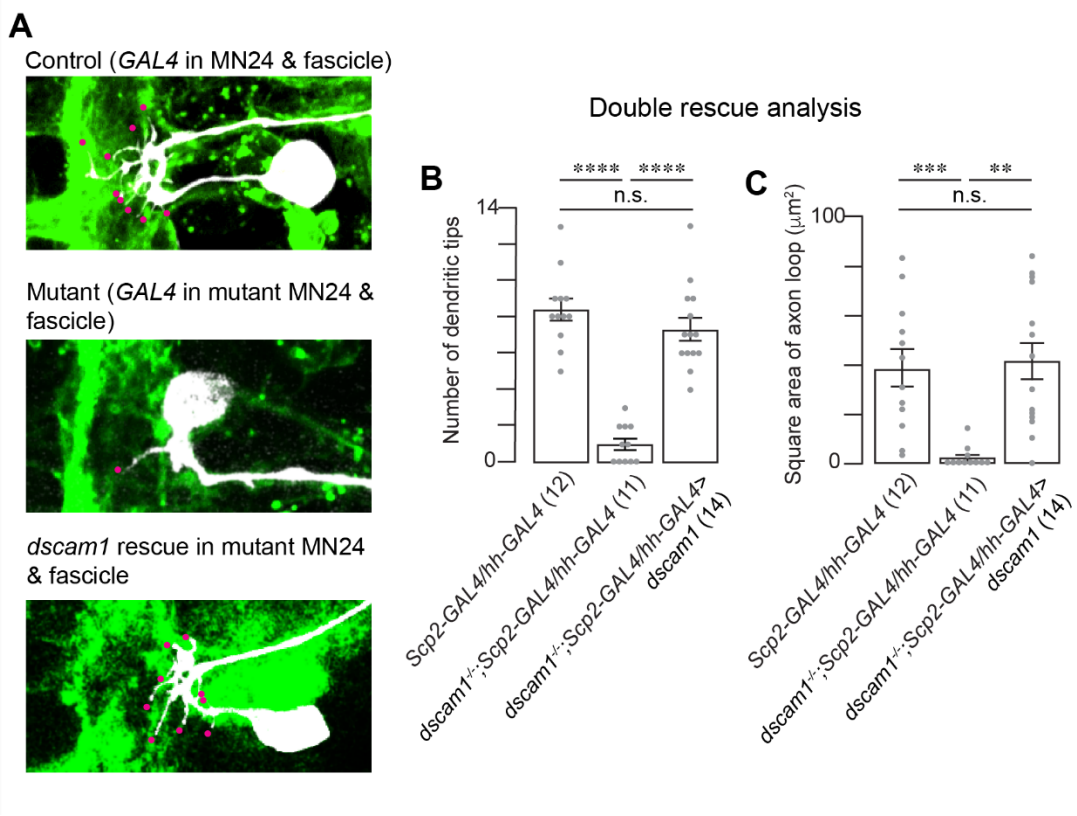

Figure 2.9 | Dscam1 in Both *Scp2*-Positive Lateral Fascicle and MN24 is Sufficient to Restore MN24 Dendritogenesis and Axon Routing (**a**) Representative fluorescence images of MN24 within wild-type background (top panel), *dscam1*$^{-/-}$ mutant background with combined *Scp2*- and *MN24*-specific expression of membrane-bound GFP (middle panel), and *dscam1*$^{-/-}$ mutant background with combined *Scp2*- and *MN24*-specific resupply of *dscam1* (bottom panel). Scale bar, 10 μm. (**b** and **c**) Comparison of mean primary dendritic branch numbers (**b**) and axon routing area (**c**) among MN24 in wild-type background, *dscam1*$^{-/-}$ mutant background with *Scp2*- and *MN24*-specific expression of GFP membrane-bound, and *dscam1*$^{-/-}$ mutant background with combined *Scp2*- and *MN24*-specific resupply of *dscam1*; using Kruskal–Wallis test followed by Dunn's multiple comparisons test.

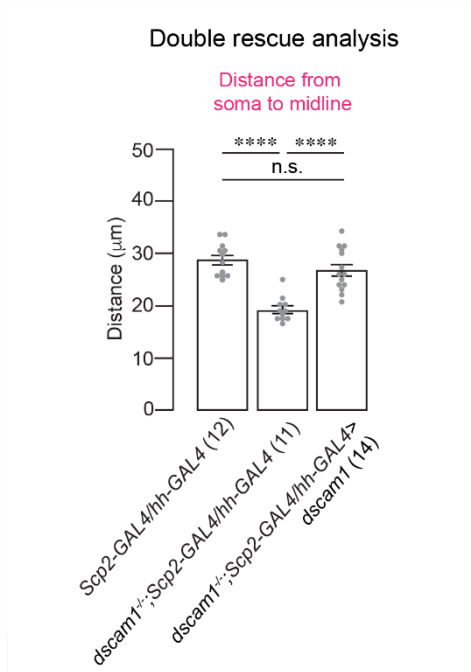

Figure 2.10 | Resupplying *dscam1* in *Scp2*-Positive Lateral Fascicle and MN24 Restores Mutant MN24 Soma Position Quantification of MN24 soma positions in wild-type background with *Scp2*- and *hh*-specific expression of membrane-bound GFP, *dscam1*$^{-/-}$ mutant background with *Scp2*- and *hh*-specific expression of membrane-bound GFP, and *dscam1*$^{-/-}$ mutant background with combined *Scp2*- and *hh*-specific resupply of *dscam1*; using Kruskal–Wallis test followed by Dunn's multiple comparisons test.

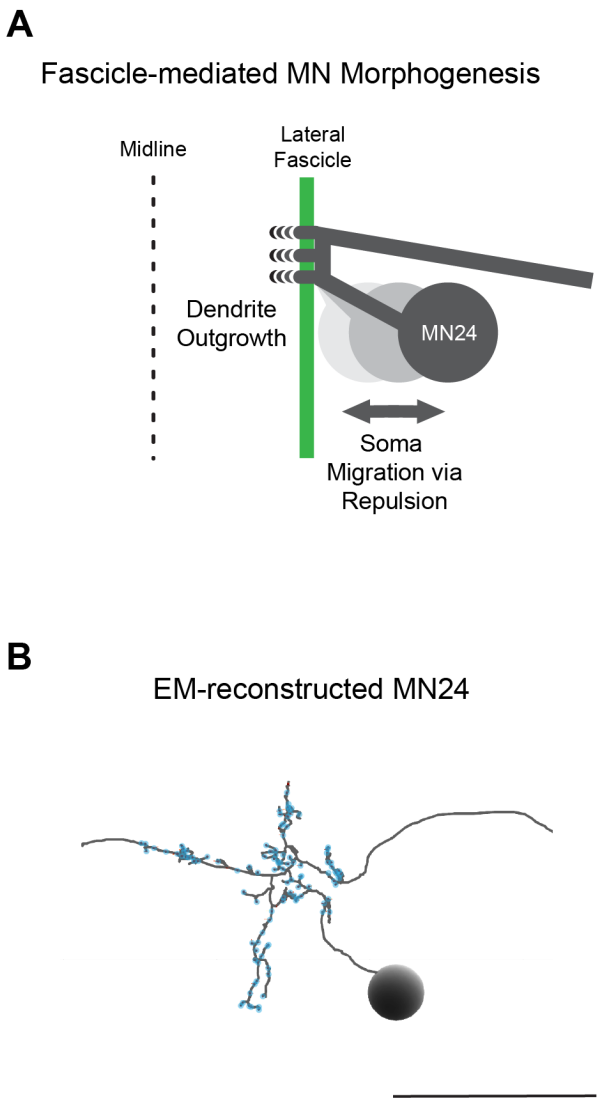

Figure 2.11 | Proposed Model for Fascicle-Mediated MN24 Morphogenesis (**a**) Schematic illustrating the proposed model of how the lateral fascicle structure mediates MN24 dendrite outgrowth and soma migration. (**b**) Electron microscopy (EM) reconstruction from Virtual Fly Brain of a single MN23/24 in 1st instar larva. Prominent morphological structures such as dendritic outgrowth and axon routing are retained in larval MN24. The backbone is indicated by gray. Blue dots indicate synaptic sites. Scale bar, 20 µm.

2.6 TABLES

Table 2.1 | Genotypes of flies shown in this study, related to Figure 2.1-2.9

Figure	Genotype
Figure 1A, B	*w;+/+*
Figure 2	*w;+/+*
Figure 3A	*w;+/+*
	w;*dscam1*^{21}/*dscam1*^{21} (***dscam1-/-***)
Figure 3D	*w;+/+*
	w;*dscam1*^{21}/*dscam1*^{21} (***dscam1-/-***)
Figure 4A	*w;+/+*
	w;*dscam1*^{21}/*dscam1*^{21} (***dscam1-/-***)
Figure 5A	*w;;hh-GAL4/UAS-mCD4::tdGFP* (**positive control**)
	w;;hh-GAL4/UAS-Dscam1 RNAi (***hh-GAL4 UAS-dscam1 RNAi***)
Figure 5C	w;*dscam1*^{21}/*dscam1*^{21};*hh-GAL4/UAS-mCD4::tdGFP* (**negative control**)
	w;*dscam1*^{21}/*dscam1*^{21}; *UAS-mCD4::tdGFP/hh-GAL4, UAS-dscam1*$^{17.2}$*::GFP* (***hh-GAL4 UAS-dscam1***)
Figure 6	*w;;scp2-GAL4/UAS-mCD4::tdGFP*
Figure 7A	*w;;scp2-GAL4/UAS-mCD4::tdGFP* (**positive control**)
	w;;scp2-GAL4/UAS-Dscam1 RNAi (***scp2-GAL4 UAS -dscam1 RNAi***)
Figure 7C	w;*dscam1*^{21}/*dscam1*^{21};*scp2-GAL4/UAS-mCD4::tdGFP* (**negative control**)
	w;*dscam1*^{21}/*dscam1*^{21}; *UAS-dscam1*$^{17.2}$*::GFP/scp2-GAL4, UAS-CD4::tdGFP* (***scp2-GAL4 UAS-dscam1***)
Figure 8A	*w;;scp2-GAL4/UAS-mCD4::tdGFP*
	w;*dscam1*^{21}/*dscam1*^{21};*scp2-GAL4/UAS-mCD4::tdGFP*
Figure 9A	*w;;scp2-GAL4, UAS-CD4::tdGFP/hh-GAL4* (**positive control**)(top)
	w;*dscam1*^{21}/*dscam1*^{21}; *scp2-GAL4, UAS-mCD4::tdGFP/hh-GAL4* (**negative control**) (middle)
	w;*dscam1*^{21}/*dscam1*^{21}; *scp2-GAL4, UAS-mCD4::tdGFP/hh-GAL4, UAS-dscam1*$^{17.2}$*::GFP* (***hh-GAL4 &scp2-GAL4 UAS-dscam1***) (bottom)

Table 2.2 | Statistical analyses grouped by figure number and panel, and statistical tests

Figure	Test					
	Mann-Whitney	**n1**	**n2**	**Exact p-value**	***U***	
3B Dendrite Count	WT versus *dscam1* $^{-}$	22	15	<0.0001	120	
3C Axon routing	WT versus *dscam1* $^{-}$	22	15	<0.0001	131	
5B Dendrite Count	*hh* > + versus *hh* > *dscam1 RNAi*	12	14	<0.0001	268	
5E Axon Routing	*hh* > + versus *hh* > *dscam1 RNAi*	12	14	0.0017	242	
	Kruskal-Wallis test followed by Dunn's multiple comparison tests			**Adjusted p-value**	***z***	
5D Dendrite Count	*hh* > + in WT background versus *hh* > + in *dscam1* $^{-}$ background	12	9	0.0002	4.01908	
	hh > + in *dscam1* $^{-}$ background versus *hh* > *dscam1* in *dscam1* $^{-}$ background	9	16	1.0000	0.87597	
	hh > + in WT background versus *hh* > *dscam1* in *dscam1* $^{-}$ background	12	16	0.0007	3.66973	
5F Axon routing	*hh* > + in WT background versus *hh* > + in *dscam1* $^{-}$ background	12	9	0.0012	3.53773	
	hh > + in *dscam1* $^{-}$ background versus *hh* > *dscam1* in *dscam1* $^{-}$ background	9	16	1.0000	0.25691	
	hh > + in WT background versus *hh* > *dscam1* in *dscam1* $^{-}$ background	12	16	0.0005	3.78933	
	Mann-Whitney			**Exact p-value**	***U***	
7B Dendrite Count	*scp2* > + versus *scp2* > *dscam1 RNAi*	12	19	<0.0001	304	
7E Axon Routing	*scp2* > + versus *scp2* > *dscam1 RNAi*	12	19	0.0042	263	
	Kruskal-Wallis test followed by Dunn's multiple comparison tests			**Adjusted p-value**	***z***	
7D Dendrite Count	*scp2* > + in WT background versus *scp2* > + in *dscam1* $^{-}$ background	12	17	0.0001	4.10278	
	scp2 > + in *dscam1* $^{-}$ background versus *scp2* > *dscam1* in *dscam1* $^{-}$ background	17	16	0.7877	1.12036	
	scp2 > + in WT background versus *scp2* > *dscam1* in *dscam1* $^{-}$ background	12	16	<0.0001	5.08455	
7F Axon routing	*scp2* > + in WT background versus *scp2* > + in *dscam1* $^{-}$ background	12	17	<0.0001	4.54159	
	scp2 > + in *dscam1* $^{-}$ background versus *scp2* > *dscam1* in *dscam1* $^{-}$ background	17	16	0.4691	1.41738	
	scp2 > + in WT background versus *scp2* > *dscam1* in *dscam1* $^{-}$ background	12	16	0.0044	3.1786	
	Welch's *t* test			**Adjusted p-value**	***t***	**DF**
8B Fascicle to midline	*scp2* > + in WT background versus *scp2* > + in *dscam1* $^{-}$ background	12	17	0.1585	1.4505	26.937
8C Soma to midline	*scp2* > + in WT background versus *scp2* > + in *dscam1* $^{-}$ background	12	17	<0.0001	4.9343	25.317
	Kruskal-Wallis test followed by Dunn's multiple comparison tests			**Adjusted p-value**	***z***	
9B Dendrite Count	*scp2,hh* > + in WT background versus *scp2,hh* > + in *dscam1* $^{-}$ background	12	11	<0.0001	4.59036	
	scp2,hh > + in *dscam1* $^{-}$ background versus *scp2,hh* > *dscam1* in *dscam1* $^{-}$ background	11	14	0.0004	3.81124	
	scp2,hh > + in WT background versus *scp2,hh* > *dscam1* in *dscam1* $^{-}$ background	12	14	1.0000	0.95042	
9C Axon routing	*scp2,hh* > + in WT background versus *scp2,hh* > + in *dscam1* $^{-}$ background	12	11	0.0005	3.74981	
	scp2,hh > + in *dscam1* $^{-}$ background versus *scp2,hh* > *dscam1* in *dscam1* $^{-}$ background	11	14	0.0003	3.90274	
	scp2,hh > + in WT background versus *scp2,hh* > *dscam1* in *dscam1* $^{-}$ background	12	14	1.0000	0.0000	
10 Soma to midline	*scp2,hh* > + in WT background versus *scp2,hh* > + in *dscam1* $^{-}$ background	12	11	<0.0001	4.24784	
	scp2,hh > + in *dscam1* $^{-}$ background versus *scp2,hh* > *dscam1* in *dscam1* $^{-}$ background	11	14	0.0007	3.6843	
	scp2,hh > + in WT background versus *scp2,hh* > *dscam1* in *dscam1* $^{-}$ background	12	14	1.0000	0.71709	

2.7 METHODS

Fly Stocks

Canton-S was used as a wild-type strain (source: W. Kim). For mutant analyses, *dscam1*^{21} (source: J. Wang) was used. The following lines were obtained from the Bloomington *Drosophila* Stock Center: *UAS-mCD4::tdGFP* (#35836), *UAS-mCD4::tdTomato* (#35841), *UAS-Dscam1 RNAi* (#38945), *hh*-GAL4 (#49437), *Scp2*-GAL4 (#49538), and *Kr-GFP* balancer (#5195). Homozygous mutants were identified using GFP balancers. *hh-GAL4* and *Scp2-GAL4* were used for transgenic expression in MN24 and a subset of the lateral fascicle, respectively, from the Janelia GAL4 stocks. For the rescue experiments in *dscam1*$^{-/-}$, in **Figures 2.3c**, **2.4d**, and **2.5a**, a single isoform of *dscam1* (*UAS-Dscam1*$^{exon\ 17.2}$*-GFP*) (source: T. Lee) was used. Specific fly genotypes in experiments are described in **Table 2.1**. Flies were reared at 25°C using standard procedures.

RNAi Experiments

For cell-specific RNAi experiments, the *UAS-shRNA* line that targets all splice variants known for *dscam1* was obtained from TRiP at Harvard Medical School via BDSC. For all examinations of *dscam1* functions, in **Figures 2.3a** and **2.4b**, the *dscam1* RNAi construct was expressed in various small subsets of neurons (*UAS-mCD4::tdTomato*/+;*UAS-dscam1RNAi*/*GAL4*). Detailed information on used *GAL4* drivers is listed in **Table 2.1**.

Immunohistochemistry

Embryos were fillet-dissected, fixed with 4% paraformaldehyde for 5 min, blocked in a solution of PBS/0.01% Triton X-100 with 0.06% BSA (TBSB) for 1 hour at room temperature (RT). For labeling of *Scp2*-positive lateral fascicle with a reference pattern (anti-Fasciclin II [FasII] and/or anti-Horseradish Peroxidase [HRP]), the embryos were incubated with anti-FasII (mouse mAb,

Developmental Studies Hybridoma Bank; 1:500) in TBSB at 4°C overnight. Samples were washed 3 x 5 min with TBSB and incubated with conjugated anti-HRP (goat mAb, JacksonImmuno; 1:500) and secondary antibodies (Alexa Fluor 647 Donkey anti-mouse, Invitrogen at 1:500) for 2 hours at RT and washed with PBS. Anti-HRP conjugation with fluorescent dyes was performed by following the same procedure as described in previous literature (Inal et al., 2021). Following immunohistochemistry, they were post-fixed with 4% paraformaldehyde for 10 min and mounted in PBS.

Fluorescence Imaging

Confocal microscopy images of fillet embryos expressing green or red fluorescent proteins alongside far-red DiD-labeled neurons were captured using an inverted fluorescence microscope (Ti-E, Nikon) with either 40x 0.80 NA water immersion objective or 100× 1.45 NA oil immersion objective (Nikon). The microscope was attached to the Dragonfly Spinning disk confocal unit (CR-DFLY-501, Andor). Three excitation lasers (40 mW 488 nm, 50 mW 561 nm, and 110 mW 642 nm lasers) were coupled to a multimode fiber passing through the Andor Borealis unit. A dichroic mirror (Dragonfly laser dichroic for 405-488-561-640) and three bandpass filters (525/50 nm, 600/50 nm, and 725/40 nm bandpass emission wheel filters) were placed in the imaging path. Images were recorded with an electron-multiplying charge-coupled device camera (iXon, Andor).

Labelling Dendrites and Quantifying Dendritic Processes in MN24

For phenotypic analyses of dendritic processes in wild-type and mutant backgrounds, DiD labeling (ThermoFisher) of MN24 was performed by following the same procedure as described in the literature (Inal et al., 2020). To minimize the variation in the dendritic processes in MN24 in different segments, neurons from abdominal segments 2 to 7 were imaged. Primary dendritic processes in individual MN24 that were longer than 1.0 mm were counted.

Quantitative measurement of MN24 and *Scp2*-positive lateral fascicle position

MN24 was labeled with DiD and genetically encoded membrane markers (mCD4::tdGFP or mCD4::tdTomato). Similarly, *Scp2*-positive lateral fascicles are marked using the aforementioned genetically encoded membrane markers. Confocal stacks were acquired varying between 0.1 and 0.5 μm z-steps. The distance of the FasII- or *Scp2*-positive lateral fascicle from the midline was measured by first generating the FasII- or *Scp2*-positive lateral fascicle intensity profile perpendicular to the midline. Then, measurements are fitted in a histogram plot. Images were analyzed using Fiji (NIH). Figures were prepared using Adobe Illustrator and Photoshop.

Experimental design and statistical analyses

A between-subject design was employed in all experiments. Immunohistochemistry and dye-labeling experiments were repeated at least two and ten times, respectively, using flies from independent crosses. Statistical analyses were performed and visualized using JMP Pro 16. The results of the statistical tests are shown in **Table 2.2**. All datasets were assessed for normality using Shapiro-Wilk's test, and nonparametric tests were employed when the normality assumption was not met. Comparisons between two groups were analyzed using nonparametric Mann-Whitney U test or parametric Welch's *t* test. Comparisons between multiples groups were analyzed using nonparametric Kruskal-Wallis test. *Post hoc* comparisons were performed using Dunn's multiple comparison test. Error bars are shown as the Standard Error of the Mean (SEM) in the figures.

2.8 ACKNOWLEDGEMENTS

We thank K. Banzai, M. Inal, O. Avraham, and the members of the Kamiyama lab for their insightful comments on the manuscript, and M. Fitch for technical support. This work was funded by the NIH grant (R01NS107558) to D.K.

2.9 AUTHOR CONTRIBUTIONS

D.K. and K.C.B. designed the project, and reviewed and edited the manuscript. K.C.B. produced reagents, performed experiments, curated and analyzed the data, and wrote the original draft of the manuscript. D.K. acquired the funding and supervised the project.

2.10 COMPETING FINANCIAL INTERESTS

The authors declare no competing financial interests.

2.11 REFERENCES

[1] Lanoue, V. and H.M. Cooper, *Branching mechanisms shaping dendrite architecture.* Dev Biol, 2019. **451**(1): p. 16-24.

[2] Yogev, S. and K. Shen, *Establishing Neuronal Polarity with Environmental and Intrinsic Mechanisms.* Neuron, 2017. **96**(3): p. 638-650.

[3] Lefebvre, J.L., J.R. Sanes, and J.N. Kay, *Development of dendritic form and function.* Annu Rev Cell Dev Biol, 2015. **31**: p. 741-77.

[4] Yogev, S. and K. Shen, *Cellular and molecular mechanisms of synaptic specificity.* Annu Rev Cell Dev Biol, 2014. **30**: p. 417-37.

[5] Haverkamp, L.J., *Anatomical and physiological development of the Xenopus embryonic motor system in the absence of neural activity.* J Neurosci, 1986. **6**(5): p. 1338-48.

[6] Verhage, M., et al., *Synaptic assembly of the brain in the absence of neurotransmitter secretion.* Science, 2000. **287**(5454): p. 864-9.

[7] Constance, W.D., et al., *Neurexin and Neuroligin-based adhesion complexes drive axonal arborisation growth independent of synaptic activity.* Elife, 2018. **7**.

[8] Varoqueaux, F., et al., *Total arrest of spontaneous and evoked synaptic transmission but normal synaptogenesis in the absence of Munc13-mediated vesicle priming.* Proc Natl Acad Sci U S A, 2002. **99**(13): p. 9037-42.

[9] Sanes, J.R., *Extracellular matrix molecules that influence neural development.* Annu Rev Neurosci, 1989. **12**: p. 491-516.

[10] Guan, K.L. and Y. Rao, *Signalling mechanisms mediating neuronal responses to guidance cues.* Nat Rev Neurosci, 2003. **4**(12): p. 941-56.

[11] Long, K.R. and W.B. Huttner, *How the extracellular matrix shapes neural development.* Open Biol, 2019. **9**(1): p. 180216.

[12] Howard, L.J., et al., *Midline axon guidance in the Drosophila embryonic central nervous system.* Semin Cell Dev Biol, 2019. **85**: p. 13-25.

[13] Klambt, C., J.R. Jacobs, and C.S. Goodman, *The midline of the Drosophila central nervous system: a model for the genetic analysis of cell fate, cell migration, and growth cone guidance.* Cell, 1991. **64**(4): p. 801-15.

[14] Evans, T.A. and G.J. Bashaw, *Axon guidance at the midline: of mice and flies.* Curr Opin Neurobiol, 2010. **20**(1): p. 79-85.

[15] Kaprielian, Z., E. Runko, and R. Imondi, *Axon guidance at the midline choice point.* Dev Dyn, 2001. **221**(2): p. 154-81.

[16] Kidd, T., et al., *Roundabout controls axon crossing of the CNS midline and defines a novel subfamily of evolutionarily conserved guidance receptors.* Cell, 1998. **92**(2): p. 205-15.

[17] Kidd, T., K.S. Bland, and C.S. Goodman, *Slit is the midline repellent for the robo receptor in Drosophila.* Cell, 1999. **96**(6): p. 785-94.

[18] Brose, K., et al., *Slit proteins bind Robo receptors and have an evolutionarily conserved role in repulsive axon guidance.* Cell, 1999. **96**(6): p. 795-806.

[19] Hiramoto, M., et al., *The Drosophila Netrin receptor Frazzled guides axons by controlling Netrin distribution.* Nature, 2000. **406**(6798): p. 886-9.

20. Harris, R., L.M. Sabatelli, and M.A. Seeger, *Guidance cues at the Drosophila CNS midline: identification and characterization of two Drosophila Netrin/UNC-6 homologs.* Neuron, 1996. **17**(2): p. 217-28.

[21] Furrer, M.P., et al., *Slit and Robo control the development of dendrites in Drosophila CNS.* Development, 2007. **134**(21): p. 3795-804.

[22] Furrer, M.P., et al., *Robo and Frazzled/DCC mediate dendritic guidance at the CNS midline.* Nat Neurosci, 2003. **6**(3): p. 223-30.

[23] Mauss, A., et al., *Midline signalling systems direct the formation of a neural map by dendritic targeting in the Drosophila motor system.* PLoS Biol, 2009. **7**(9): p. e1000200.

[24] Organisti, C., et al., *Flamingo, a seven-pass transmembrane cadherin, cooperates with Netrin/Frazzled in Drosophila midline guidance.* Genes Cells, 2015. **20**(1): p. 50-67.

[25] Alavi, M., et al., *Dscam1 Forms a Complex with Robo1 and the N-Terminal Fragment of Slit to Promote the Growth of Longitudinal Axons.* PLoS Biol, 2016. **14**(9): p. e1002560.

[26] Kamiyama, D., et al., *Specification of Dendritogenesis Site in Drosophila aCC Motoneuron by Membrane Enrichment of Pak1 through Dscam1.* Dev Cell, 2015. **35**(1): p. 93-106.

[27] Schmucker, D., et al., *Drosophila Dscam is an axon guidance receptor exhibiting extraordinary molecular diversity.* Cell, 2000. **101**(6): p. 671-84.

[28] Dong, H., et al., *Self-avoidance alone does not explain the function of Dscam1 in mushroom body axonal wiring.* Curr Biol, 2022. **32**(13): p. 2908-2920 e4.

2[9] Zhu, H., et al., *Dendritic patterning by Dscam and synaptic partner matching in the Drosophila antennal lobe.* Nat Neurosci, 2006. **9**(3): p. 349-55.

[30] Wojtowicz, W.M., et al., *Alternative splicing of Drosophila Dscam generates axon guidance receptors that exhibit isoform-specific homophilic binding.* Cell, 2004. **118**(5): p. 619-33.

[31] Zhan, X.L., et al., *Analysis of Dscam diversity in regulating axon guidance in Drosophila mushroom bodies.* Neuron, 2004. **43**(5): p. 673-86.

[32] Goyal, G., et al., *Inter-axonal recognition organizes Drosophila olfactory map formation.* Sci Rep, 2019. **9**(1): p. 11554.

[33] Liu, C., et al., *Dscam1 establishes the columnar units through lineage-dependent repulsion between sister neurons in the fly brain.* Nat Commun, 2020. **11**(1): p. 4067.

[34] Wilhelm, N., et al., *Dscam1 Has Diverse Neuron Type-Specific Functions in the Developing Drosophila CNS.* eNeuro, 2022. **9**(4).

[35] Vactor, D.V., et al., *Genes that control neuromuscular specificity in Drosophila.* Cell, 1993. **73**(6): p. 1137-53.

[36] Sink, H. and P.M. Whitington, *Location and connectivity of abdominal motoneurons in the embryo and larva of Drosophila melanogaster.* J Neurobiol, 1991. **22**(3): p. 298-311.

[37] Hoang, B. and A. Chiba, *Single-cell analysis of Drosophila larval neuromuscular synapses.* Dev Biol, 2001. **229**(1): p. 55-70.

[38] Landgraf, M., et al., *The origin, location, and projections of the embryonic abdominal motorneurons of Drosophila.* J Neurosci, 1997. **17**(24): p. 9642-55.

[39] Landgraf, M., et al., *Embryonic origins of a motor system: motor dendrites form a myotopic map in Drosophila.* PLoS Biol, 2003. **1**(2): p. E41.

[40] Landgraf, M., et al., *Charting the Drosophila neuropile: a strategy for the standardised characterisation of genetically amenable neurites.* Dev Biol, 2003. **260**(1): p. 207-25.

[41] Yamagata, M. and J.R. Sanes, *Dscam and Sidekick proteins direct lamina-specific synaptic connections in vertebrate retina.* Nature, 2008. **451**(7177): p. 465-9.

[42] Winding, M., et al., *The connectome of an insect brain.* Science, 2023. **379**(6636): p. eadd9330.

[43] Saalfeld, S., et al., *CATMAID: collaborative annotation toolkit for massive amounts of image data.* Bioinformatics, 2009. **25**(15): p. 1984-6.

[44] Tomer, R., et al., *Quantitative high-speed imaging of entire developing embryos with simultaneous multiview light-sheet microscopy.* Nat Methods, 2012. **9**(7): p. 755-63.

[45] Sun, W., et al., *Ultra-deep profiling of alternatively spliced Drosophila Dscam isoforms by circularization-assisted multi-segment sequencing.* EMBO J, 2013. **32**(14): p. 2029-38.

[46] Wojtowicz, W.M., et al., *A vast repertoire of Dscam binding specificities arises from modular interactions of variable Ig domains.* Cell, 2007. **130**(6): p. 1134-45.

[47] Hattori, D., et al., *Robust discrimination between self and non-self neurites requires thousands of Dscam1 isoforms.* Nature, 2009. **461**(7264): p. 644-8.

[48] Hattori, D., et al., *Dscam diversity is essential for neuronal wiring and self-recognition.* Nature, 2007. **449**(7159): p. 223-7.

[49] Zou, W., et al., *A multi-protein receptor-ligand complex underlies combinatorial dendrite guidance choices in C. elegans.* Elife, 2016. **5**.

[50] Sundararajan, L., J. Stern, and D.M. Miller, 3rd, *Mechanisms that regulate morphogenesis of a highly branched neuron in C. elegans.* Dev Biol, 2019. **451**(1): p. 53-67.

[51] Dascenco, D., et al., *Slit and Receptor Tyrosine Phosphatase 69D Confer Spatial Specificity to Axon Branching via Dscam1.* Cell, 2015. **162**(5): p. 1140-54.

[52] Andrews, G.L., et al., *Dscam guides embryonic axons by Netrin-dependent and -independent functions.* Development, 2008. **135**(23): p. 3839-48.

[53] Liu, G., et al., *DSCAM functions as a netrin receptor in commissural axon pathfinding.* Proc Natl Acad Sci U S A, 2009. **106**(8): p. 2951-6.

[54] Evans, T.A., *Embryonic axon guidance: insights from Drosophila and other insects.* Curr Opin Insect Sci, 2016. **18**: p. 11-16.

[55] Fazeli, A., et al., *Phenotype of mice lacking functional Deleted in colorectal cancer (Dcc) gene.* Nature, 1997. **386**(6627): p. 796-804.

[56] Kolodziej, P.A., et al., *frazzled encodes a Drosophila member of the DCC immunoglobulin subfamily and is required for CNS and motor axon guidance.* Cell, 1996. **87**(2): p. 197-204.

[57] Mitchell, K.J., et al., *Genetic analysis of Netrin genes in Drosophila: Netrins guide CNS commissural axons and peripheral motor axons.* Neuron, 1996. **17**(2): p. 203-15.

[58] Cohen, O., et al., *Roles of DSCAM in axonal decussation and fasciculation of chick spinal interneurons.* Int J Dev Biol, 2017. **61**(3-4-5): p. 235-244.

[59] Avraham, O., et al., *Transcriptional control of axonal guidance and sorting in dorsal interneurons by the Lim-HD proteins Lhx9 and Lhx1.* Neural Dev, 2009. **4**: p. 21.

[60] Avraham, O., et al., *Motor and dorsal root ganglion axons serve as choice points for the ipsilateral turning of dI3 axons.* J Neurosci, 2010. **30**(46): p. 15546-57.

[61] Inal, M.A., et al., *Imaging of In Vitro and In Vivo Neurons in Drosophila Using Stochastic Optical Reconstruction Microscopy.* Curr Protoc, 2021. **1**(7): p. e203.

[62] Inal, M.A., K. Banzai, and D. Kamiyama, *Retrograde Tracing of Drosophila Embryonic Motor Neurons Using Lipophilic Fluorescent Dyes.* J Vis Exp, 2020(155).

CHAPTER 3

CRISPR/CAS9-MEDIATED KNOCK-IN IN *EBONY* GENE USING A PCR PRODUCT DONOR TEMPLATE IN *DROSOPHILA*[3]

[3] Bui, K. C., and Kamiyama, D. Reprinted here with permission of publisher.

3.1 ABSTRACT

CRISPR/Cas9 technology has been a powerful tool for gene editing in *Drosophila*, particularly for knocking in base-pair mutations or a variety of gene cassettes into endogenous gene loci. Among the *Drosophila* community, there has been a concerted effort to establish CRISPR/Cas9-mediated knock-in protocols that decrease the amount of time spent on molecular cloning. Here, we report the CRISPR/Cas9-mediated insertion of a ~50 base-pair sequence into the *ebony* gene locus, using a linear double-stranded DNA (PCR product) donor template. By circumventing the cloning step of the donor template, our approach suggests the PCR product as a useful, alternative knock-in donor format.

3.2 INTRODUCTION

Since the advent of the CRISPR/Cas9 technology, gene editing in many model organisms, including *Drosophila melanogaster*, has been a common approach for many researchers to study and modify specific gene functions [1,2]. One of the features of the CRISPR/Cas9 system is its ability to disrupt gene function by introducing out-of-frame indel mutations into a target genomic locus [1,3,4]. In addition, the CRISPR/Cas9 system can also be used to precisely insert visible markers (e.g., cassettes encoding fluorescent proteins) to study the localization of live, endogenous proteins within their native environments [5–9].

Drosophila melanogaster is an important model system for gene editing due to its usefulness to study human diseases since about 2,276 genes in flies are conserved and linked to human diseases [10]. Taking advantage of the evolutionarily conserved genes and genetic tractability, the *Drosophila* "Gene Disruption Project" uses a reverse genetics approach to precisely insert reporters or disrupt homologous fly genes to elucidate multiple molecular

mechanisms that underlie their disease phenotypes [5,11,12]. To generate these transgenic lines in an efficient and scalable manner, there has been a concerted effort among the *Drosophila* community to characterize more time- and cost-effective approaches and protocols for CRISPR/Cas9-mediated gene editing within the last decade [1,2,5,6,8].

Initially, researchers used plasmid donor templates containing long (>1kb) homology arms for knock-in in *Drosophila* [1,3,4,13]. Constructing these large plasmid donor templates required extensive molecular cloning [14]. As a result, there have been approaches that have looked towards decreasing the amount of time towards molecular cloning in preparation for CRISPR/Cas9-mediated knock-in in *Drosophila*. One way to bypass cloning the donor template is to use single-stranded oligonucleotide donors – which can be outsourced by a commercial entity [1,12,14–17]. For example, Port et al. successfully introduced an 11 bp mutation containing a restriction enzyme site into the *ebony* genomic locus, using a 50 nt single-stranded oligonucleotide donor and thus, demonstrating a single-stranded oligonucleotide as a cloning-free donor format for CRISPR/Cas9-mediated insertion [1]. Nowadays, custom plasmids can be synthesized by tech companies in a cost-effective manner, especially if the gene cassette is short (<1kb). For instance, Kanca et al. utilized commercially synthesized plasmid donor templates in combination with an *in vivo* linearization strategy – a process in which the specific gRNA cuts linearize the plasmid construct *in vivo* upon injection – for CRISPR/Cas9-mediated knock-in in multiple gene loci in *Drosophila* [5].

Using linear double-stranded DNA (PCR product) donors could also decrease the time towards molecular cloning. PCR products require no cloning, can be generated within two hours, and can be readily scaled for high-throughput library generation. PCR product donors have previously been used for CRISPR/Cas9-mediated insertions in *Drosophila in vitro* [8,19] but, so

far, not *in vivo*. To demonstrate the PCR product as a cloning-free, alternative donor format, we knock in a short disruptive cassette into the *ebony* gene of fruit flies [5].

3.3 RESULTS

To gauge gene editing using the CRISPR/Cas9 system in *Drosophila*, previous reports historically have introduced indel mutations into a specific gene locus: *ebony* on the third chromosome [1,3,20,21]. Flies with a homozygous loss-of-function *ebony* mutation (e.g., $TM3,e^{1}/TM6b,e^{1}$) are known to display a dark cuticle phenotype – thereby facilitating the screening of successful editing events [1,3,6]. More recently, to benchmark the approach for insertion of a novel donor format, Bosch et al. have used the *ebony* locus to demonstrate CRISPR/Cas9-mediated, homology-independent insertion of a linearized donor plasmid [6].

Similarly, to benchmark CRISPR/Cas9-mediated knock-in using the PCR product donor, we targeted the *ebony* gene by cutting at a site 25 bp downstream of the translational start codon of the *ebony* gene, using *ebony*-gRNA (**Figure 3.1a**), as previously described by Port et al. [1]. We injected a premixed solution of a plasmid expressing the *ebony*-gRNA and the PCR product donor template into embryos ubiquitously expressing the Cas9 endonuclease. For the knock-in, we used a PCR product donor template that contains a disruptive gene cassette (three tandem stop codons in different reading frames and a mini-PolyA tail, flanked by 90 bp homology arms; adapted from Kanca et al.) [5] (**Figure 3.1b**).

To determine whether the PCR product donor could yield a knock-in event, we extracted the genomic DNA from 700-embryo pools 24 hours after injection and amplified a DNA fragment using a set of primers that recognizes a region internal to the knock-in site on the 5’ end and a

downstream region of *ebony* on the 3' end. The knock-in allele-specific PCR should yield an expected amplicon of 991 bp (**Figure 3.1b**).

It has been known that different concentrations of an injected plasmid donor template can affect the frequency of knock-in integration in *Drosophila* [3,6]. To assess the concentration of PCR product donor for knock-in, we tested concentrations from 0-700 ng/μL. Using the primer set recognizing the knock-in site within the *ebony* gene, we found that the pooled embryos injected with the PCR product donor template yielded an amplicon corresponding with the expected size of 991 bp, suggesting precise insertions of the PCR product donor into *ebony* (**Figure 3.2a**). Interestingly, we found that pooled embryos injected with the highest concentration of PCR product donor (700 ng/μL) yielded an additional faint band containing a shorter DNA amplicon. This downshifted band suggests that imprecise integration of the disruptive cassette may occur when a high concentration of PCR product donor is injected.

To avoid imprecise knock-in events, we injected the *ebony*-gRNA with 70 ng/μL of the PCR product donor template into the Cas9-expressing embryos for all subsequent microinjections. In total, we injected 2800 embryos, of which 155 flies (5.5%) survived after the microinjection process – which we refer to as G_0 survivors (**Figure 3.2b**). 75 single G_0 male survivors were then crossed with female *ebony* loss-of-function mutants (*TM3,*e^1*/TM6b,*e^1). Only single crosses that generated at least 50 G_1 progenies were counted towards the rate of successful crosses; 43 G_0 male survivors (57.3%) had successful crosses (**Figure 3.2b**).

The G_1 progeny were then screened for the dark cuticle phenotype, indicative of a germline-transmitted CRISPR/Cas9-mediated editing event (**Figure 3.2c**). For this study, we coined "$e^{93C7CRISPR}$" as the allele with the inserted disruptive cassette in the *ebony* gene (located in the 93C7 cytogenetic region). Upon successful integration of the disruptive cassette, G_1 progeny

with the dark cuticle phenotype would contain the *ebony*^{93C7CRISPR} and *ebony*^{1} alleles (*e*^{93C7CRISPR}/*TM6b,e*^{1}) (**Figure 3.2c**). To determine whether a knock-in event occurred, we verified the integration of the disruptive cassette by PCR validation (**Figure 3.2d**). We extracted genomic DNA from each individual fly and amplified the DNA fragment, using the same primer set recognizing the knock-in site within the *ebony* locus. G_1 progeny containing the inserted disruptive cassette (*e*^{93C7CRISPR}/*TM6b,e*^{1}) yielded the expected 991 bp band whereas G_1 progeny without the knock-in event (+/*TM6b,e*^{1}) or female homozygous for the *ebony*^{1} allele (*TM3,e*^{1}/*TM6b,e*^{1}) did not yield any amplicon (**Figure 3.2d**). Thus, our screening approach could detect the germline-transmitted knock-in event in the *ebony* gene.

Finally, from these G_1 progeny, siblings with the dark cuticle phenotype were crossed to generate homozygous (*e*^{93C7CRISPR}/*e*^{93C7CRISPR}) flies, to which we validated the insertion of the disruptive cassette into the *ebony* gene by Sanger sequencing (**Figure 3.2e**). Based on this representative sequencing data, the insertion of the disruptive cassette was without additional random insertions or deletions in the *ebony* gene. Overall, 4 out of 43 crosses (9.3%) successfully passed down the germline-transmitted knock-in cassette to their progeny (**Figure 3.2b**). This founder rate (9.3%) is comparable to that reported by Kanca et al., in which they reported rates roughly ranging from 2-12% using their *in vivo* linearized disruptive donor cassette – thus, corroborating with this study's germline-transmitted knock-in rate using PCR product as a donor template [5].

3.4 DISCUSSION

Altogether, these data show that the PCR product as a donor format can be useful for germline-transmitted knock-in into the *ebony* gene in *Drosophila*. While we show that the founder rate using

the PCR product donor template is comparable to that of other donor formats from previous literature, we noted that our survival rate is lower than those of previous reports, which roughly range from 10-45% after injecting a gene-specific gRNA and donor template [5,6]. To address if the PCR product donor affects survival rate, we injected embryos with ebony-sgRNA alone and saw no significant difference between those injected with or without the PCR product donor (**Supplementary Figure 3.1**). This suggests that the observed survival rate may be due to the laboratory-to-laboratory variation, such as the microinjection process [22]. For example, we dissolved the CRISPR/Cas9 components in TE buffer rather than an in-house formulated injection buffer for microinjections [18,23]. Optimization in injection buffer compositions may further improve the survival rate. However, this parameter remains to be empirically tested in *Drosophila* and is not covered in this study.

Additional studies are required for generating knock-ins using the PCR product donor. These studies would be important for determining whether this approach using a PCR product donor would be useful for scalable generation of a collection of mutant fly lines as the "Gene Disruption Project" is aiming for [5,11,12]. A previous study has shown that a long gene cassette (>1000 bp), using a PCR product donor, can be integrated into the *Drosophila* genome in a cell culture system [8]. Whether *in vivo* knock-in of a long gene cassette (>1000 bp) remains to be tested. Their knock-in strategy also utilized short homology arms (<100 bp) [8]. Homology arm length is a factor to be considered for this approach as most commercially available primers are capped within a 100 bp length. Currently, the scope of this study is focused on knock-in occurring within the *ebony* gene but paves the way for this knock-in approach to be expanded to other genes in the future.

3.5 FIGURES

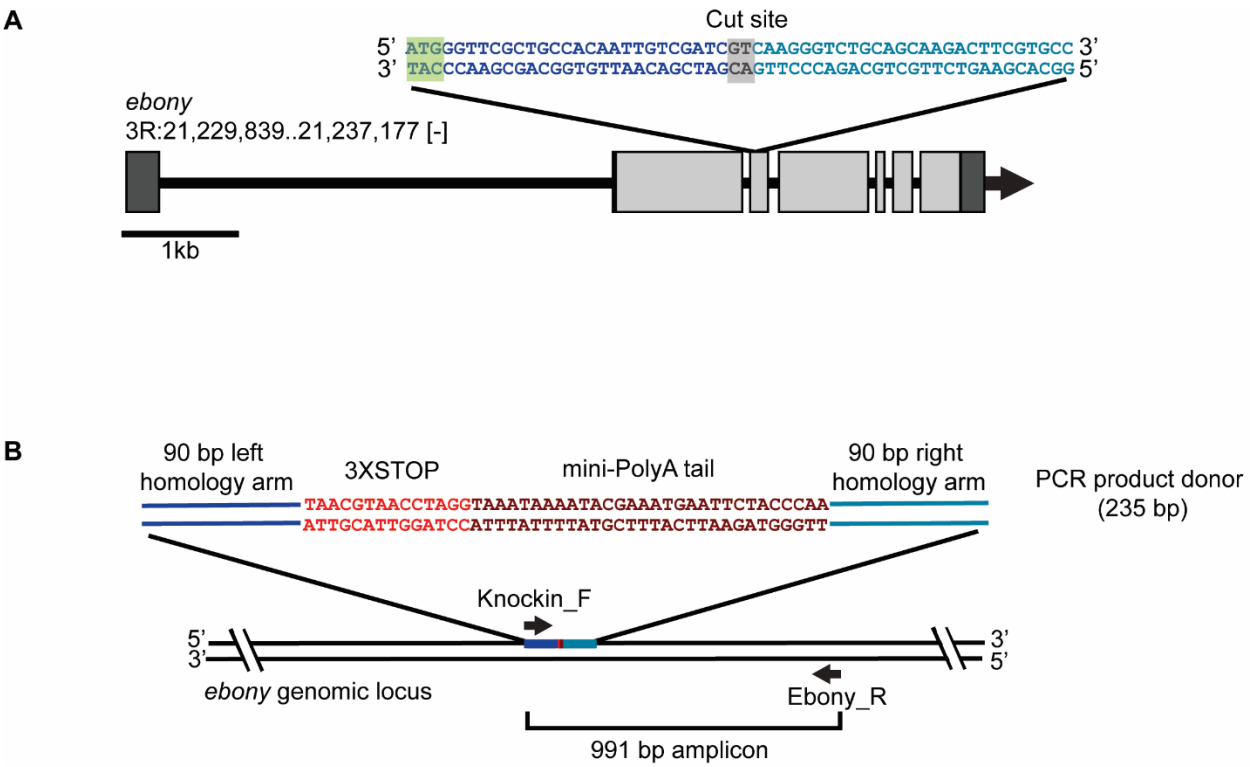

Figure 3.1 | Schematic of strategy using PCR product as a donor for CRISPR/Cas9-mediated knock-in in *ebony* gene (**a**) Schematic of the target site of *ebony*-gRNA in the second exon of the *ebony* gene. Boxes indicate exons (light gray) and untranslated regions (dark gray). Highlighted texts are the cut site targeted by Cas9 endonuclease (gray) and start codon (green). Texts in dark blue and light blue indicate the sequences that flank the cut site. (**b**) The PCR product donor containing the disruptive gene cassette for insertion into the cut site of *ebony*. The disruptive donor cassette contains three stop codons in all reading frames (red) and a mini-PolyA tail (dark red), flanked by 90 bp homology arms (dark blue and light blue). Black arrows indicate the primer set (Knockin_F and Ebony_R) used to amplify the 991 bp region to confirm the knock-in event in the *ebony* genomic locus.

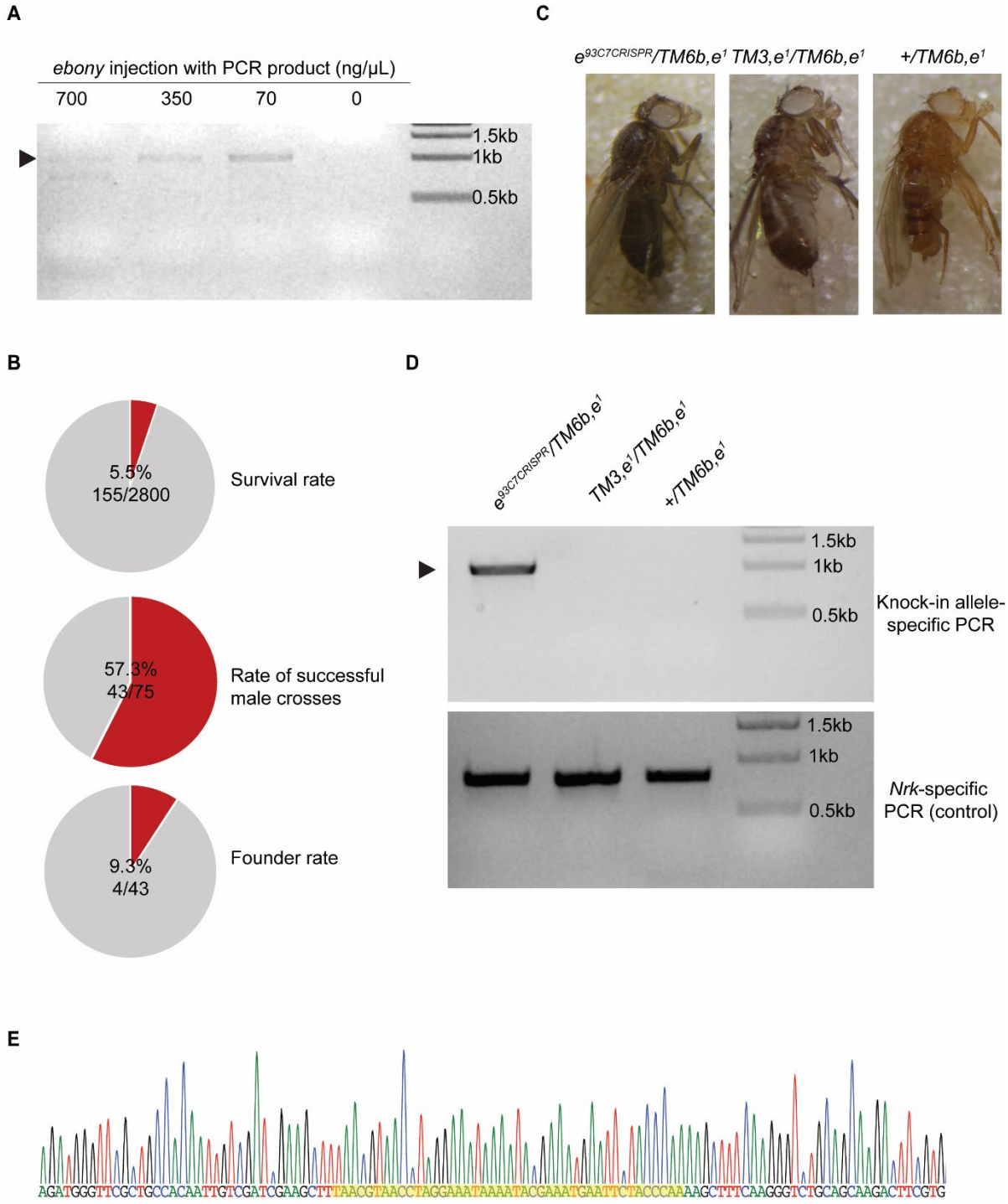

Figure 3.2 | Germline-transmitted CRISPR/Cas9-mediated knock-in in *ebony* gene using a PCR product donor template (**a**) Knock-in events detected using different concentrations (700,

350, 70, 0 ng/μL) of PCR product donor template injected into 700-embryo pools. 1% agarose gel image shows the amplicons from knock-in allele-specific PCR, using 15ng of genomic DNA and primer set Knockin_F and Ebony_R (see **Figure 3.1b**). Arrowhead indicates the band of the expected 991 bp amplicon. (**b**) Survival, successful cross, and founder rates, using PCR product donor for CRISPR/Cas9-mediated insertion of the disruptive cassette into *ebony*. *Drosophila* embryos were injected with a pre-mixed solution of the PCR product donor template and gRNA plasmid (see *Embryo Microinjection* in Materials and Methods). (**c**) Images of a G_1 $e^{93C7CRISPR}/TM6b,e^{1}$ fly with knock-in of the disruptive donor cassette (left) compared to a $TM3,e^{1}/TM6b,e^{1}$ fly (middle) and a sibling G_1 $+/TM6b,e^{1}$ fly without the knock-in event (right). (**d**) Top and bottom agarose gel images show the amplicon products from PCR. For the top gel image, shown is the amplified fragment of the knock-in region in an individual G_1 $e^{93C7CRISPR}/TM6b,e^{1}$ fly, resulting from the successful incorporation of the PCR product (first lane) into the *ebony* genomic locus. No amplified fragment from the $TM3,e^{1}/TM6b,e^{1}$ fly (second lane) or the sibling G_1 $+/TM6b,e^{1}$ fly (third lane), as a result of no incorporation of the PCR product donor. Primer set (Knockin_F and Ebony_R) is used for knock-in allele-specific PCR (see **Figure 3.1b**). For the bottom gel image, a primer set (Nrk_F and Nrk_R) is used for *Neurospecific receptor kinase (Nrk*) gene-specific PCR (control for DNA quality). Arrowhead indicates the band of the 991 bp amplicon from knock-in allele-specific PCR. Each lane contains the PCR amplification from the genomic DNA of a single fly. (**e**) Sequencing chromatogram of the PCR product amplified from a homozygous fly derived from successful knock-in of PCR product donor. The yellow highlighted region indicates the incorporated three stop codons and mini-PolyA tail in the *ebony* genomic locus.

3.6 SUPPLEMENTARY FIGURES

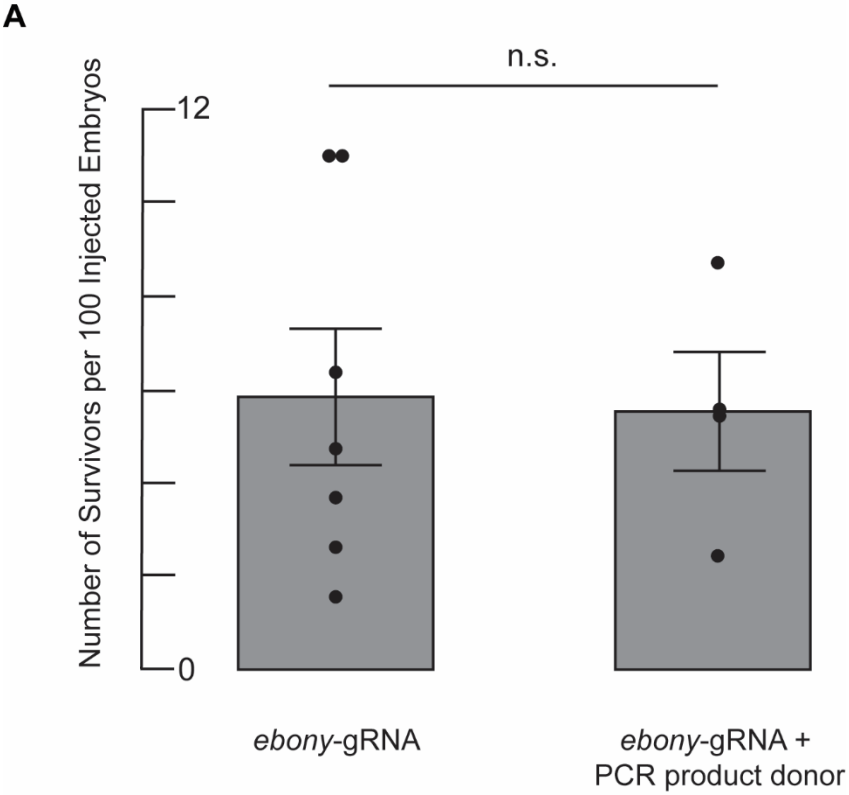

Supplementary Figure 3.1 | Survival rate of injected embryos is independent of PCR product donor template (**a**) Comparison of the survival rates of embryos injected with either *ebony*-gRNA alone or *ebony*-gRNA and PCR product donor for CRISPR/Cas9-mediated insertion of the disruptive cassette into *ebony*. Each data point represents an independent microinjection trial. Error bars represent ±SEM. n.s indicates not significant. Statistical analysis was done by student's t-test.

3.7 METHODS

Plasmid preparation

For gRNA generation, plasmids were generated using the general following protocol. DNA fragments were amplified using Q5 High-Fidelity DNA Polymerase (NEB). Thermocycling conditions are as followed: 98°C for 30 s (denaturation), 98°C for 10 s, 52°C for 10 s, and 72°C for 45 s for 30 cycles, and 72°C for 2 min.

pCFD4-U6:1_U6:3tandemgRNAs (Plasmid #49411) was digested using BbsI-HF (NEB) at 37°C for 16h. The vector backbone and amplified DNA fragment were then gel-purified using NucleoSpin Gel and PCR Clean-up Kit (Macherey-Nagel #740609) and assembled using In-Fusion HD Cloning Plus Kit (Takara Bio #638910).

Chemically competent *E. coli* strain (Takara Bio #636763) was transformed and selected on LB-agar plates with ampicillin. Plasmids were isolated and amplified from colonies using ZymoPURE Plasmid Miniprep Kit (Zymo Research #D4209) and sequenced at Eton Bioscience Inc. Primer sequences for gRNA plasmid construction are listed below:

- *ebony*-gRNA forward primer: 5′-TATATAGGAAAGATATCCGGGTGAACTTCGCCACAATTGTCGATCGTCAGTTTTAGAGCTAGAAATAGCAAG-3’
- *ebony*-gRNA reverse primer: 5′-ATTTTAACTTGCTATTTCTAGCTCTAAAACTGACGATCGACAATTGTGGCGACGTTAAATTGAAAATAGGTC-3’

The disruptive donor cassette was synthesized and cloned into pUCIDT vector at Integrated DNA Technologies. Templates for dsDNA construct were ordered as followed:

- Disrup-dsDNA: 5'-

  GTAGTACGATCATAACAACGCGGTCCGACTGAGATTCTAAGCCCAAAACTAA

  CAAAGTATTCCCCACAGTTAATATATCTTCAAGATGGGTTCGCTGCCACAATT

  GTCGATCGTTCGAATAACGTAACCTAGGAAATAAAATACGAAATGAATTCTA

  CCCAATTCGAATCAAGGGTCTGCAGCAAGACTTCGTGCCTAGAGCTCTGCAC

  CGCATCTTCGAGGAGCAGCAGCTGCGGCATGCCGACAAGGTGGCTCTGACCG

  CGTTGTTATGATCGTACTAC-3'

Upon synthesis of the plasmid template donor, we amplify a DNA fragment to use as the PCR product donor. Primer sequences for PCR product donor construction are listed as followed:

- Disrup-PCRdonor forward primer: 5'-TCCGACTGAGATTCTAAGCC-3'
- Disrup-PCRdonor reverse primer: 5'-TCAGAGCCACCTTGTCGG-3'

Embryo microinjection

The CRISPR/Cas9 components were prepared in TE buffer at these final concentrations: *ebony*-gRNA plasmid: 300 ng/µL; Disruptive donor cassette (PCR product): 70 ng/µL.

CRISPR/Cas9 components were mixed and co-injected into 700 y[1] =qM{w[+mC]=Act5C-Cas9.P}ZH-2A w[*] (BDSC# 54590) embryos during the syncytial stage of development for each trial. 4 microinjection trials were performed. Microinjections were performed at 18°C, and embryos were moved to 25°C, following injection. Flies were cultured on standard fly food at 25°C. Injected G_0 males were crossed with y[1] w[*]; TM3,e^1 Sb[1]/TM6b,e^1 Tb[+] (BDSC# 3720) females, and their subsequent G_1 progeny were screened and validated for knock-in.

Genomic DNA Extraction

Genomic DNA was extracted from individual flies using DNAzol (Invitrogen #10503027) or PureLink Genomic DNA Mini Kit (Invitrogen #K182001), according to the manufacturer's protocol. DNA concentration was measured using the NanoPhotometer C40 (Implen).

PCR validation

Primer set (Knockin_F and Ebony_R) recognizing the knock-in region on the 5' end and the downstream 3' region of *ebony* was used to amplify a 991 bp product. Primer set (Nrk_F and Nrk_R) was used for *Nrk* gene-specific PCR as a control for DNA quality. PCR validation used the genomic DNA prepared from individual flies and was amplified using Taq 2X Master Mix (NEB #M0270L). Thermocycling conditions are as followed: 95°C for 30 s (denaturation), 95°C 30 s, 60°C 30 s, 68°C 1 min for 30 cycles, and 68°C 5 min.

Primer sequences for PCR validation are listed below:

- Knockin_F primer: 5'-CGATCGAAGCTTTAACGTAACCT-3'
- Ebony_R primer: 5'-GATAGGGGTTCTCCGGAGCAGACC-3'
- Nrk_F primer: 5'-GCACATGGCGGTAAAGATCG-3'
- Nrk_R primer: 5'-GTGAGATCAGAGGGGCATCT-3'

3.8 ACKNOWLEDGEMENTS

We thank K. Banzai and members of the Kamiyama lab for their insightful comments on the manuscript; K. Banzai for *Nrk* gene-specific primer set; R. Kamiyama for *ebony*-gRNA plasmid; and M. Fitch for technical support. This work was supported by an NIH R01 NS107558 (to D.K.).

3.9 AUTHOR CONTRIBUTIONS

D.K. and K.C.B. designed the project and edited the manuscript. K.C.B. produced reagents, performed experiments, analyzed the data, and wrote the manuscript.

3.10 COMPETING FINANCIAL INTERESTS

The authors declare no competing financial interests.

3.11 REFERENCES

[1] F. Port, H.M. Chen, T. Lee, S.L. Bullock, Optimized CRISPR/Cas tools for efficient germline and somatic genome engineering in Drosophila, Proc. Natl. Acad. Sci. U. S. A. (2014). https://doi.org/10.1073/pnas.1405500111.

[2] S.J. Gratz, A.M. Cummings, J.N. Nguyen, D.C. Hamm, L.K. Donohue, M.M. Harrison, J. Wildonger, K.M. O'connor-Giles, Genome engineering of Drosophila with the CRISPR RNA-guided Cas9 nuclease, Genetics. (2013). https://doi.org/10.1534/genetics.113.152710.

[3] F. Port, N. Muschalik, S.L. Bullock, Systematic Evaluation of Drosophila CRISPR Tools Reveals Safe and Robust Alternatives to Autonomous Gene Drives in Basic Research, Genetics. 5 (2015) 1493–1502. https://doi.org/10.1534/g3.115.019083.

[4] S.J. Gratz, F.P. Ukken, C.D. Rubinstein, G. Thiede, L.K. Donohue, A.M. Cummings, K.M. Oconnor-Giles, Highly specific and efficient CRISPR/Cas9-catalyzed homology-directed repair in Drosophila, Genetics. (2014). https://doi.org/10.1534/genetics.113.160713.

[5] O. Kanca, J. Zirin, J. Garcia-Marques, S.M. Knight, D. Yang-Zhou, G. Amador, H.

Chung, Z. Zuo, L. Ma, Y. He, W.W. Lin, Y. Fang, M. Ge, S. Yamamoto, K.L. Schulze, Y. Hu, A.C. Spradling, S.E. Mohr, N. Perrimon, H.J. Bellen, An efficient CRISPR-based strategy to insert small and large fragments of DNA using short homology arms, Elife. (2019). https://doi.org/10.7554/eLife.51539.

[6] J.A. Bosch, R. Colbeth, J. Zirin, N. Perrimon, Gene knock-ins in Drosophila using homology-independent insertion of universal donor plasmids, Genetics. (2020). https://doi.org/10.1534/genetics.119.302819.

[7] J. Xu, A.R. Kim, R.W. Cheloha, F.A. Fischer, J.S.S. Li, Y. Feng, E. Stoneburner, R. Binari, S.E. Mohr, J. Zirin, H. Ploegh, N. Perrimon, Protein visualization and manipulation in Drosophila through the use of epitope tags recognized by nanobodies, Elife. 11 (2022). https://doi.org/10.7554/eLife.74326.

[8] S. Kunzelmann, R. Böttcher, I. Schmidts, K. Förstemann, A comprehensive toolbox for genome editing in cultured Drosophila melanogaster cells, G3 Genes, Genomes, Genet. 6 (2016). https://doi.org/10.1534/g3.116.028241.

[9] H. Kina, T. Yoshitani, K. Hanyu-Nakamura, A. Nakamura, Rapid and efficient generation of GFP-knocked-in Drosophila by the CRISPR-Cas9-mediated genome editing, Dev. Growth Differ. (2019) dgd.12607. https://doi.org/10.1111/dgd.12607.

[10] S. Yamamoto, M. Jaiswal, W.L. Charng, T. Gambin, E. Karaca, G. Mirzaa, W. Wiszniewski, H. Sandoval, N.A. Haelterman, B. Xiong, K. Zhang, V. Bayat, G. David, T. Li, K. Chen, U. Gala, T. Harel, D. Pehlivan, S. Penney, L.E.L.M. Vissers, J. De Ligt, S.N. Jhangiani, Y. Xie, S.H. Tsang, Y. Parman, M. Sivaci, E. Battaloglu, D. Muzny, Y.W. Wan, Z. Liu, A.T. Lin-Moore, R.D. Clark, C.J. Curry, N. Link, K.L. Schulze, E. Boerwinkle, W.B. Dobyns, R. Allikmets, R.A. Gibbs, R. Chen, J.R. Lupski, M.F.

Wangler, H.J. Bellen, A drosophila genetic resource of mutants to study mechanisms underlying human genetic diseases, Cell. 159 (2014). https://doi.org/10.1016/j.cell.2014.09.002.

[11] A.C. Spradling, D. Stern, A. Beaton, E.J. Rhem, T. Laverty, N. Mozden, S. Misra, G.M. Rubin, The Berkeley Drosophila Genome Project gene disruption project: Single P-element insertions mutating 25% of vital Drosophila genes, Genetics. 153 (1999). https://doi.org/10.1093/genetics/153.1.135.

[12] H.J. Bellen, R.W. Levis, G. Liao, Y. He, J.W. Carlson, G. Tsang, M. Evans-Holm, P.R. Hiesinger, K.L. Schulze, G.M. Rubin, R.A. Hoskins, A.C. Spradling, The BDGP gene disruption project: Single transposon insertions associated with 40% of Drosophila genes, Genetics. 167 (2004). https://doi.org/10.1534/genetics.104.026427.

[13] Z. Xue, M. Ren, M. Wu, J. Dai, Y.S. Rong, G. Gao, Efficient gene knock-out and knock-in with transgenic cas9 in Drosophila, G3 Genes, Genomes, Genet. (2014). https://doi.org/10.1534/g3.114.010496.

[14] X. Zhang, W.H. Koolhaas, F. Schnorrer, A versatile two-step CRISPR- and RMCE-based strategy for efficient genome engineering in Drosophila, G3 Genes, Genomes, Genet. 4 (2014). https://doi.org/10.1534/g3.114.013979.

[15] T. Levi, A. Sloutskin, R. Kalifa, T. Juven-Gershon, O. Gerlitz, Efficient in Vivo Introduction of Point Mutations Using ssODN and a Co-CRISPR Approach, Biol. Proced. Online. 22 (2020). https://doi.org/10.1186/s12575-020-00123-7.

[16] J. Zirin, J. Bosch, R. Viswanatha, S.E. Mohr, N. Perrimon, State-of-the-art CRISPR for in vivo and cell-based studies in Drosophila, Trends Genet. 38 (2022). https://doi.org/10.1016/j.tig.2021.11.006.

[17] E. Bier, M.M. Harrison, K.M. O'connor-Giles, J. Wildonger, Advances in engineering the fly genome with the CRISPR-Cas system, Genetics. 208 (2018) 1–18. https://doi.org/10.1534/genetics.117.1113.

[18] J. Gokcezade, G. Sienski, P. Duchek, Efficient CRISPR/Cas9 plasmids for rapid and versatile genome editing in Drosophila, G3 Genes, Genomes, Genet. 4 (2014). https://doi.org/10.1534/g3.114.014126.

[19] R. Böttcher, M. Hollmann, K. Merk, V. Nitschko, C. Obermaier, J. Philippou-Massier, I. Wieland, U. Gaul, K. Förstemann, Efficient chromosomal gene modification with CRISPR/cas9 and PCR-based homologous recombination donors in cultured Drosophila cells, Nucleic Acids Res. 42 (2014). https://doi.org/10.1093/nar/gku289.

[20] J.H. Massey, N. Akiyama, T. Bien, K. Dreisewerd, P.J. Wittkopp, J.Y. Yew, A. Takahashi, Pleiotropic Effects of ebony and tan on Pigmentation and Cuticular Hydrocarbon Composition in Drosophila melanogaster, Front. Physiol. 10 (2019). https://doi.org/10.3389/fphys.2019.00518.

[21] N.S. Kane, M. Vora, K.J. Varre, R.W. Padgett, Efficient screening of CRISPR/Cas9-induced events in Drosophila using a Co-CRISPR strategy, G3 Genes, Genomes, Genet. 7 (2017). https://doi.org/10.1534/g3.116.036723.

[22] R.L. Brinster, H.Y. Chen, M.E. Trumbauer, M.K. Yagle, R.D. Palmiter, Factors affecting the efficiency of introducing foreign DNA into mice by microinjecting eggs, Proc. Natl. Acad. Sci. U. S. A. 82 (1985). https://doi.org/10.1073/pnas.82.13.4438.

[23] B. Ewen-Campen, N. Perrimon, ovoD Co-selection: A method for enriching CRISPR/ Cas9-edited alleles in drosophila, G3 Genes, Genomes, Genet. 8 (2018). https://doi.org/10.1534/g3.118.200498.

CHAPTER 4

GENERATION OF RED-FLUORESCENT TRIPARTITE MRUBY4 SYSTEM AS AN ALTERNATIVE PROTEIN-PROTEIN INTERACTION BIOSENSOR[5]

[3] Bui, K. C., and Kamiyama, D. *To be submitted to a peer-reviewed journal*.

4.1 ABSTRACT

The generation of split fluorescent proteins has enabled the development of versatile tools for studying protein-protein interactions in living cells. Here, we present the tripartite mRuby4 system, a red-colored split fluorescent protein, based on the structural framework of the tripartite GFP system. The mRuby4 protein, like GFP, is composed of an 11-β-strand barrel structure, and here, we split it into three separate fragments: mRuby4$_{1-9}$, mRuby4$_{10}$, and mRuby4$_{11}$. We characterized the complementation of the tripartite mRuby4 system in human 293T cells under various conditions of proximity between the split tags, and their fluorescent signal appears bright when the tags are within 10 nm (a biologically relevant distance between two interacting proteins). Inspired by this result, we fused the tripartite mRuby4 tags to FKBP and FRB protein molecules and assay the tripartite mRuby4 system as an interaction sensor. However, there was no red fluorescence detected upon the rapamycin-induced FKBP-FRB interaction. Our results suggest that the current iteration of the tripartite mRuby4 system is not sufficient for robust detection of protein-protein interactions but could be improved through further engineering efforts.

4.2 INTRODUCTION

Green fluorescent protein (GFP) has long been a cornerstone in the field of molecular biology, allowing researchers to visualize and track proteins in living cells with remarkable clarity [1–3]. With the advent of split fluorescent proteins, researchers can visualize protein-protein interactions within living cells [4–6]. Previous work has generated the tripartite GFP system, where superfolder GFP is split into three parts, resulting in two short (~20 a.a.) peptides GFP β-strand 10 (GFP$_{10}$) and GFP β-strand 11 (GFP$_{11}$), and a "detector fragment" GFP β-strands 1-9 (GFP$_{1-9}$) [7]. The short peptides GFP$_{10}$ and GFP$_{11}$ can each be tagged to one of the interacting partners. The individual

fragments by themselves do not have any fluorescent signal. However, upon protein-protein interaction, all three components: GFP_{1-9}, GFP_{10}, GFP_{11} can reconstitute into a functional GFP [7]. Using such small fragments to tag proteins can reduce aggregation and folding interference – factors that may impact protein interaction [7].

The tripartite GFP system is an attractive, modular approach for visualizing protein interactions or complexes in live cellular contexts. Despite this advancement, there are still limitations associated with the tripartite GFP system. One major limitation is its emission wavelength, which falls within the green spectrum. This poses challenges when studying multiple proteins simultaneously in single cells, as it can be difficult to distinguish between different fluorescent signals.

To address this limitation, a red-colored tripartite fluorescent protein system is needed. Red fluorescent proteins (RFPs) offer distinct advantages, such as longer emission wavelengths and reduced phototoxicity, making them ideal for multicolor imaging experiments. By developing a tripartite RFP system, researchers can overcome the limitations of traditional GFP and expand the possibilities for studying complex cellular processes in greater detail.

Our group's previous works have generated several spontaneously assembling split bipartite FPs ($FP_{1-10/11}$) by dividing between β-strand 10 and β-strand 11 of the FP and thereby creating β-strand 1-9 component and β-strand 11 (the epitope tag) [8,9]. From this engineering approach, we developed multiple color variants of this split bipartite FP system, which include $EBFP2_{1-10/11}$, $Capri_{1-10/11}$, and $mRuby4_{1-10/11}$ [9]. From the available colored split FPs, we chose the split bipartite mRuby4 system to generate a red-colored split tripartite FP system since its emission would be distinct from the green-color spectrum [10]. Moreover, it has been known that other red-colored FPs do not tolerate well a single long spacer insertion such as mKO2, mApple, mScarlet-

I, and sfCherry2, which show diminished fluorescence in the reconstituted FP compared to its full-length counterpart [8,9,11]. Tamura and colleagues have shown that the mRuby variant tolerates a single spacer insertion as its signal level is ~69% compared to its full-length counterpart, suggesting that the split mRuby4 has efficient self-complementation and retains some fluorescent signal after its "split" [9]. Thus, it is conceivable that (1) mRuby4 can better tolerate multiple spacer insertions compared to other red-colored FPs and (2) its tripartite components can reconstitute into a functional fluorescent protein. Inspired by this split bipartite system, here we further engineered and yielded a split tripartite mRuby4 system.

4.3 RESULTS

Proximity of fragments affects the reconstitution of tripartite mRuby4

Similar to the structure of full-length GFP, mRuby4 is composed of an 11-β-strand barrel [12]. To generate the red-colored tripartite system, we split mRuby4 into three fragments: mRuby4$_{1-9}$, mRuby4$_{10}$, and mRuby4$_{11}$, mirroring the split sites of the tripartite GFP system (**Figure 4.1**). To verify the *in vivo* complementation of these three fragments, we co-expressed all three fragments in 293T cells. The detector fragment, mRuby4$_{1-9}$, and short peptide fragment, mRuby4$_{10}$, were fused to C-terminal monomeric infrared fluorescent protein (mIFP) and membrane-anchoring CAAX sequence. The other short peptide fragment mRuby4$_{11}$ was either fused to the mIFP and CAAX sequence; or cytoplasmic FKBP12-rapamycin binding domain (FRB) (**Figure 4.2a-b**). When mRuby4$_{11}$ was fused to cytoplasmic FRB and co-expressed with membrane-anchored mRuby4$_{1-9}$ and mRuby4$_{10}$ fragments, there was no reconstituted signal from tripartite mRuby4, indicating that there is no spontaneous self-assembly when one of the fragments is localized in a different compartment of the cell (**Figure 4.2a**). However, when mRuby4$_{11}$ was fused to a membrane anchor and co-expressed with the membrane-anchored mRuby4$_{1-9}$ and mRuby4$_{10}$

fragments, we could detect reconstituted mRuby4 signal on the membrane, indicating that the tripartite fragments could self-complement when all fragments are localized in the same cellular compartment (**Figure 4.2b**).

To simulate a condition where two proteins interact with each other, we added a short (~11 a.a.) linker sequence between $mRuby4_{10}$ and $mRuby4_{11}$ components. It has been known that a protein-protein interaction can occur within molecular distances from 1-10 nm [13–15]. With this 11 a.a. linker, the two tripartite-FP-fusion protein molecules are expected to be ~5 nm apart [16]. When $mRuby4_{10-11}$ was fused to a membrane anchor and co-expressed with the membrane-anchored $mRuby4_{1-9}$, we could detect a reconstituted mRuby4 signal on the membrane (**Figure 4.2c**). Moreover, the signal intensity was greater than that of unlinked tripartite fragments, suggesting that this tripartite mRuby4 system may be able to detect a protein interaction (**Figure 4.2d-e**).

FKBP-FRB interaction as a benchmark for tripartite FP interaction sensor

To assess the ability of the tripartite mRuby4 system to detect a protein interaction, we use the well-documented, rapamycin-inducible interaction between rapamycin-binding domain of the mammalian target of rapamycin (mTOR) kinase (FRB) and FK506-binding protein 12 (FKBP) [17]. Previously, Cabantous and colleagues used the FRB/FKBP interaction as a benchmark for tripartite GFP interaction reporter [7]. In our hands, we wanted to visually assess the dynamics of this interaction within human 293T cells by using time-lapse imaging. We fused (1) the N-terminal Lyn11 membrane-anchoring sequence and two tandem FKBP to the GFP_{10} fragment, (2) the N-terminal FRB to the GFP_{11} fragment, and (3) the GFP_{1-9} detector fragment was fused to the C-terminal monomeric infrared fluorescent protein (mIFP) and membrane-anchoring CAAX

sequence (**See 4.7 Methods**). When both GFP_{10} and GFP_{11} fusions are co-expressed alongside the membrane-anchored GFP_{1-9}, near-blank levels of fluorescent signal are observed (**Supplementary Figure 4.1 and 4.2a**). However, upon the addition of 200 nM of rapamycin, a rapid increase in fluorescence on the cell membrane is detected, likely due to the reconstitution of all tripartite GFP fusion components, suggesting an interaction between FKBP-GFP_{10} and FRB-GFP_{11} fusion proteins (**Supplementary Figure 4.1 and 4.2a**). After 40 minutes of rapamycin incubation, a two-fold change in green fluorescence is detected, and at 90 minutes of rapamycin incubation, a plateau in the maximum green fluorescent signal begins to occur (**Supplementary Figure 4.2b**). Upon validating this benchmark for tripartite GFP reconstitution, we based our parameters from this assay to test our tripartite mRuby4 interaction sensor.

Tripartite mRuby4 does not reconstitute upon FKBP-FRB interaction

Similarly, to test our tripartite mRuby4 interaction reporter, we fused (1) N-terminal Lyn11 membrane-anchoring sequence and two tandem FKBP to the $mRuby4_{10}$ fragment, (2) N-terminal FRB to $mRuby4_{11}$ fragment, and (3) $mRuby4_{1-9}$ detector fragment was fused to C-terminal monomeric infrared fluorescent protein (mIFP) and membrane-anchoring CAAX sequence (**Figure 4.3a**). We co-transfected all three constructs in 293T cells. One hour before imaging, we added 200 nM of rapamycin in order to easily detect any fluorescence. However, we unexpectedly could not detect any fluorescent signal on the membrane, as we would expect the reconstitution of tripartite mRuby4 components upon FKBP-FRB interaction.

Because we previously tested the FKBP-FRB rapamycin-inducible interaction using the tripartite GFP fusion constructs, we ruled out the possibility of the absence of FKBP-FRB interaction upon rapamycin addition. One possibility is that the Lyn11::FKBP::FKBP::$mRuby4_{10}$

localizes to a different sub-compartment of the membrane compared to mRuby4$_{1-9}$::mIFP::CAAX due to the different membrane-anchoring sequences. To rule out this explanation, we deleted the Lyn11 sequence and added the C-terminal CAAX sequence to the mRuby4$_{10}$ fragment (**Supplementary Figure 4.3a**). Upon co-expressing all tripartite components and adding rapamycin, we still could not detect any fluorescent signal (**Supplementary Figure 4.3b**).

Another possibility is that fusion to the two bulky, tandem FKBP protein molecules prevents tripartite mRuby4 reconstitution. To test this, we use the mRuby4$_{11}$ fragment fused to C-terminal monomeric infrared fluorescent protein (mIFP) and membrane-anchoring CAAX sequence (**Supplementary Figure 4.3c**). Upon co-expressing all tripartite components, we could detect a faint fluorescent signal on the membrane, suggesting that tripartite mRuby4 can self-assemble into a functional protein (**Supplementary Figure 4.3d**). While mRuby4$_{10}$ fusion protein, co-expressed with the other tripartite fragments, does not prevent tripartite mRuby4 reconstitution, (1) we speculate that mRuby4$_{10}$ fragment fused to the bulky FKBP could hinder the complementation efficiency of the tripartite system to some degree due to the weak fluorescent signal observed and (2) it does not fully rule out the possibility that FRB- mRuby4$_{11}$ fusion may be misfolded, hindering or preventing tripartite mRuby4 complementation – which we did not test in this study.

Another possibility is that rapamycin itself affects tripartite mRuby4 reconstitution – to which we co-expressed all tripartite fragments (all individually fused to C-terminal mIFP and CAAX sequence) (**Supplementary Figure 4.4a**). We show that upon the addition of rapamycin, we can detect the reconstituted fluorescent signal on the membrane, indicating that rapamycin does not prevent the association of the tripartite fragments (**Supplementary Figure 4.4b**). With these results taken altogether, this current iteration of the tripartite mRuby4 system is not sufficient for

robust detection of protein-protein interactions. However, with further engineering, this system may be improved to be an alternative red-colored biosensor for protein interaction (**see 4.4 Discussion**).

Mutagenesis-based approach to improve tripartite mRuby4 complementation efficiency

While we have shown that tripartite mRuby4 can self-assemble into a functional fluorescent protein, our results also indicate that when the $mRuby4_{10}$ and $mRuby4_{11}$ fragments are fused to individual interacting proteins, the tripartite mRuby4 components cannot associate and reconstitute into a functional fluorescent protein. Moreover, the reconstituted signal from the tripartite mRuby4 system is weak compared to those of the bipartite and full-length variants (**Supplementary Figure 4.5a-d**). This limitation highlights the need to further enhance the design of the tripartite mRuby4 system for use in protein interaction studies.

To address this limitation, future research could focus on introducing mutations into the $mRuby4_{1\text{-}9}$ component of tripartite mRuby4. Previously, Cabantous and colleagues showed that introducing mutations into $GFP_{1\text{-}9}$ greatly improved solubility and complementation of the tripartite GFP system expressed in *E. coli* [7]. Here, we utilize a mutagenesis-based approach and introduce random mutations into the $mRuby4_{1\text{-}9}$ fragment during error-prone PCR, and show preliminary data for improved complementation efficiency of the tripartite mRuby4 (**Figure 4.4a**). Then, we clone the mutagenized $mRuby4_{1\text{-}9}$ sequence into a tripartite mRuby4 simulation construct which contains long (30 a.a.) linkers between each tripartite component, hereby referred to as $mRuby_{1\text{-}9\text{-}longlinker\text{-}10\text{-}longlinker\text{-}11}$ (**Figure 4.4a**). The original $mRuby4_{1\text{-}9\text{-}longlinker\text{-}10\text{-}longlinker\text{-}11}$ construct (containing no mutations) was expressed from an isopropyl β-D-1-thiogalactopyranoside (IPTG) inducible pET vector and showed that the *E. coli* have weak, detectable red fluorescence after 24h

of IPTG induction (**Figure 4.4b**). We look at the fluorescence at different time points after IPTG induction in a negative control (full-length Clover) and a positive control (the bipartite simulation construct: $mRuby_{1\text{-}9\text{-}longlinker\text{-}10\text{-}11}$), where the positive control shows detectable red fluorescence even at 0h after IPTG induction (**Figure 4.4b**).

The bipartite simulation shows robust reconstitution, as we have observed similarly in transfected 293T cells (**Figure 4.2c**). As we predicted earlier, mRuby4 tolerates a single linker insertion well. We looked at the fluorescent signals of two bipartite mRuby4 simulation constructs – where long (30 a.a.) linker insertion was placed between β strand 9 and β strand 10 ($mRuby_{1\text{-}9\text{-}longlinker\text{-}10\text{-}11}$); or β strand 10 and β strand 11 ($mRuby_{1\text{-}10\text{-}longlinker\text{-}11}$) (**Supplementary Figure 4.6a**). We detected a bright fluorescent signal 24h after IPTG induction in both bipartite mRuby4 simulation conditions (**Supplementary Figure 4.6b**). We see at least two-fold fluorescence intensities from both bipartite mRuby4 simulation constructs at 16h after IPTG induction (**Supplementary Figure 4.6c**). Based on the fluorescent signal from the bipartite mRuby4 simulation construct, we would expect the rounds of mutagenesis in $mRuby_{1\text{-}9}$ to improve the complementation efficiency and fluorescent signal from the tripartite mRuby4 simulation construct.

From the first round of mutagenesis, when the tripartite mRuby4 simulation construct (containing mutagenized $mRuby4_{1\text{-}9}$ sequence) was expressed, we screened through 900 different colonies. Of these colonies, we observed two colonies that had detectable, bright fluorescent signal 8h after IPTG induction, suggesting that these colonies may be expressing a mutagenized $mRuby4_{1\text{-}9\text{-}longlinker\text{-}10\text{-}longlinker\text{-}11}$ construct which had an efficient tripartite mRuby4 reconstitution (**Figure 4.4c**).

4.4 DISCUSSION

Improving tripartite mRuby4 performance

The preliminary data from the first round of mutagenesis of the tripartite mRuby4 simulation construct demonstrates that targeted mutations in the complementary fragments of mRuby4 can significantly enhance its complementation efficiency. This suggests that further rounds of mutagenesis may improve the complementation efficiency of the tripartite mRuby4 system. Previous bioengineering works have shown that at least three rounds of mutagenesis are sufficient to have an improved complementation efficiency of a split fluorescent protein [6,7,9]. To this end, we outline a mutagenesis-based approach where we would introduce mutations into the larger $mRuby4_{1\text{-}9}$ sequence (**Figure 4.4d**). By systematically screening colonies expressing mutagenized $mRuby4_{1\text{-}9\text{-}longlinker\text{-}10\text{-}longlinker\text{-}11}$ in *E. coli*, we can rapidly identify variants that may exhibit improved association and reconstitution of the tripartite mRuby4 system. We can further validate these results by testing the tripartite mRuby4 complementation within 293T cells.

One of the key challenges in designing split fluorescent protein systems is ensuring that the fused protein fragments remain soluble and capable of reconstituting into a functional fluorescent protein upon complementation. One explanation for the negative results observed in the FKBP-FRB assay is that one or more of the fused proteins are insoluble and inaccessible and may not associate with their tripartite partners [18,19]. Our mutagenesis-based strategy may also enhance the solubility of fused protein fragments, such as the introduction of stabilizing mutations or mutations that promote proper protein folding.

In conclusion, the tripartite mRuby4 system is a promising red-colored split FP system that could act as an interaction biosensor using short fragment tags. The mutagenesis-based approach described in this study is one proposed avenue for improving the performance of the tripartite

mRuby4 system for studying protein-protein interactions. By further optimizing the design of tripartite mRuby4 and addressing challenges related to split protein complementation, researchers can expand the utility of split fluorescent protein systems for a wide range of biological applications.

4.5 FIGURES

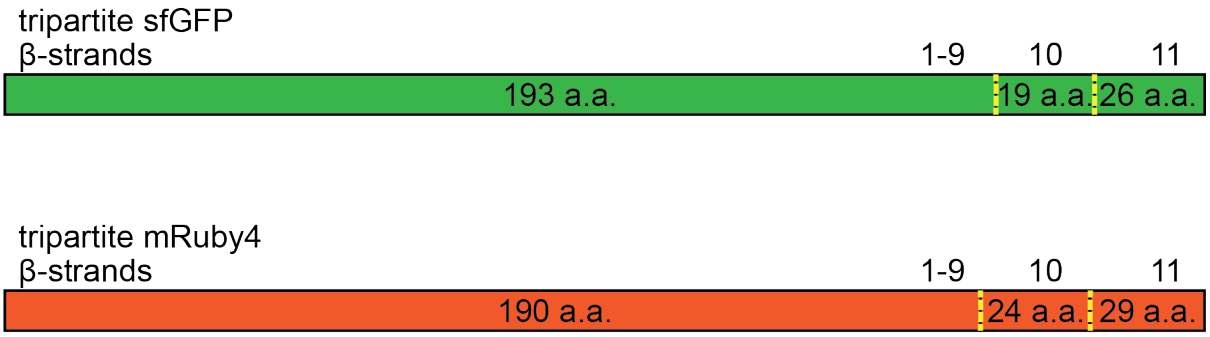

Figure 4.1 | Design of tripartite mRuby4 system mRuby4 (orange) is split (dashed yellow lines) into the tripartite components: mRuby4$_{1\text{-}9}$ (β-strand 1–9), mRuby4$_{10}$ (β-strand 10), and mRuby4$_{11}$ (β-strand 11). The design of the tripartite mRuby4 system is based on the known split points from tripartite sfGFP (green) [7]. The amino acid (a.a.) lengths of tripartite mRuby4 components parallels those of the tripartite sfGFP.

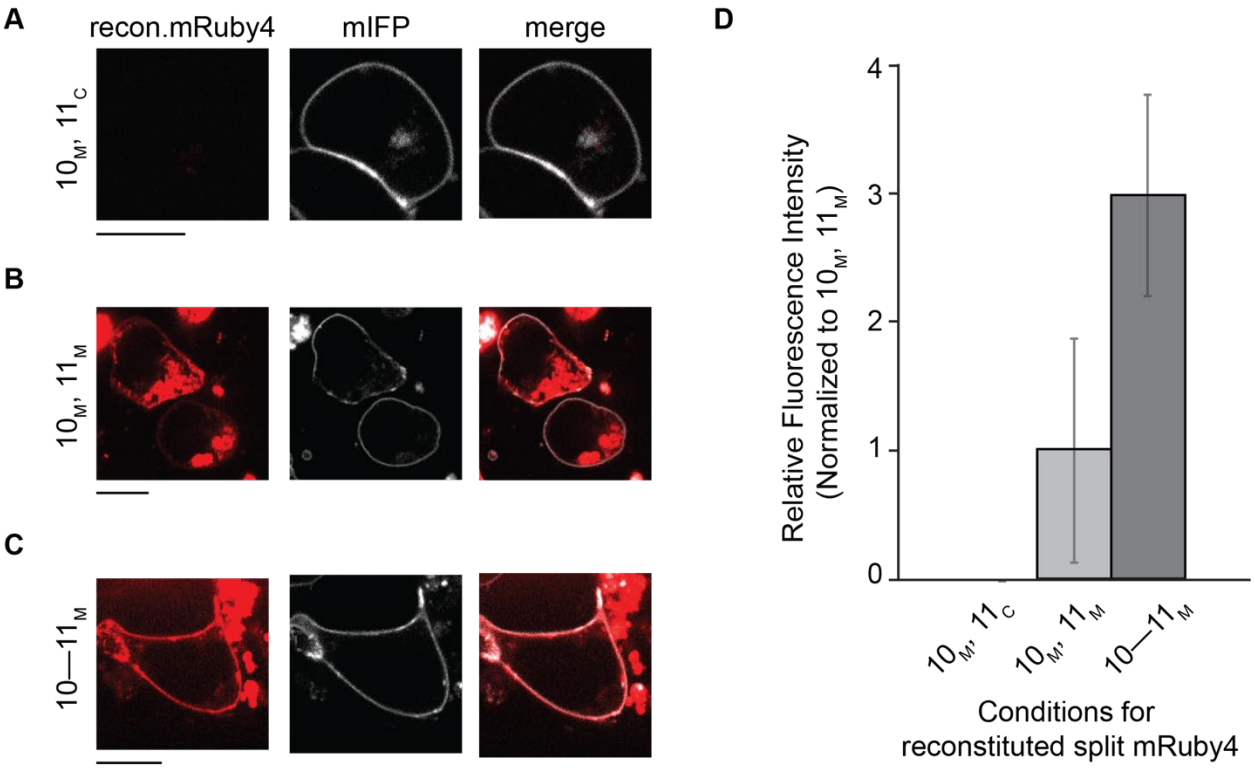
A
recon.mRuby4
mIFP
merge
10M, 11C
B
10M, 11M
C
10—11M
D
Relative Fluorescence Intensity
(Normalized to 10M, 11M)
4
3
2
1
0
10M, 11C
10M, 11M
10—11M
Conditions for
reconstituted split mRuby4

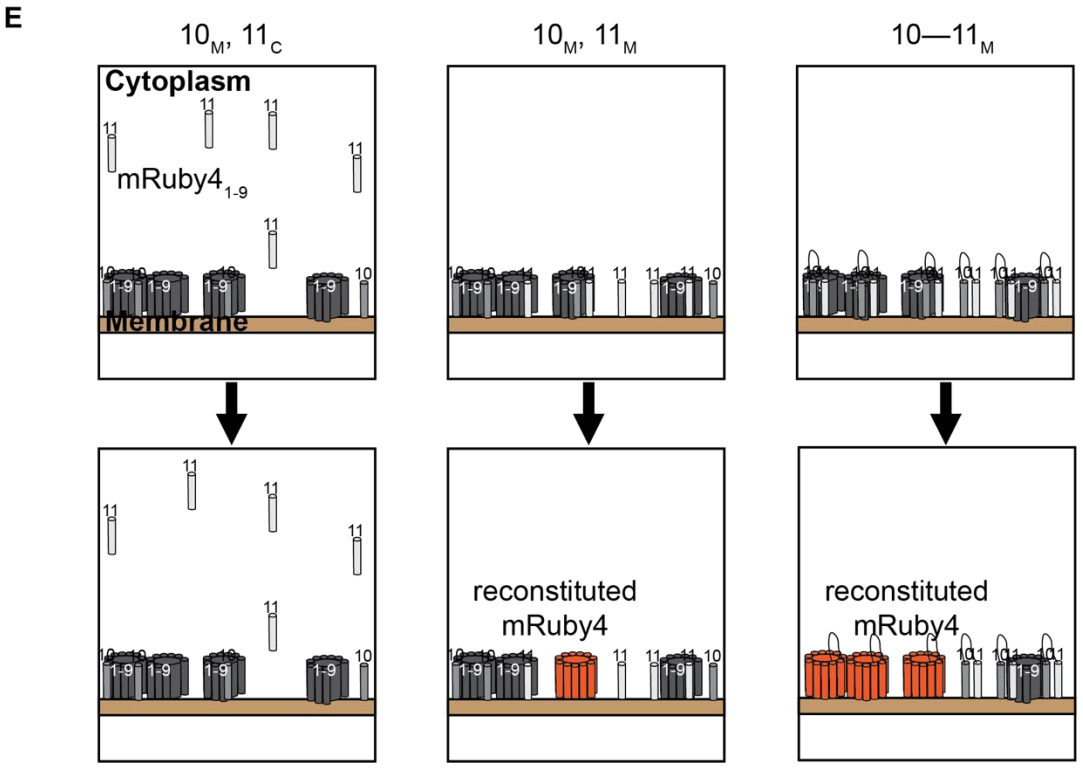
E
10M, 11C
10M, 11M
10—11M
Cytoplasm
mRuby4 1-9
Membrane
reconstituted
mRuby4
reconstituted
mRuby4

Figure 4.2 | Reconstitution of tripartite mRuby4 components depends on proximity of mRuby4$_{10}$ and mRuby4$_{11}$ (**a**) When mRuby4$_{11}$ is free-floating in the cytoplasm and mRuby4$_{10}$ is bound to the membrane due to the C-terminal CAAX motif (10_M, 11_C), there is no tripartite mRuby4 reconstitution – where mRuby4$_{1\text{-}9}$ is free-floating in the cytoplasm. Monomeric infrared fluorescent protein (mIFP) serves as a transfection marker for all subsequent experiments in this paper. When mRuby4$_{10}$ and mRuby4$_{11}$ fragments are (**b**) both bound to the membrane due to the C-terminal CAAX motif (10_M, 11_M), and (**c**) bound together with an 11 a.a. chain (10_M–11_M), there is split mRuby4 reconstitution (red) – where mRuby4$_{1\text{-}9}$ is bound to the membrane. (**d**) Quantification of fluorescence intensity from tripartite mRuby4 reconstitution in each condition. (**e**) Cartoon schematic of tripartite mRuby4 reconstitution (orange barrel) in each condition. When mRuby4$_{11}$ (light gray cylinder) is in the cytoplasm, there is no spontaneous reconstitution with mRuby4$_{10}$ (dark gray cylinder) and mRuby4$_{1\text{-}9}$ (dark gray barrel) on the membrane (left column). There is spontaneous reconstitution when mRuby4$_{10}$ and mRuby4$_{11}$ are both expressed individually on the membrane (middle column) or physically linked together (right column) – when mRuby4$_{1\text{-}9}$ is present in the cell. Scale bar, 10 μm in (**a-c**).

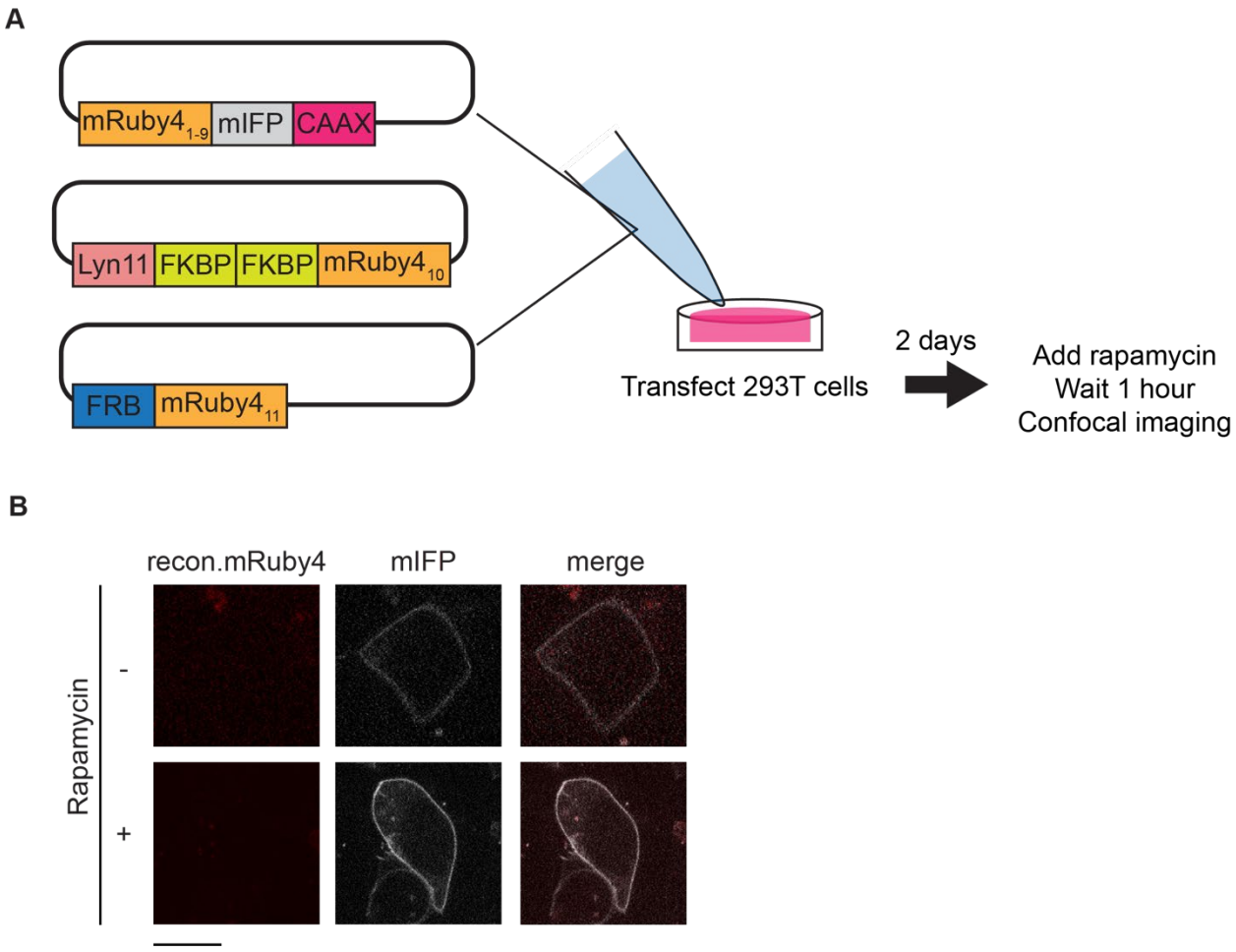

Figure 4.3 | Reconstitution of tripartite mRuby4 components does not occur upon FKBP and FRB protein interaction on the membrane (**a**) Cartoon schematic of transfection and imaging experiment. A mix of plasmid constructs was transfected into human 293T cells. mRuby4$_{1-9}$ construct contains the C-terminal mIFP (gray) transfection marker and membrane-anchor CAAX motif (dark pink). mRuby4$_{10}$ construct contains the N-terminal membrane-anchor Lyn11 sequence (lime green) and two tandem sequences of FKBP (salmon pink). mRuby4$_{10}$ construct contains the N-terminal membrane-anchor Lyn11 sequence (lime green) and two tandem sequences of FKBP (salmon pink). mRuby4$_{11}$ construct contains an N-terminal sequence of FRB (blue). For more details of the experiments performed, see **4.7 Methods**. (**b**) Upon the

addition of rapamycin, the FKBP-FRB interaction is induced on the membrane in transfected cells. Without rapamycin, no FKBP-FRB interaction occurs (top row). However, upon FKBP-FRB interaction, there is no tripartite mRuby4 reconstitution on the membrane, showing a false negative readout (bottom row). Scale bar, 10 μm.

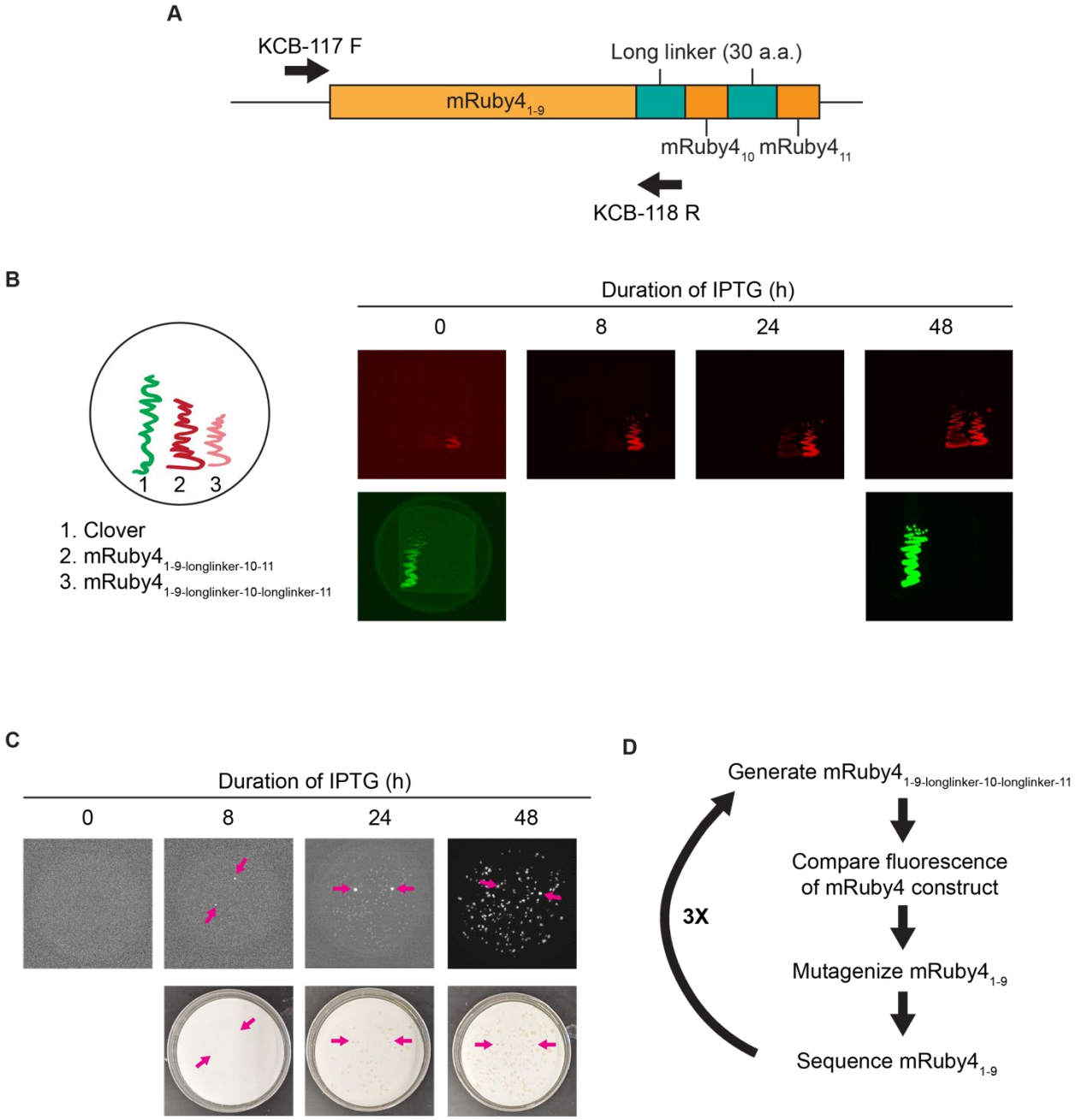

Figure 4.4 | Mutagenesis of mRuby4$_{1-9}$ in *E. coli* for improving complementation efficiency of tripartite mRuby4 system (**a**) Cartoon schematic of mRuby4$_{1-9-longlinker-10-longlinker-11}$ for mutagenesis. Two spacer sequences (to generate a 30 a.a. linker) (teal) were inserted between mRuby4$_{1-9}$ and mRuby4$_{10}$ sequences; and mRuby4$_{10}$ and mRuby4$_{11}$ sequences. Mutations were introduced into mRuby4$_{1-9}$ during error-prone PCR, using primer set KCB-117 and KCB-118.

(**b**) Fluorescence intensity, upon IPTG induction, of *E. coli.* expressing Clover (negative control), mRuby4$_{1\text{-}9\text{-}longlinker\text{-}10\text{-}11}$ (positive control), and mRuby4$_{1\text{-}9\text{-}longlinker\text{-}10\text{-}longlinker\text{-}11}$ from 0-48h. The cartoon schematic is shown on the left. Time-lapse of fluorescence intensity is shown on the right. (**c**) *E. coli.* colonies expressing mRuby4$_{1\text{-}9\text{-}longlinker\text{-}10\text{-}longlinker\text{-}11}$ upon the first round of mutagenesis in the mRuby4$_{1\text{-}9}$ component from 0-48h after IPTG induction. Pink arrows denote colonies with red fluorescence detected 8 hours after IPTG induction. (**d**) Mutagenesis-based approach for optimizing complementation efficiency of mRuby4$_{1\text{-}9\text{-}longlinker\text{-}10\text{-}longlinker\text{-}11}$.

4.6 SUPPLEMENTARY FIGURES

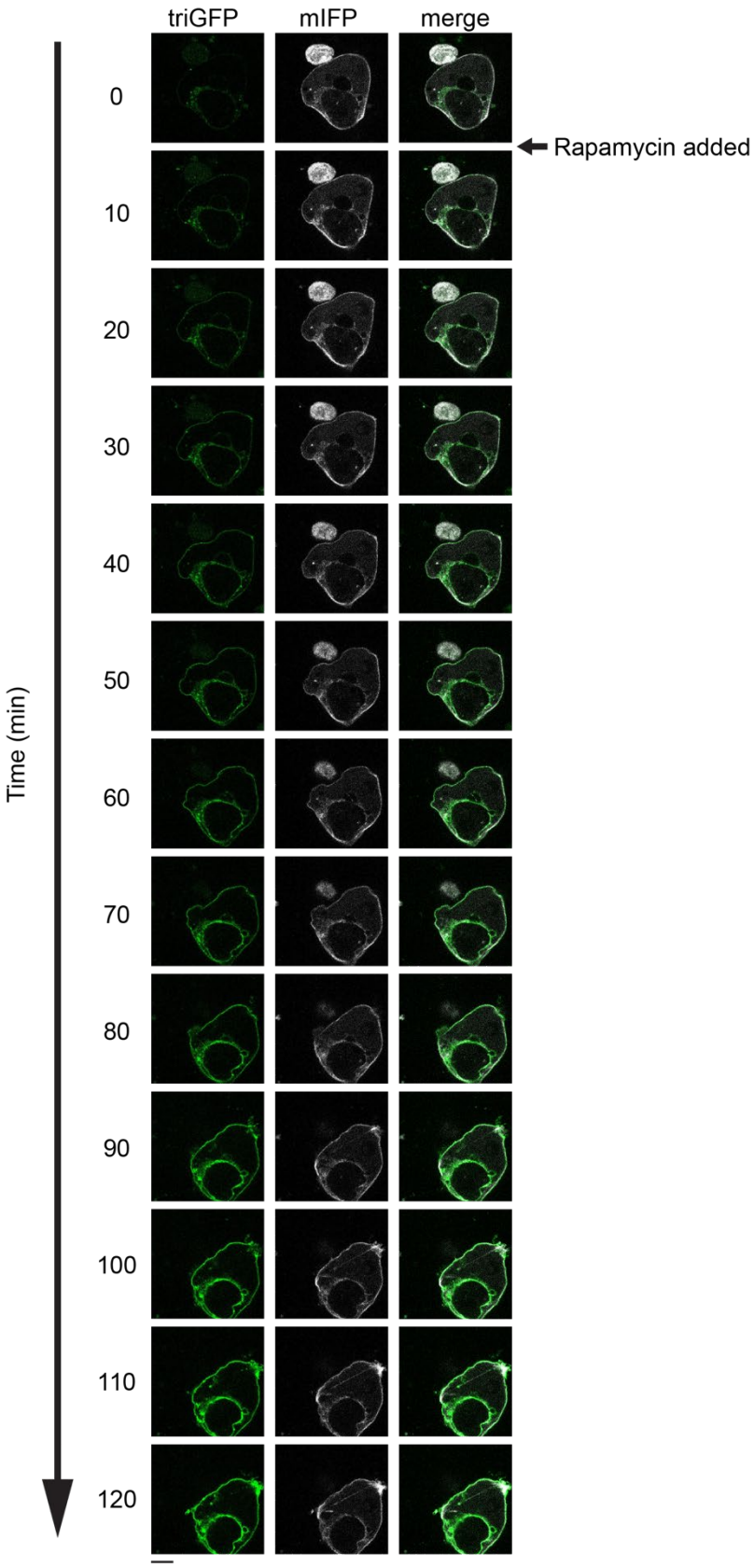

Supplementary Figure 4.1 | Time-lapse imaging of triGFP reconstitution upon FKBP-FRB interaction on the membrane (**a**) Time-lapse series imaged from 0-120 min of tripartite GFP reconstitution upon inducing the FKBP-FRB interaction within a single 293T cell. Three constructs are expressed in this cell: Lyn11::FKBP::FKBP::GFP_{10}, FRB::GFP_{11}, and GFP_{1-9}::mIFP::CAAX. Upon the addition of rapamycin (black arrow) at 5 minutes, the green fluorescent signal on the membrane is detected. One frame is taken every 10 minutes. Scale bar, 10 μm.

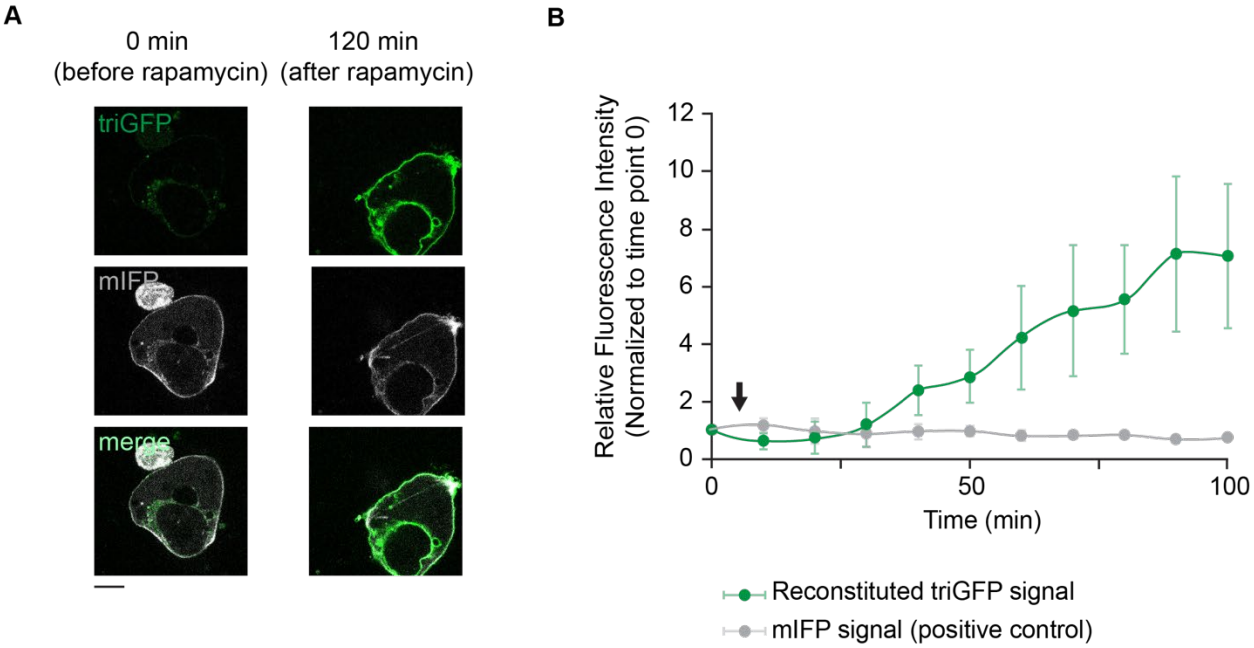

Supplementary Figure 4.2 | Quantification of fluorescence intensity from reconstituted triGFP after rapamycin addition (**a**) Confocal images of the green fluorescent signals at time points 0 and 120 minutes. Rapamycin, which induces FKBP-FRB interaction, was added at 5 minutes. Scale bar, 10 μm. (**b**) Quantification of the fluorescent signals detected across time (min) during the time-lapse imaging series. Green indicates the fluorescent signals from reconstituted tripartite GFP. Gray indicates the fluorescent signals from mIFP. The black arrow indicates the addition of rapamycin. Error bars, STD.

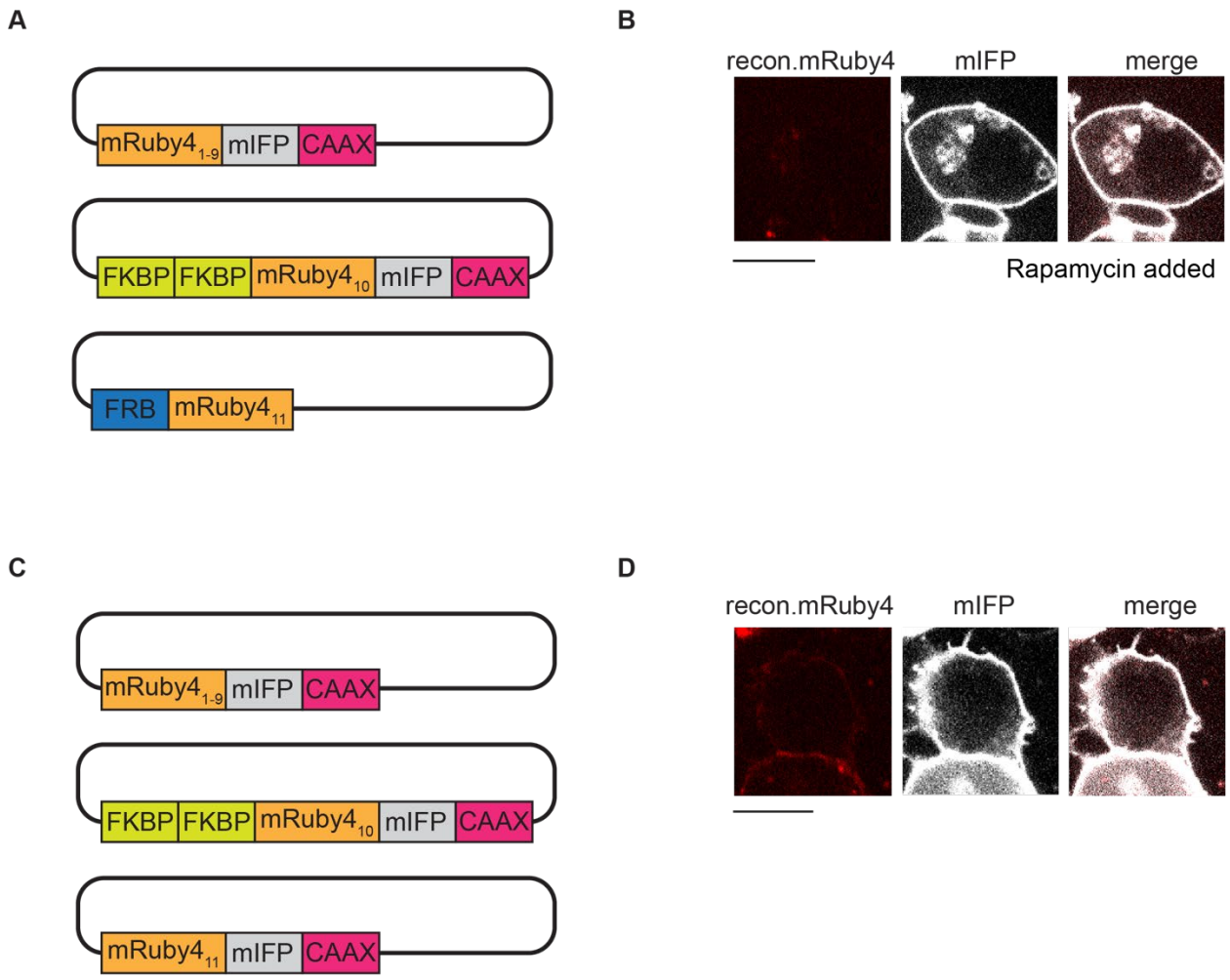

Supplementary Figure 4.3 | Membrane-anchors, not membrane FKBP-FRB protein interaction, permits tripartite mRuby4 reconstitution (**a, c**) Cartoon schematic of the mix of constructs co-expressed in (**b, d**) transfected cells. (**a**) FKBP::FKBP::mRuby10 is membrane-anchored using the CAAX sequence instead of the Lyn11 sequence (that was used in **Figure 4.3a**). (**b**) No red fluorescent signal is detected when FKBP-FRB interaction is induced. This cell expressed the constructs from (**a**). (**c**) All tripartite components are fused to mIFP::CAAX. All of their protein molecules should localize similarly on the cell membrane. Note that the FRB sequence is deleted in the mRuby4$_{11}$ fusion construct. (d) A weak red fluorescent signal is detected. This cell expressed the constructs from (**b**). Scale bar, 10 μm in (**c-d**).

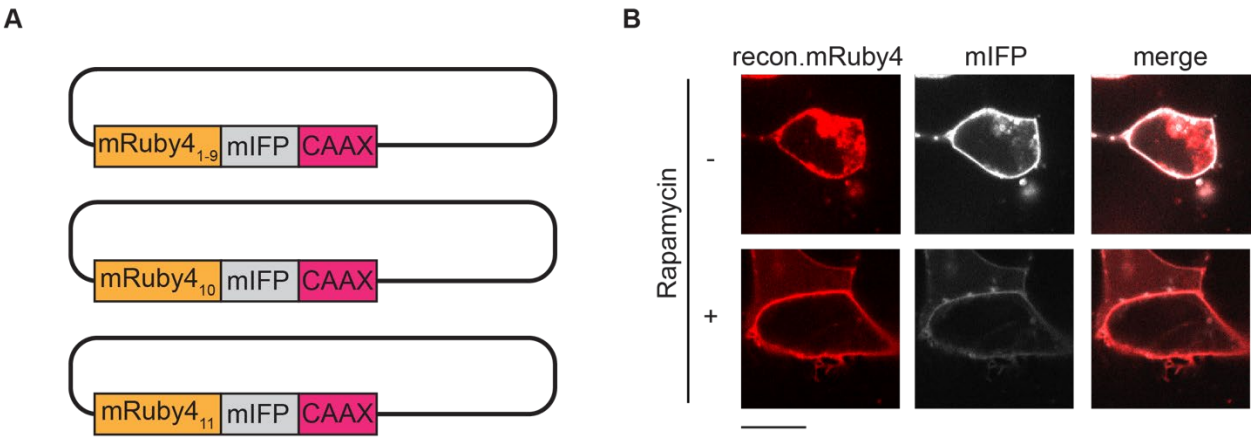

Supplementary Figure 4.4 | Rapamycin does not prevent tripartite mRuby4 reconstitution

(**a**) Cartoon schematic of the mix of constructs co-expressed in (**b**). (**b**) A red fluorescent signal is detected on the membrane. The addition of rapamycin does not prevent the self-assembly of tripartite mRuby4 components (bottom row). Scale bar, 10 μm.

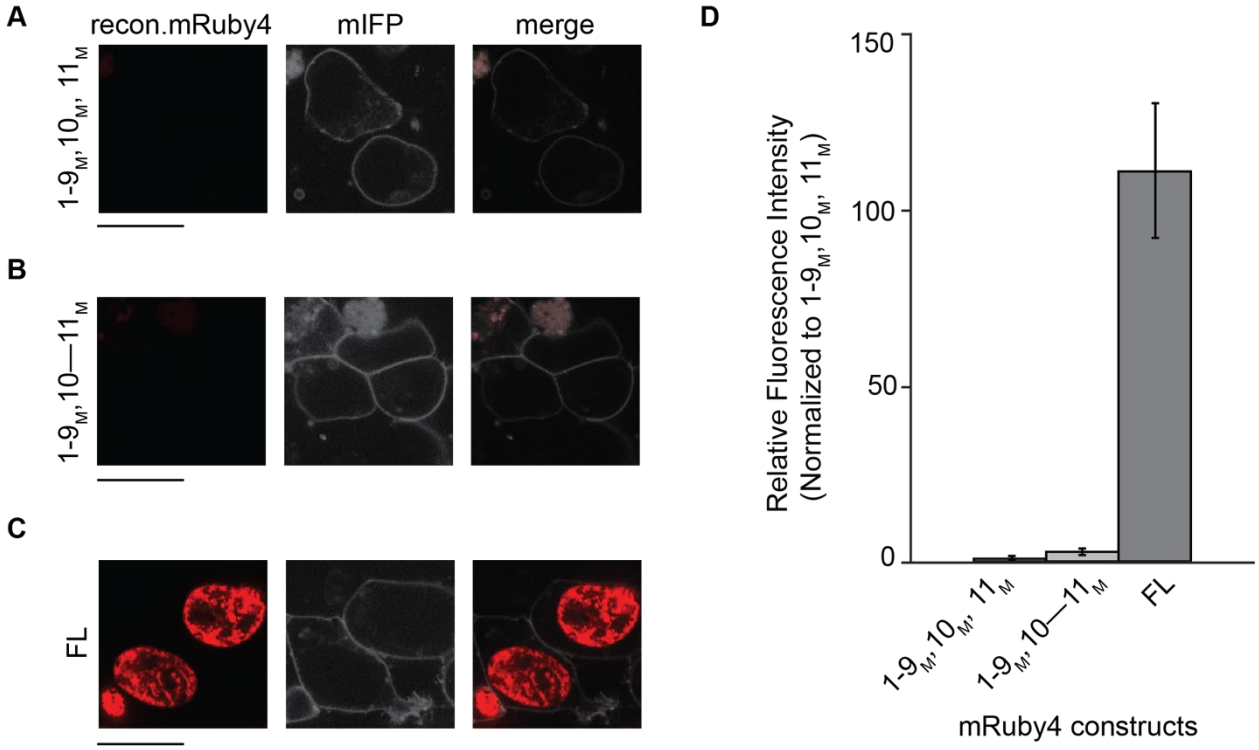

Supplementary Figure 4.5 | Brightness of tripartite mRuby4 reconstitution can be improved (**a-b**) Confocal images of split mRuby4 reconstitution. Co-expressed with membrane-anchored mRuby4$_{1\text{-}9}$ fragment, when mRuby4$_{10}$ and mRuby4$_{11}$ fragments are (**a**) individually bound to the membrane due to the C-terminal CAAX motif (1-9$_M$, 10$_M$, 11$_M$) or (**b**) bound with each other using an 11 a.a. linker chain (1-9$_M$, 10$_M$–11$_M$), there is split mRuby4 reconstitution (red). The fluorescent signals detected from split mRuby4 are weak. (**c**) Confocal images of full-length mRuby3 fused to H2B, a histone-localized protein. The fluorescent signal detected from the full-length variant is bright. (**d**) Quantification of relative red fluorescence intensity from the mRuby variants.

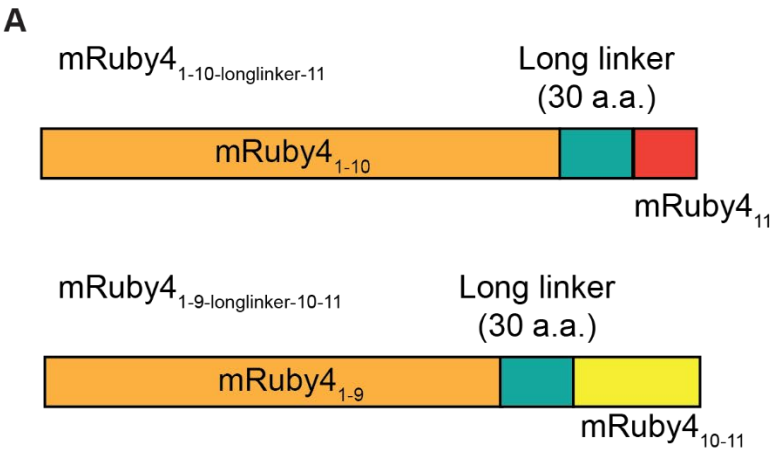

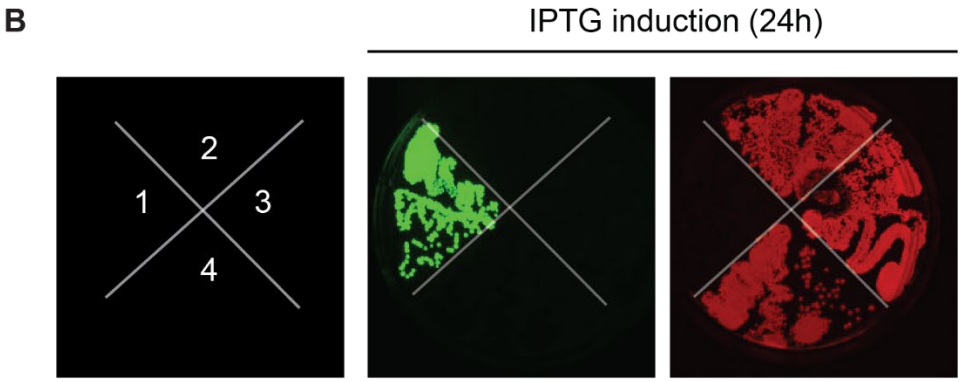

1. Clover
2. mRuby4 1-9-longlinker-10-11
3. mRuby4 1-10-longlinker-11
4. FL mRuby4

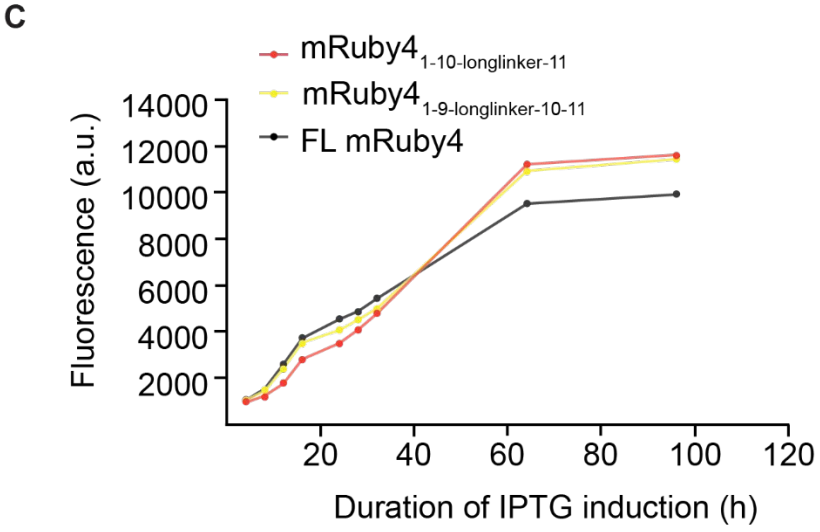

Supplementary Figure 4.6 | Single-spacer insertion into mRuby4 has bright fluorescent signal (**a**) Cartoon schematic of the two variations of single-spacer-inserted-mRuby4. A single spacer (30 a.a. chain) is either inserted between $mRuby4_{10}$ and $mRuby4_{11}$ – this construct is denoted as $mRuby4_{1\text{-}10\text{-}longlinker\text{-}11}$ (top); or inserted between $mRuby4_{9}$ and $mRuby4_{10}$ – this construct is denoted as $mRuby4_{1\text{-}9\text{-}longlinker\text{-}10\text{-}11}$ (bottom). (**b**) Fluorescent signals detected, after 24 hours of IPTG induction, from E. coli expressing various constructs: Clover, $mRuby4_{1\text{-}10\text{-}longlinker\text{-}11}$, $mRuby4_{1\text{-}9\text{-}longlinker\text{-}10\text{-}11}$, or full-length mRuby4. Red fluorescent signals appear bright in colonies expressing any of the mRuby4 variants. (**c**) Quantification of fluorescence intensities from colonies expressing $mRuby4_{1\text{-}10\text{-}longlinker\text{-}11}$, $mRuby4_{1\text{-}9\text{-}longlinker\text{-}10\text{-}11}$, or full-length mRuby4 across time (hours) after IPTG induction.

4.7 SUPPLEMENTARY TABLES

Supplementary Table 4.1 | Nucleotide sequences of mRuby4$_{1-9}$, mRuby4$_{10-11}$, mRuby4$_{10}$, mRuby4$_{11}$

mRuby4$_{1-9}$	ATGGTGTCTAAGGGCGAAGAGCTGATCAAGGAAAATATGCGTACGAA GGTGGTCATGGAAGGTTCGGTCAACGGCCACCATTTCAAATGCA TAGGTGAAGGAGAAGGCAGACCGTACGAGGGAGTGCAAACCAT GAGGATCAAAGTCATCGAGGGAGGACCCCTGCCATTTGCCTTTG ACATTCTTGCCACGTCGTTCATGTATGGCAGCCGTACCTTTATCA AGTACCCGGCCGACATCCCTGATTTCTTTAAACAGTCCTTTCCTG AGGGTTTTACTTGGGAAAGAGTTACGAGATACGAAGATGGTGG AGTCATCACCGTCACGCAGGACACCTGCCTTGAGGATGGCGAG CTCGTCTACAACGTCAAGGTCAGCGGGGTAAACTTTCCCTCCAA TGGTCCCGTGATGCAGAAGAAGACCAAGGGTTGGGAGCCTAAT ACAGAGATGATGTATCCAGTAGATGGTGGTCTGAGAGGATACA CTGACATCGCACTGAAAGTTGATGGTGGTGGCCATCTGCACTGC AACTTCGTGACAACTTACAGGTCAAAAAAGACCGTC
mRuby4$_{10-11}$	ATGGTCCATGCCGTTGATCACCGCCTGGAAAGGATCGAGGAGAGTGAC AATGAAACCTACGTAGTGCAAAGAGAAGTGGCAGTTGCCAAATACAG CAACCTTGGTGGTGGCATGGACGAGCTGTACAAGACCGGT
mRuby4$_{10}$	ATGGGGAACATCAAGATGCCCGGTGTCCATGCCGTTGATCACCGCCTG GAAAGGATCGAGGAGAGTGACAATGAA
mRuby4$_{11}$	ATGGGGAACACCTACGTAGTGCAAAGAGAAGTGGCAGTTGCCAAATA CAGCAACCTTGGTGGTGGCATGGACGAGCTGTACAAGACCGGT

Supplementary Table 4.2 | Amino acid sequences of tripartite mRuby4 tags

mRuby4$_{10}$	GNIKMPGVHAVDHRLERIEESDNE
mRuby4$_{11}$	GNTYVVQREVAVAKYSNLGGGMDELYKTG

Supplementary Table 4.3 | List of primers used in this study

Split tripartite tag

FKBP-GFP(10)_inversePCR

- **Forward Primer:** GACCATCCTGCTGAAGGACCTGAACGGCGGCAGCCACATGGACTCTAGATCATAATCAGCCATACCACATTTGTAGAGGTTTTACTTGC
- **Reverse Primer:** TGGGTGCTCAGGTAGTGGTTGTCGGGCAGGTCCATGGTGTAGCGGCCGCTGGTGGCGAC

FKBP-mRuby4(10)_inversePCR

- **Forward Primer:** CGCCTGGAAAGGATCGAGGAGAGTGACAATGAAGACTCTAGATCATAATCAGCCATACCACATTTGTAGAGGTTTTACTTGC
- **Reverse Primer:** GTGATCAACGGCATGGACACCGGGCATCTTGATGCGGCCGCTGGTGGCGAC

GFP(11)-FRB_inversePCR

- **Forward Primer:** GTACGTGACCGCCGCCGGCATCACCGACGCCAGCTAGGCTACCGGTCGCCACCTC
- **Reverse Primer:** TCCAGCAGCACCATGTGGTCCCTCTTCTCGCTGGTGCTCATGCTAGCGGATCTGACGG

mRuby4(11)-FRB_inversePCR

- **Forward Primer:** CAACCTTGGTGGTGGCATGGACGAGCTGTACAAGACCGGTTCCGGACTCAGATCTCGA
- **Reverse Primer:** CTGTATTTGGCAACTGCCACTTCTCTTTGCACTACGTAGGTCATGCTAGCGGATCTGAC

Mutagenesis_mRuby4(1-9)

- **Forward Primer:** GATCCGAGCTCGACCGAATTC

- **Reverse Primer:** CAGCCAAGCTGCAGATCT

Supplementary Table 4.4 | Amino acid sequences of mRuby4$_{1\text{-}9\text{-}longlinker\text{-}10\text{-}11}$, mRuby41$_{\text{-}9\text{-}longlinker\text{-}10\text{-}longlinker\text{-}11}$, and mutagenized mRuby4$_{1\text{-}9}$ constructs

mRuby4$_{1\text{-}9\text{-}longlinker\text{-}10\text{-}11}$	MVSKGEELIKENMRTKVVMEGSVNGHHFKCIGEGEGRPYEGVQTMRIKV IEGGPLPFAFDILATSFMYGSRTFIKYPADIPDFFKQSFPEGFTWERVTRY EDGGVITVTQDTCLEDGELVYNVKVSGVNFPSNGPVMQKKTKGWEPNTE MMYPVDGGLRGYTDIALKVDGGGHLHCNFVTTYRSKKTVEF**GGGGSEG GGSGGPGSGGEGSAGGGSAGGGS**GNIKMPGVHAVDHRLERIEESDNET YVVQREVAVAKYSNLGGGMDELYK
mRuby41$_{\text{-}9\text{-}longlinker\text{-}10\text{-}longlinker\text{-}11}$	MVSKGEELIKENMRTKVVMEGSVNGHHFKCIGEGEGRPYEGVQTMRIKV IEGGPLPFAFDILATSFMYGSRTFIKYPADIPDFFKQSFPEGFTWERVTRYE DGGVITVTQDTCLEDGELVYNVKVSGVNFPSNGPVMQKKTKGWEPNTE MMYPVDGGLRGYTDIALKVDGGGHLHCNFVTTYRSKKTVEF**GGGGSEG GGSGGPGSGGEGSAGGGSAGGGS**GNIKMPGVHAVDHRLERIEESDN**GG GGSEGGGSGGPGSGGEGSAGGGSAGGGS**ETYVVQREVAVAKYSNLGG GMDELYK
Mutagenized mRuby4$_{1\text{-}9}$	MVSKGEELIKENMRTKVVMEGSLNGHHFKCIGEGEGRPYEGVQTMRIKVI EGGPLPFAFDILATSFMYGSRTFIKYPADIPDFFKQSFPEGFTWERVTRYED GGVITVTQDTCLEDGELVYNVKVSGVNFPSNGPVMQKKTKGWEPNTEM MYPVDGGLRGYTDIALKVDGGGHLHCNFVTTYRSKKTV

Bolded text indicates **linker construct**. Yellow highlight indicates mutation.

4.8 METHODS

Molecular cloning

The amino acid sequences of the tripartite GFP components were obtained from a published report [7]. The bipartite split mRuby4 and full-length mRuby3 constructs were obtained from our group's previous report [9]. The split mRuby4 construct was split at the same sites as tripartite GFP. mIFP::CAAX was synthesized (Integrated DNA Technologies) and cloned into the mammalian expression vector pcDNA3.1 (Invitrogen) between KpnI and EcoRI (NEB) by using the In-Fusion HD cloning kit (Takara Bio). Each component, mRuby4$_{1\text{-}9}$, mRuby4$_{10–11}$, mRuby4$_{10}$, and mRuby4$_{11}$, was amplified from split mRuby4 construct [9] by PCR and subsequently inserted into the pcDNA3.1 vector containing the mIFP::CAAX sequence at the KpnI site (NEB) by using the In-Fusion HD cloning kit (Takara Bio).

For the nucleotide sequences of mRuby4$_{1\text{-}9}$, mRuby4$_{10–11}$, mRuby4$_{10}$, and mRuby4$_{11}$, see **Supplementary Table 4.1**. For amino acid sequences of mRuby4$_{10}$, and mRuby4$_{11}$, see **Supplementary Table 4.2**.

To validate a positive control and establish the parameters for the protein interaction assay, FKBP and FRB protein molecules were fused with the tripartite GFP tags first before fusing with our tripartite mRuby4 tags. To generate the plasmids of split tripartite FP-tag fusions, DNA fragments encoding FKBP fused to GFP$_{10}$, FKBP fused to mRuby4$_{10}$, FRB fused to GFP$_{11}$, and FRB fused to mRuby4$_{11}$ were amplified by inverse PCR with sets of primers (see also **Supplementary Table 4.3**) and assembled using the In-Fusion HD cloning kit (Takara Bio). For the PCR amplification, the following DNA templates were utilized: Lyn-FKBP-FKBP-CFP (LF2C) (Addgene #20149) and YFP-tagged FRB (YR) (Addgene #20148) [17].

Mutagenesis of tripartite mRuby4 simulation construct

For the first round of mutagenesis, we adopted a complementation assay previously described to optimize split mCherry2 in *E. coli* [11,20]. A 30 a.a. linker (GGGGSEGGGSGGPGSGGEGSAGGGSAGGGS) [9] was inserted between (1) either or (2) both: ninth and tenth β strands; and tenth and eleventh β strands of mRuby4. Through these insertions, $mRuby4_{1\text{-}10\text{-}longlinker\text{-}11}$, $mRuby4_{1\text{-}9\text{-}longlinker\text{-}10\text{-}11}$, and $mRuby4_{1\text{-}9\text{-}longlinker\text{-}10\text{-}longlinker\text{-}11}$ were generated. Each respective DNA sequence was synthesized and then cloned into the BamHI/XhoI sites of the *E. coli* expression vector pET28a (Novagen). For amino acid sequences of $mRuby4_{1\text{-}9\text{-}longlinker\text{-}10\text{-}11}$, $mRuby4_{1\text{-}9\text{-}longlinker\text{-}10\text{-}longlinker\text{-}11}$, and mutagenized $mRuby4_{1\text{-}9}$, see **Supplementary Table 4.4**. The amino acid sequence for $mRuby4_{1\text{-}10\text{-}longlinker\text{-}11}$ was adopted from our previous report [9].

To improve the complementation efficiency of the tripartite mRuby4 simulation construct, the $mRuby4_{1\text{-}9}$ component was mutagenized by using a GeneMorph II Random Mutagenesis Kit (Agilent), using a set of primers (see **Supplementary Table 4.3**). Amplicons of $mRuby4_{1\text{-}9}$ were cloned into the pET28a vector containing $mRuby4_{1\text{-}9\text{-}longlinker\text{-}10\text{-}longlinker\text{-}11}$ construct using the BamHI/EcoRI sites. Plasmid transformation into E. coli and mutagenesis screening was performed as per our previous study's protocol [9]. 900 colonies were screened after a single round of mutagenesis.

Fluorescence imaging

Confocal microscopy images of tripartite mRuby4 and tripartite GFP were captured on an inverted fluorescence microscope (Ti-E, Nikon) with a 100 × 1.45 NA oil immersion objective (Plan Apo, Nikon). The microscope was attached to the Dragonfly Spinning disk confocal unit (CR-DFLY-501, Andor). Two excitation lasers (40 mW 488 nm and 50 mW 561 nm lasers) were coupled to a multimode fiber passing through the Andor Borealis unit. A dichroic mirror (Dragonfly laser

dichroic for 405-488-561-640) and three bandpass filters (525/50 nm, 600/50 nm, and 725/40 nm bandpass emission wheel filters) were placed in the imaging path. The images were recorded with an EM-CCD camera (iXon, Andor). Average intensity z projections were shown in z projections, unless otherwise noted in the figure legends. Analyses of the confocal images were performed on Fiji software (NIH).

Cell culture, transfection, and rapamycin treatment

Cell culture was maintained as per our previous study's protocol. Plasmids were transfected at 600–900 ng DNA per well with Lipofectamine 2000 (3 μL, Invitrogen) or polyethylenimine (3 μL of 1 mg/mL PEI, Polysciences, Inc.) into Nunc Lab-Tek II Chambered Cover Glass (size: 8 wells, Nalge Nunc International) or Corning Costar Cell Culture Plates (size: 12 or 24 wells, Corning). In experiments where three separate constructs are expressed, the plasmids of each FP-tag and their detector fragment were transfected at 300 ng each. Cells were fixed with buffered 4% paraformaldehyde (Electron Microscope Sciences), mounted with PBS, and imaged by confocal microscopy. For drug-induced interactions, rapamycin (LC laboratories) was diluted in PBS, added to the FRB/FKBP protein assay for the final concentration of 200nM rapamycin, and imaged after 1-hour incubation. Time-lapse images of tripartite GFP reconstitution fluorescence in the FRB/FKBP protein assay were imaged using confocal microscopy at 10-minute intervals, for 2 hours.

Statistics and reproducibility

All experiments for the quantification of fluorescent levels in 293T cells were replicated at least 3 times independently. Statistical analyses were performed using JMP Pro 16. Error bars in all figures refer to the standard deviation of the mean.

4.9 ACKNOWLEDGEMENTS

We thank R. Tamura for split mRuby4 construct and M. Fitch for technical support. We acknowledge the assistance of the Biomedical Microscopy Core and the CTEGD Cytometry Shared Resource Laboratory. This work was supported by an NIH R01 NS107558 (to D.K.).

4.10 AUTHOR CONTRIBUTIONS

D.K. and K.C.B. designed the project and edited the manuscript. K.C.B. produced reagents, performed experiments, analyzed the data, and wrote the manuscript.

4.11 COMPETING FINANCIAL INTERESTS

The authors declare no competing financial interests.

4.11 REFERENCES

[1] F.G. Prendergast, K.G. Mann, Chemical and Physical Properties of Aequorin and the Green Fluorescent Protein Isolated from Aequorea forskålea†, Biochemistry. 17 (1978). https://doi.org/10.1021/bi00610a004.

[2] M. Zimmer, GFP: From jellyfish to the Nobel prize and beyond, Chem. Soc. Rev. 38 (2009). https://doi.org/10.1039/b904023d.

[3] R.Y. Tsien, THE GREEN FLUORESCENT PROTEIN, Annu. Rev. Biochem. 67 (1998) 509–544. https://doi.org/https://doi.org/10.1146/annurev.biochem.67.1.509.

[4] T.K. Kerppola, Bimolecular Fluorescence Complementation (BiFC) Analysis as a Probe of Protein Interactions in Living Cells, Annu. Rev. Biophys. (2008). https://doi.org/10.1146/annurev.biophys.37.032807.125842.

[5] T.K. Kerppola, Visualization of molecular interactions by fluorescence complementation, Nat. Rev. Mol. Cell Biol. 7 (2006). https://doi.org/10.1038/nrm1929.

[6] J.D. Pedelacq, S. Cabantous, Development and applications of superfolder and split fluorescent protein detection systems in biology, Int. J. Mol. Sci. 20 (2019). https://doi.org/10.3390/ijms20143479.

[7] S. Cabantous, H.B. Nguyen, J.-D. Pedelacq, F. Koraïchi, A. Chaudhary, K. Ganguly, M.A. Lockard, G. Favre, T.C. Terwilliger, G.S. Waldo, A New Protein-Protein Interaction Sensor Based on Tripartite Split-GFP Association, Sci. Rep. 3 (2013) 2854. https://doi.org/10.1038/srep02854.

[8] D. Kamiyama, S. Sekine, B. Barsi-rhyne, J. Hu, B. Chen, L.A. Gilbert, H. Ishikawa, M.D. Leonetti, W.F. Marshall, J.S. Weissman, B. Huang, Versatile protein tagging in cells with split fluorescent protein, Nat. Commun. 7 (2016) 1–9. https://doi.org/10.1038/ncomms11046.

[9] R. Tamura, F. Jiang, J. Xie, D. Kamiyama, Multiplexed labeling of cellular proteins with split fluorescent protein tags, Commun. Biol. 4 (2021). https://doi.org/10.1038/s42003-021-01780-4.

[10] S. Kredel, F. Oswald, K. Nienhaus, K. Deuschle, C. Röcker, M. Wolff, R. Heilker, G.U. Nienhaus, J. Wiedenmann, mRuby, a bright monomeric red fluorescent protein for labeling of subcellular structures, PLoS One. 4 (2009). https://doi.org/10.1371/journal.pone.0004391.

[11] S. Feng, A. Varshney, D.C. Villa, C. Modavi, J. Kohler, F. Farah, Bright split red fluorescent proteins with enhanced complementation efficiency for the tagging of endogenous proteins and visualization of synapses, Nat. Commun. 8 (2018).

[12] J. Akerboom, N.C. Calderón, L. Tian, S. Wabnig, M. Prigge, J. Tolö, A. Gordus, M.B. Orger, K.E. Severi, J.J. Macklin, R. Patel, S.R. Pulver, T.J. Wardill, E. Fischer, C. Schüler, T.W. Chen, K.S. Sarkisyan, J.S. Marvin, C.I. Bargmann, D.S. Kim, S. Kügler, L. Lagnado, P. Hegemann, A. Gottschalk, E.R. Schreiter, L.L. Looger, Genetically encoded calcium indicators for multi-color neural activity imaging and combination with optogenetics, Front. Mol. Neurosci. (2013). https://doi.org/10.3389/fnmol.2013.00002.

[13] T. Förster, Zwischenmolekulare Energiewanderung und Fluoreszenz, Ann. Phys. 437 (1948). https://doi.org/10.1002/andp.19484370105.

[14] T. Főrster, Delocalized excitation and excitation transfer, U.S. At. Energy Comm. F. Full J. Title. (1965). https://doi.org/10.2172/4626886.

[15] A. Margineanu, J.J. Chan, D.J. Kelly, S.C. Warren, D. Flatters, S. Kumar, M. Katan, C.W. Dunsby, P.M.W. French, Screening for protein-protein interactions using Förster resonance energy transfer (FRET) and fluorescence lifetime imaging microscopy (FLIM), Sci. Rep. 6 (2016). https://doi.org/10.1038/srep28186.

[16] S.R.K. Ainavarapu, J. Brujić, H.H. Huang, A.P. Wiita, H. Lu, L. Li, K.A. Walther, M. Carrion-Vazquez, H. Li, J.M. Fernandez, Contour length and refolding rate of a small protein controlled by engineered disulfide bonds, Biophys. J. 92 (2007). https://doi.org/10.1529/biophysj.106.091561.

[17] T. Inoue, W. Do Heo, J.S. Grimley, T.J. Wandless, T. Meyer, An inducible translocation strategy to rapidly activate and inhibit small GTPase signaling pathways, Nat. Methods. (2005). https://doi.org/10.1038/nmeth763.

[18] S. Cabantous, T.C. Terwilliger, G.S. Waldo, Protein tagging and detection with engineered self-assembling fragments of green fluorescent protein, Nat. Biotechnol. 23

(2005). https://doi.org/10.1038/nbt1044.

[19] S. Cabantous, G.S. Waldo, In vivo and in vitro protein solubility assays using split GFP, Nat. Methods. 3 (2006). https://doi.org/10.1038/nmeth932.

[20] S. Feng, S. Sekine, V. Pessino, H. Li, M.D. Leonetti, B. Huang, Improved split fluorescent proteins for endogenous protein labeling, Nat. Commun. 8 (2017) 370. https://doi.org/10.1038/s41467-017-00494-8.

CHAPTER 5

CONCLUSIONS AND FUTURE DIRECTIONS

5.1 SUMMARY OF DISSERTATION

Neuronal fascicle instructs MN24 axon and dendrite patterning

In Chapter 2, we revealed that the longitudinal neuronal fascicle within the nerve cord can guide motoneuron axon and dendrite patterning via Dscam1 signaling. For many decades, previous works explored midline diffusible cues as the central reference cues for axon and dendrite patterning [1–10]. Given that *Drosophila* motoneuron pattern their axon and dendrites in a precise, spatial manner, it is likely that juxtracrine signaling may play a role in the invariant patterning of these subcellular structures. Our group's study previously identified Dscam1-mediated neuronal interaction between aCC and MP1 neuron underlies aCC dendritogenesis [11]. Interestingly, Dscam1's function is not exclusive to just dendritogenesis but extends to functions such as axon guidance, cell migration, and self-avoidance [12–19]. One prevailing question to answer was whether juxtracrine signaling plays a role in other motoneuron morphologies, and if so, what are the molecular cues? There exists motoneurons types that have distinct morphological features compared to the textbook-example aCC motoneuron. While the axon of aCC projects directly from the soma to innervate muscle 1 in the peripheral field, there are many motoneurons that do not have this direct peripheral projection. Rather, this category of motoneurons project their axons towards the midline, rotate to project along the anterior-posterior axis, and finally rotate to project away from the midline and towards their respective muscle targets, like MN24. We refer to the

detour of the axon before its muscle innervation as 'axon routing'. Based off the motoneuron compilation from Landgraf et al., we estimate that half of the known motoneuron types have an axon routing feature. To answer our question whether juxtracrine signaling plays a role in other motoneuron morphologies, we used MN24 due to its axon routing feature and distinct location of MN24 dendrites from the aCC-MP1 interaction site. First, we characterized the mediolateral positions of MN24 and lateral fascicle labeled by the *scp2*-GAL4 driver. We found that the positions of MN24 dendrites overlap with the position of the lateral fascicle, raising the likelihood of neuronal contact due to this proximity. Second, upon knocking down *dscam1* in either MN24 or *Scp2*-positive fascicle, we observed (1) a reduction in the number of primary dendritic branches and (2) an unexpected axon routing defect, mirroring the phenotype seen in *dscam1*$^{-/-}$ mutants. The observation that MN24 axons still contact the *Scp2*-positive fascicle in *dscam1*$^{-/-}$ mutants rules out the possibility that the mutant phenotype is due to a mislocalization of these neural processes. This suggests that *dscam1* in both MN24 and *Scp2*-positive fascicle is necessary for MN24 dendrite formation and axon routing. Third, our rescue experiments in *dscam1*$^{-/-}$ mutants, involving the reintroduction of *dscam1* into either MN24 or *Scp2*-positive fascicle, were unsuccessful in rescuing either defects in dendritic count or axon routing. This indicates that *dscam1* function in either neuron type alone is insufficient. However, when *dscam1* was reintroduced into both MN24 and *Scp2*-positive fascicle in *dscam1*$^{-/-}$ mutants, we could fully rescue the dendritic and axonal phenotype. Overall, our findings indicate that the lateral fascicle structure serves as a novel reference structure for motoneuron neurite patterning. Moreover, Dscam1 serves as a positional cue, mediating MN24 morphology in relation to the lateral fascicle. From these results, we propose a model, in which Dscam1 (1) mediates the interaction between MN24 and the lateral fascicle and (2) plays differential roles within an individual motoneuron.

Alternative CRISPR/Cas9 knock-in approach using PCR-amplicon-donor in *Drosophila*

In Chapter 3, we demonstrate an alternative knock-in approach using the PCR-amplicon as a donor format in *Drosophila*. First, we show that Cas9-expressing embryos injected with the PCR product donor template and plasmid expressing the *ebony*-gRNA had a knock-in event in the *ebony* gene. We confirm the knock-in event by PCR screening with a primer set recognizing the knock-in site within the *ebony* gene. Second, to demonstrate that the genomic integration of the PCR product could be transmitted in the *Drosophila* germline and subsequent progeny, we use a two-step screening approach to generate a knock-in fly line using the PCR product donor. We use a genetic complementation assay and screen for dark-body-colored progeny that may contain the germline-transmitted knock-in. Then, we use the aforementioned PCR screening to detect the knock-in event in the *ebony* gene of single fly progeny, also later confirmed by Sanger sequencing. Altogether, we report a cloning-free, alternative approach for knock-in using the PCR product. In theory, this approach can be used in a scalable fashion to rapidly generate multiple mutant fly lines in accordance with the *Drosophila* Gene Disruption Project.

Generation of red-colored tripartite mRuby4 system

In Chapter 4, we demonstrate the fluorescent reconstitution of the red-colored tripartite mRuby4 system under multiple cellular contexts. First, we show that reconstitution occurs when both tripartite mRuby4 tags ($mRuby4_{10}$ and $mRuby4_{11}$) are localized within proximity of each other in the presence of the detector fragment ($mRuby4_{1\text{-}9}$). Secondly, we show that fluorescent reconstitution does not occur when (1) tripartite mRuby4 tags ($mRuby4_{10}$ and $mRuby4_{11}$) are fused to FKBP and FRB and (2) the FKBP-FRB interaction is induced. Because we do not see any fluorescence result despite the tripartite mRuby4 tags are fused to their respective interacting proteins, we outline a mutagenesis-based approach to improve the complementation efficiency of

the tripartite mRuby4 fragments. Altogether, the tripartite mRuby4 system is a promising interaction sensor as a red-colored alternative to the existing tripartite GFP system.

5.2 FUTURE DIRECTIONS

Dscam1 signaling for motoneuron axon and dendrite patterning

In this dissertation, we proposed a general role of Dscam1 as a positional cue for motoneuron dendrite and axon patterning in the *Drosophila* nerve cord. This finding suggests that Dscam1 must be supplied non-cell-autonomously by another neuron to precisely pattern motoneuron neurites. Our previous study identified MP1 neuron as the Dscam1 supplier neuron for aCC dendritogenesis. A cluster of questions that arises from this: Is a single cell or a group of cells supplying Dscam1 for MN24 dendrite formation? What distinguishes this neuron as a Dscam1-supplier neuron compared to another neuron with Dscam1 expression? What other neuron pairs have this Dscam1-mediated motoneuron dendrite and axon patterning? One possible explanation is that early-born neurons that can project their processes first may later supply Dscam1 to establish motoneuron neurite patterning. Coined as “pioneer neurons”, these neurons project their axons out to the target first, later trailed by growth cones of other neurons [20]. MP1 neuron has been uniquely known to be one of the first neurons to project its axon along in the medial section of the longitudinal commissure. Thus, the unidentified neuron that first establishes its axon along the lateral part of the longitudinal commissure may be responsible for MN24 axon and dendrite patterning. Advancements in single-cell sequencing technologies may provide more insight into the neuron identity, at least at the level of gene expression. Analyzing the transcriptomic data will permit identifying and distinguishing different types of neurons that may play a role of juxtracrine patterning of neurites. Linking this information with functional assays such as electrophysiology

and microscopy, we can begin to probe these guiding partner neurons and gain insight into the CNS organization pattern underlying flies and potentially vertebrates.

Scalable generation of specific mutant fly lines

While our demonstration of CRISPR/Cas9-mediated knock-in strategy using the PCR product donor in Chapter 3 was restricted to the *ebony* gene, this strategy could be readily adapted to other genes. Currently, there are roughly 3,000 genes in the fly genome that do not have an associated mutant fly line available at the Blooming Drosophila Stock Center. This alternative approach bypasses molecular cloning of the donor, which can be time-consuming and labor-intensive. With commercially available oligonucleotides, this strategy allows for scalable, cloning-free knock-in using the CRISPR/Cas9 system.

With the advent of multiplexed CRISPR/Cas technologies, researchers can theoretically generate combinatorial genetic knockouts using this strategy [21]. The success of concurrent multiple knock-ins depends on factors such as the editing efficiency of the Cas endonuclease or the number and specificity of the gRNAs. Intentional design by the user bypasses some of these limitations – one such solution to ensure efficient editing by multiple gRNAs is to use predictive algorithms or computational tools such as web-based FlyCRISPR's Target Finder tool (https://flycrispr.org/target-finder/) to avoid off-targeting effects [22]. With this approach and technological advances, future work will give rise to more available mutant fly lines and allow researchers to probe corresponding gene functions and interactions.

Utilizing the triparite mRuby4 system as an interaction sensor

So far, we characterized the generation of tripartite mRuby4 system in Chapter 4. As mentioned previously, the tripartite mRuby4 could still be further improved as an interaction sensor for live cell imaging. Upon improvement through a mutagenesis-based approach, the tripartite mRuby4

system can be a powerful, red-colored detector for protein-protein interaction. One benefit of using the tripartite FP system is the short tags that can be fused to the proteins of interest.

Since our study in Chapter 3 focuses on introducing a short disruptive cassette, this approach could be utilized for the knock-in of a short tag of comparable size (such as mRuby4$_{10 \text{ or } 11}$), thereby endogenously tagging proteins. Using our approach, the mRuby4$_{10 \text{ or } 11}$ fragments (which is approximately ~50 bp) could be readily synthesized and used as a knock-in donor. Thus, this approach could be scalable to generate a library of proteins endogenously tagged with knock-in mRuby4$_{10 \text{ or } 11}$, upon further characterization of this donor format.

5.3 REFERENCES

[1] Brankatschk M, Dickson BJ. Netrins guide Drosophila commissural axons at short range. Nat Neurosci 2006;9. https://doi.org/10.1038/nn1625.

[2] Ito K, Urban J, Technau GM. Distribution, classification, and development of Drosophila glial cells in the late embryonic and early larval ventral nerve cord. Roux's Arch Dev Biol 1995;204. https://doi.org/10.1007/BF02179499.

[3] Mitchell KJ, Doyle L. JL, Serafini T, Kennedy TE, Tessier-Lavigne M, Goodman CS, et al. Genetic analysis of Netrin genes in Drosophila: Netrins guide CNS commissural axons and peripheral motor axons. Neuron 1996;17. https://doi.org/10.1016/S0896-6273(00)80153-1.

[4] Zlatic M, Landgraf M, Bate M. Genetic specification of axonal arbors: atonal regulates robo3 to position terminal branches in the Drosophila nervous system. Neuron 2003;37. https://doi.org/10.1016/S0896-6273(02)01131-5.

[5] Kidd T, Brose K, Mitchell KJ, Fetter RD, Tessier-Lavigne M, Goodman CS, et al.

Roundabout controls axon crossing of the CNS midline and defines a novel subfamily of evolutionarily conserved guidance receptors. Cell 1998;92. https://doi.org/10.1016/S0092-8674(00)80915-0.

[6] Kidd T, Bland KS, Goodman CS. Slit is the midline repellent for the Robo receptor in Drosophila. Cell 1999;96. https://doi.org/10.1016/S0092-8674(00)80589-9.

[7] Long H, Sabatier C, Ma L, Plump A, Yuan W, Ornitz DM, et al. Conserved roles for Slit and Robo proteins in midline commissural axon guidance. Neuron 2004;42. https://doi.org/10.1016/S0896-6273(04)00179-5.

[8] Simpson JH, Kidd T, Bland KS, Goodman CS. Short-range and long-range guidance by Slit and its robo receptors: Robo and Robo2 play distinct roles in midline guidance. Neuron 2000;28. https://doi.org/10.1016/S0896-6273(00)00151-3.

[9] Furrer MP, Kim S, Wolf B, Chiba A. Robo and Frazzled/DCC mediate dendritic guidance at the CNS midline. Nat Neurosci 2003;6. https://doi.org/10.1038/nn1017.

[10] Evans TA, Bashaw GJ. Axon guidance at the midline: of mice and flies. Curr Opin Neurobiol 2010;20. https://doi.org/10.1016/j.conb.2009.12.006.

[11] Kamiyama D, McGorty R, Kamiyama R, Kim MD, Chiba A, Huang B. Specification of Dendritogenesis Site in Drosophila aCC Motoneuron by Membrane Enrichment of Pak1 through Dscam1. Dev Cell 2015;35. https://doi.org/10.1016/j.devcel.2015.09.007.

[12] Schmucker D, Clemens JC, Shu H, Worby CA, Xiao J, Muda M, et al. Drosophila Dscam is an axon guidance receptor exhibiting extraordinary molecular diversity. Cell 2000;101. https://doi.org/10.1016/S0092-8674(00)80878-8.

[13] Dong H, Guo P, Zhang J, Wu L, Fu Y, Li L, et al. Self-avoidance alone does not explain the function of Dscam1 in mushroom body axonal wiring. Curr Biol 2022;32.

https://doi.org/10.1016/j.cub.2022.05.030.

[14] Zhu H, Hummel T, Clemens JC, Berdnik D, Zipursky SL, Luo L. Dendritic patterning by Dscam and synaptic partner matching in the Drosophila antennal lobe. Nat Neurosci 2006;9. https://doi.org/10.1038/nn1652.

[15] Wojtowicz WM, Flanagan JJ, Millard SS, Zipursky SL, Clemens JC. Alternative splicing of Drosophila Dscam generates axon guidance receptors that exhibit isoform-specific homophilic binding. Cell 2004;118. https://doi.org/10.1016/j.cell.2004.08.021.

[16] Zhan XL, Clemens JC, Neves G, Hattori D, Flanagan JJ, Hummel T, et al. Analysis of Dscam diversity in regulating axon guidance in Drosophila mushroom bodies. Neuron 2004;43. https://doi.org/10.1016/j.neuron.2004.07.020.

[17] Goyal G, Zierau A, Lattemann M, Bergkirchner B, Javorski D, Kaur R, et al. Inter-axonal recognition organizes Drosophila olfactory map formation. Sci Rep 2019;9. https://doi.org/10.1038/s41598-019-47924-9.

[18] Liu C, Trush O, Han X, Wang M, Takayama R, Yasugi T, et al. Dscam1 establishes the columnar units through lineage-dependent repulsion between sister neurons in the fly brain. Nat Commun 2020;11. https://doi.org/10.1038/s41467-020-17931-w.

[19] Wilhelm N, Kumari S, Krick N, Rickert C, Duch C. Dscam1 Has Diverse Neuron Type-Specific Functions in the Developing Drosophila CNS. ENeuro 2022;9. https://doi.org/10.1523/ENEURO.0255-22.2022.

[20] Bate CM. Pioneer neurones in an insect embryo. Nature 1976;260. https://doi.org/10.1038/260054a0.

[21] McCarty NS, Graham AE, Studená L, Ledesma-Amaro R. Multiplexed CRISPR technologies for gene editing and transcriptional regulation. Nat Commun 2020;11.

https://doi.org/10.1038/s41467-020-15053-x.

[22] Gratz SJ, Ukken FP, Rubinstein CD, Thiede G, Donohue LK, Cummings AM, et al. Highly specific and efficient CRISPR/Cas9-catalyzed homology-directed repair in Drosophila. Genetics 2014. https://doi.org/10.1534/genetics.113.160713.